The Application of Synchrotron Radiation and in Particular X-ray Absorption Spectroscopy to Matrix Isolated Species

Nigel A. Young

Department of Chemistry

The University of Hull

Kingston upon Hull

HU6 7RX

Abstract

This review provides comprehensive coverage of the application of X-ray absorption spectroscopy (XAS, XAFS, EXAFS, XANES) to matrix isolated species. As X-ray absorption spectroscopy provides structural data without the need for long range order it has been applied to a large number of systems to yield unique structural data about both the matrix isolated species, and their interactions with the matrix host. To put the work into perspective there is a tutorial introduction to the theoretical background of X-ray absorption spectroscopy, data content, processing and analysis. In addition there is brief coverage of the use of other synchrotron radiation techniques for the study of matrix isolated species, and a consideration of future perspectives.

Keywords

Matrix isolation; X-ray absorption spectroscopy; EXAFS; XANES; Synchrotron Radiation

1. Introduction

This review covers the application of synchrotron radiation (SR) to the characterisation of matrix isolated species up to early 2014. Although the characterisation of matrix isolated species has used SR over its entire range, this review will concentrate on the application of X-ray absorption spectroscopy to matrix isolated species, with a brief coverage of the other spectral regions. In addition, there is a short section on possible future experiments.

2. Synchrotron Radiation

Synchrotron radiation (SR) is emitted by charged particles (usually electrons or positrons) travelling at relativistic speeds when accelerated by magnetic fields. The initial experiments utilising SR were carried out parasitically at particle physics accelerator facilities. This was followed by purpose built facilities known as second generation sources, dedicated to SR users from chemistry, physics, materials science, biology etc. Originally the storage rings used conventional bending electromagnets to generate the SR, but the more recent developments use a variety of "insertion" devices such as undulator and wiggler magnets in the intervening straight sections to produce the SR. At these third generation sources, undulator magnets are used to produce highly focussed high intensity radiation, whereas Wiggler or wavelength shift magnets are primarily used to produce shorter wavelength output. In essence the early SR machines were a set of bends linked by empty straight sections, whereas now they are best thought of as a series of straight sections connected by bending magnets, although the bending magnet radiation is still used.

The advantages of SR are that it provides a very intense and tuneable source of continuum radiation from the far-IR through to the hard X-ray. The radiation is inherently linearly polarised and circularly polarised light is relatively easy to obtain. The major disadvantage is the limited access to the national and international facilities.

3. Matrix isolation

Matrix isolation is an experimental method for stabilising otherwise intractable, unstable and highly reactive species long enough for them to be spectroscopically characterised. The use of solid noble gases was originally pioneered by George Pimentel in the 1950s [1] and has now developed into a mature technique that has been used to study a wide selection of species [2-17]. In essence, it is similar to preparing a KBr disc for IR spectroscopy, except

that the KBr is replaced by a cryogenic matrix such as solid neon, argon or nitrogen, and true atomic or molecular dilution is achieved. The most common approach is to use solid argon as the matrix host at *ca*. 10 K with the species of interest diluted in it at ratios of the order of 1:100 to 1:1000, but more concentrated and dilute mixtures are also used. The more dilute the mixture, the higher the quality of the spectra in terms of bandwidth, but this has downsides in terms of detection. With the improvement in cryostat technology, neon and hydrogen (including *p*-H_2) matrices are now also routinely used. The use of helium nanodroplets to provide helium matrices is becoming more widespread [18-22].

The details of the experimental set-up required for matrix isolation have been well described by Dunkin [16] and the requirements are similar for most spectroscopic techniques. In essence, a cryostat with a spectroscopically suitable substrate is held at a low enough temperature to condense the matrix gas, which is usually less than half the melting point of the matrix solid [12-14]. The most popular cryostats are He closed cycle systems, rather than He flow cryostats, and with these it is now possible to reach *ca*. 4 K. It should be noted that the early pioneers employed liquid hydrogen cryostats. The cryostat is mounted in a vacuum chamber with a number of ports to allow for spectroscopy, sample inlet *via* either heating or cooling to obtain sufficient vapour pressure, as well as photolysis etc. The quality of the matrix deposit is very dependent on the deposition conditions used, and each laboratory has its own preferred method, but in general the matrix gas is bled/leaked into the vacuum chamber at a few mmol hr^{-1} until the spectra are of sufficient intensity and quality. Pulsed deposition has been found to improve spectral quality by some workers. In addition to using inert matrix gases, the experiments can also use inert gases doped with reactive species such as CO, NO, alkenes, etc or neat reactive matrices such as CO, N_2, Cl_2, F_2 etc., and the reactions monitored on deposition, or after subsequent photolysis or annealing.

The most common spectroscopic technique used is infrared as this gives excellent speciation and product identification. The sharp bands (fwhm ~1 cm^{-1} or better) that result from trapping in a non-interacting medium allow for the use of both natural and induced isotopes that are crucial to determining the number of atoms involved, as well as the bond angles and mode of bonding. Although it is attractive to obtain Raman data from matrices, this has always been much more of a struggle due to sensitivity and radiation damage, in addition to the more usual fluorescence problems. Electronic absorption (UV-vis) spectroscopy is useful for studying atomic species, but because of the broad bands in molecular species it is usually

not sufficient without other supporting data. In some cases vibrational progressions can be observed [23]. EPR is very powerful for open shell systems such as organic and main group radicals and transition metal compounds with unpaired electrons. Niche techniques such as Mössbauer spectroscopy have found also some use.

Whilst these spectroscopic techniques provide excellent speciation as well as insight into bonding, the ability to obtain direct structural information is limited to bond angles from IR spectra using either isotopic shifts or relative intensities. The ability to determine bond lengths and other inter- and intra-atomic distances directly is very limited to a couple of techniques such as NMR and X-ray absorption spectroscopy.

NMR spectroscopy of matrix isolated species was first reported in 1978 [24, 25], including the determination of a spectrum consistent for $(HCl)_2$ in solid ^{40}Ar with a linear hydrogen bond and a Cl ...Cl separation of 3.7 Å, with the second unit 122° to the first HCl molecule [25]. Subsequent developments include the study of *o*-H_2 in solid Ne, Ar, Kr and *p*-H_2 [26], ^{13}C CPMAS studies of photochemically generated molecules in frozen organic glasses [27, 28], the design and application of an NMR spectrometer capable of working at 26 K [29] and the study of N_2/Ar mixtures [30-33]. Although it is possible to use ^{13}C cross-polarisation spectra from species containing a pair of adjacent ^{13}C nuclei to reflect the ^{13}C-^{13}C dipolar coupling of matrix isolated organic species to obtain interatomic distances, this has not found widespread use. For example, a value of 1.53 Å for the carbon-carbon distance in matrix isolated cyclopropane was in reasonable agreement with the X-ray value of 1.510 Å [34]. Other examples of NMR derived interatomic distances include CH_3F (1.40_5 $\pm 0.02_0$ Å), C_2H_2 (1.21_5 $\pm 0.01_5$ Å) C_2H_4 (1.34 $\pm 0.01_5$ Å), CH_3CHO (1.54_0 ± 0.01_5 Å) [35]; *o*-benzyne (1.24 ±0.02 Å) [36]

Whilst X-ray and neutron diffraction techniques are the method of choice for obtaining high quality structural data in the solid state, they are of more limited use for the study of matrix isolated species, but have been extensively used to study the structures of the pure hosts [37-40] including at high pressure [41]. Of more relevance to matrix isolation are those experiments involving rapidly vapour deposited matrix gases with and without dopants [42-52] and monitoring the growth of argon on graphite [53].

Neutron diffraction scattering can provide both diffraction and spectroscopic (INS) data from the same sample [44], and inelastic neutron scattering was reviewed in 1992 [54]. In addition the sampling depth for neutron diffraction can be much greater than for X-rays. For solid rapid vapour deposited Kr annealing at 100 K was required to observe sharp Bragg reflections from the fcc/ccp phase, and the neutron diffraction pattern was significantly modified by the addition of small amounts of water [45]. Diffraction (X-ray and neutron) patterns for pure argon and krypton were interpreted in terms of a three phase model: a basic fcc/ccp core structure (*Fm*3*m*), with dislocations give rise to stacking faults, which results in a related hcp phase ($P6_3/mmc$), as well as a region giving rise to a broad diffuse intensity [44, 45, 47, 49]. More recent work has indicated that CH_4 and SF_6 suspended in solid Ar or Kr do not significantly increase the width of the Bragg reflections immediately after deposition, as the line widths are dominated by the crystallite size (400 – 500 Å for Ar) [52]. For these systems, no narrowing of the X-ray Bragg reflections were observed on annealing. Pure argon and krypton were shown to adopt a regular fcc structure when obtained by preparing the samples either from the liquid or condensing onto sample support at 40 K [47]. Pure solid nitrogen below 37 K also had an fcc equilibrium structure with *Pa*3 symmetry.

These rapid vapour deposition experiments [42-45, 47-52] have shown that cryogenic matrices originating from gas phase deposition are generally microcrystalline porous solids, which may also contain amorphous or nearly amorphous domains [49]. Vapour deposition introduces structural disorder into solids and two effects were identified: (i) the low temperature suppresses diffusion and relaxation of the solid during deposition, and thus even in pure matrices defects like stacking faults arise at a high concentration. Mixtures are frozen which are not stable under equilibrium conditions; (ii) The undercooling leads to a high rate of nucleation and thus to very small grains. At low temperatures these grains are metastable, in spite of their high surface energy [47].

Electron diffraction has also been used to study small argon clusters (20-50 atoms) [55] as well as larger ones up to 750 atoms [56]. Whilst X-ray and neutron diffraction gives important structural information about the host and the effect that its rapid deposition and the presence of dopants may have upon it, it is not widely practised as the majority of the matrix isolation community is much more interested in the structures and properties of the trapped guest species.

4. X-ray absorption spectroscopy

4.1. Introduction

As X-ray absorption spectroscopy is element specific, and can be carried out in any phase it is ideally suited to obtaining structural data from both the matrix and the matrix isolated species. The reason why it is not more widely used is that it requires an intense source of X-rays that is only feasible at synchrotron radiation sources. In order to appreciate the information (and its limitations) that is obtainable using X-ray absorption spectroscopy of matrix isolated species it is necessary to briefly consider its theoretical basis as well as aspects of data collection, manipulation and analysis.

4.2. Interactions of X-rays with matter

There are four principal ways that X-rays interact with matter and appear to be absorbed. However, three of these are scattering events, and only the fourth is true absorption.

4.2.1. X-ray scattering processes

Rayleigh scattering occurs when the incident and scattered radiation have the same energy and phase relationship. This gives rise to the coherent or elastic scattering found in conventional diffraction experiments. Compton scattering occurs when the incident radiation interacts with the outer electrons of the absorbing atom and loses some energy. This is no longer an elastic process as the scattered and incident radiation no longer have the same energy or phase relationship. It increases with photon energy, and is in part responsible for the diffuse scatter seen in diffraction experiments. X-ray Raman scattering is similar to the more common Raman techniques and just as visible laser scattering is subject to weak Raman scattering when transitions between vibrational energy levels are detectable, so with X-ray scattering weak Raman scatter peaks at well defined energies can also be observed.

4.2.2. "True" X-ray absorption

In contrast to the scattering processes, "true" absorption occurs at discrete energies when electrons are excited from core levels such as the 1s, to either vacant valence orbitals, virtual/Rydberg states or into the continuum when photoionisation takes place. If the excitation process involves a 1s electron, it is a K-edge or K shell process. At the L-edge (n = 2) there is the possibility of excitation from the 2s or 2p orbitals. A process involving the 2s electron gives rise to a L_1 or L_I-edge, whereas due to spin-orbit coupling of the core-hole there are two edges from 2p orbitals known as $L_{2,3}$ or $L_{II,III}$-edges, with the L_3 being the $2p_{3/2}$ and the L_2 the $2p_{1/2}$ process. From similar considerations there are 5 M edges arising from the

3s, 3p and 3d orbitals. A schematic diagram of the relative energies of the absorption edges is shown in Fig. 1. As the energy for every edge is element dependent, this gives the technique one of its major advantages: i.e. it is ***element specific***. This means that it is possible to obtain structural information from a minor component (guest) in the presence of a major component (matrix host).

4.2.3. **X-ray absorption and relaxation processes**

Although excitations from many core shells are possible, the majority of experiments use the K- or L-edges. The formation of a core hole leaves the atom in a highly excited state, and it seeks to fill this core-hole *via* a variety of relaxation mechanisms. How this subsequent core hole is filled gives rise to two different forms of emission. One is radiative and results in the emission of "characteristic" X-rays when an electron moves from a higher orbital to the core hole. These X-rays are the same as those produced when high energy electrons bombard the metal target in a conventional X-ray tube. The second, non-radiative process, also involves an electron moving from a higher orbital to the core-hole, but this time with the simultaneous emission of an Auger electron, again with characteristic energy. Fig. 2 demonstrates the relaxation processes from the L shell to a K shell core-hole. Electrons from the L_2 or L_3 levels are much more likely as 2p-1s transitions are orbitally allowed, whereas the at L_1 level the 2s-1s transitions are orbitally forbidden. Clearly there are then subsequent processes resulting in further emission of X-rays and electrons. In particular, secondary electron emission results in emission of electrons with a wide variety of energies. Auger emission is favoured for lighter elements, whereas for heavier elements, X-ray emission dominates. Whilst the direct absorption of X-rays can be used to obtain spectra, for dilute systems such as matrix isolated species, X-ray fluorescence and electron emission are more common.

4.3. **X-ray absorption spectra**

There are a number of phrases and abbreviations in common use to describe the various parts of the X-ray absorption spectrum. X-ray absorption spectroscopy (XAS) and X-ray absorption fine structure spectroscopy (XAFS) are used to describe the whole spectrum. In contrast, X-ray absorption near edge structure (XANES) or near edge X-ray absorption fine structure (NEXAFS) are used to describe the features in close proximity to the absorption edge. Extended X-ray absorption fine structure (EXAFS) is used to describe the oscillations in the absorption cross section beyond the edge. The Cr K-edge spectrum of CrO_2Cl_2 at 10 K (Fig. 3) shows how the X-ray absorption spectrum is conveniently divided into the XANES

and EXAFS regions. For lower energy edges (< 2 keV), the XANES or NEXAFS features dominate the spectra, whilst at intermediate energies (2 – 14 keV) both XANES and EXAFS regions are very useful, at higher energies the XANES features become broad and less diagnostic due to core-hole lifetime effects.

4.3.1. **X-ray absorption near edge structure (XANES)**

The XANES part of the spectrum comprises the features just prior to the edge as well as the edge itself and is the result of transitions from the core level (1s for K-edges) to valence orbitals (e.g. 3d, 4p) as well as virtual or Rydberg states (e.g. 5p etc.) and these are shown schematically in Fig. 4. The position of both the distinctive features and the edge itself are often used to identify oxidation states as they move to higher energy with an increase in oxidation state.

The transitions are governed by the normal electronic absorption spectroscopy selection rules (dipole ($\Delta l = \pm 1$); spin ($\Delta S = 0$); Laporte (if *i* then must be change in parity)). Therefore, 1s – 3d transitions at the K-edges are dipole forbidden, but because there is extensive p-d mixing in tetrahedral molecules such as CrO_2Cl_2, they can become quite intense, especially if the d-manifold is empty. Whilst there is some quadrupole contribution to the 1s-3d transitions, these are also inherently weak.

Whilst schematic diagrams (e.g. Fig. 4) have been widely used, with recent developments in time-dependent DFT calculations by Neese *et al*. it is now possible to carry out accurate XANES calculations on the core level transitions, which also allow for visualisation of the orbitals involved [57-63]. The calculated TD-DFT XANES spectrum for CrO_2Cl_2 [64], is shown in Fig. 5, together with the individual transitions and orbitals involved. The TD-DFT calculated spectra are different from those observed experimentally as they only contain the electronic transitions, which will be superimposed on the rising edge due to the transition to the continuum in the experimental spectra. The calculated spectral components are shifted from the observed ones, and whilst it is possible to align them, this has not been done in this case. The calculations confirm that the lower energy transitions between 5925 and 5931 eV are due to transitions from the 1s core orbital to molecular orbitals that have a high proportion of Cr 3d character. Those at 5926.73, 5928.76 and 5929.33 eV are essentially dipole allowed transitions (>98% dipole character). The transition at 5927.63 eV is still predominantly dipole allowed (90%), but with a small magnetic (3.5%) and quadrupole (6%) contribution.

The transition at 5927.29 eV only has quadrupole character. These calculated spectral features correlate very well with the experimental pre-edge features at 5990 eV, including a shoulder shown in Fig. 3. The calculated weak transition at 5932.5 eV is a predominantly dipole allowed transition to a 4s type MO. The weak features at 5935 eV involve transitions to predominantly lone pairs on the Cl atoms, whilst those between 5935.8 and 5937 eV contain essentially fully allowed dipole transitions to MOs with significant p orbital character, and these correspond to the features that occur on the edge in the experimental spectrum at 6001.5 eV. The relatively weak features above 5940 eV will be masked almost entirely by the edge structure in the experimental spectrum.

The pre-edge transitions in CrO_2Cl_2 are intense compared to the majority of those observed for other 3d transition metal complexes due to a relaxation of the selection rules because of the extensive π-bonding in a tetrahedral environment. Representative sets of XANES spectra for cobalt and nickel complexes in different geometries are shown in Fig. 6 which also indicate the element specificity of the technique. The Co K-edge XANES data show the general effect of a change in oxidation state between Co(II) and Co(III) and the sensitivity of the pre-edge and edge features to the site symmetry of the cobalt [65]. In the Ni(II) octahedral complexes ($NiBr_2$ and $[(en)_2NiBr_2(en)_2]_2Br_2$) the 1s-3d transitions are very weak, and become significantly more intense in tetrahedral complexes such as $[NiBr_2(PPh_3)_2]$. In the square planar *cis*-$[NiBr_2(dppe)]$ and *trans*-$[NiBr_2(PEt_3)_2]$ complexes the intense feature on the edge is due to a 1s-4p transition [66]. Therefore, K-edge XANES spectra can be used to identify the oxidation state and site symmetry of the element under observation.

At the L-edge of the 3d transition metals the 2p-3d transitions are dipole allowed and in addition to being intense they are very sensitive to both oxidation state and spin state as shown for representative high- and low-spin compounds of Fe(II) and Fe(III) in Fig. 7 [67].

Currently, there only appears to be only one paper utilising 3d L-edge XAS to investigate matrix isolated species (see section 7.2.2 [68]), although a similar approach has been used for 2p-5d transitions in lanthanides (see section 7.9.1) and copper clusters in gas phase argon clusters (see section 7.4.2[69]). This is an area that is ripe for development for the experimental study of electronic structure in first row transition element species as the 1s-3d transitions are forbidden at the K-edges, and the d-d transitions in electronic absorption spectra are also usually weak. The ability to model the data has also improved with recent

theoretical/computational developments using either atomic multiplet [70] or TD-DFT approaches [71].

At the K-edges of the 4d transition elements, the edge features are less diagnostic as they are broadened by the relatively large core-hole lifetimes, but edge positions are often sufficiently diagnostic. The K-edges of the 5d elements are even broader and at very high energy (> 63 keV) which is beyond the energy range of most SR facilities. However, the L-edges are accessible (9 – 15 keV), and in this case the intensity of what is known as the "white line" (so called from the effect they had on the photographic plates used in the original experiments) can be used to help identify oxidation state (see section 9.6).

The K-edges of P, S and Cl have been shown to be very diagnostic of environment in a range of materials [72-80].

4.3.2. **Extended X-ray absorption spectroscopy (EXAFS)**

The EXAFS part of the spectrum beyond the edge involves the excitation of the core level electron into the continuum. This results in photoionisation of the atom, with the creation of a photoelectron and a core hole. In X-ray absorption spectra there is a long tail after the edge, because it is possible to keep pumping the core electron into the continuum as the excess kinetic energy is carried away by the photoelectron. As the photoelectron has different kinetic energies at different points in the spectrum, so does its wavelength, and it is this that gives rise to the characteristic modulation in the absorption cross-section.

The EXAFS oscillations observed after the edge in the Kr K-edge spectrum of solid Kr at 10 K (Fig. 8(b) [81]) are not present in the spectrum of liquid Kr (0.1 GPa and 298 K in a diamond anvil cell (Fig. 8(a) [82, 83]). In Br_2, EXAFS oscillations are observed for both gas phase and condensed samples. Therefore, the EXAFS oscillations must be related to "well-defined" interatomic interactions, which may be either intra- or inter-molecular in nature. However, unlike diffraction there is no need for long range order. Therefore, it is possible to obtain short-range structural data irrespective of phase.

A simple or heuristic picture of what is happening is shown in Fig. 9. The photoelectron that is ejected from the element under study (grey) propagates as a spherical (black) wave. If there

are other atoms around this atom, then the photoelectron is scattered by these, part of which results in a backscattered wave, which can then interfere with the outgoing wave. The diagram shows the case for two atoms at different interatomic distances, one of which (blue) results in constructive interference (peaks coincide with peaks), whilst the other (red) results in destructive interference (peaks coincide with troughs). As the photoelectron wavelength changes throughout the spectrum as it carries away the excess kinetic energy, this pattern of constructive and destructive interference also changes through the spectrum, and gives rise to a final state interference effect. It is this change in the interference pattern that causes the modulation of the absorption cross section, and the observation of the oscillations after the edge. If all the surrounding atoms are of the same type at the same distance, then one damped sine wave will be observed for this shell. If there is more than one shell, then a superposition of damped sine waves is observed, resulting in a complicated pattern, reminiscent of when several stones are thrown into still water.

4.4. **Data Collection**

In order to obtain X-ray absorption spectra of concentrated samples, let alone dilute matrix isolated species, an intense source of tuneable X-rays is required. In practice this means that the experiments have to be carried out at synchrotron radiation sources, where relativistic electrons (or positrons) emit a broad spectrum of wavelengths from the IR to hard X-rays after being are accelerated by a variety of magnetic devices. As the vast majority of experiments use monochromatic light rather than a broad spectrum, a means of selecting wavelengths is necessary. For low energy experiments (vac-UV, soft X-ray) diffraction gratings are used, but at higher energies single crystal silicon monochromators with specific crystal cuts (e.g. [111], [220] etc.) are used *via* application of Bragg's law. Traditionally the monochromator was operated in step scan mode, but it is now much more common to continuously sweep the monochromator and this allows for improved time resolution. Even higher time resolution can be obtained by use of an energy dispersive set-up with a bent monochromator so that the whole spectrum is collected simultaneously using a position sensitive detector after being focussed to a tight spot on the sample. (As this is effectively a transmission experiment requiring reasonable concentrations it has not found use for the study of matrix isolated species apart from a few preliminary experiments conducted by the author at the matrix gas edges.) Higher harmonics, which adversely affect the intensity of the oscillations are minimised by either detuning the monochromator, or by use of grazing incidence mirrors. There are a range of detectors available, each with different characteristics.

The beam size is defined to be compatible with the experiment, and also to optimise resolution.

The incident intensity (I_0) of the X-ray beam is usually measured with an ion chamber, although other methods are occasionally used. The simplest way to obtain the absorption spectrum is to measure the transmitted intensity (I_t) after the beam has passed through the sample with a second ion chamber. However, if the element of interest is very dilute, this will only produce a very small edge feature, and it is very difficult to accurately extract the oscillations from the data. In this case one of the two relaxation mechanisms described earlier (section 4.2.3) can be utilised. The easiest is to use the fluorescence decay path and if the fluorescence intensity (I_f) is measured it is assumed that the absorption is directly proportional to this. For matrix isolation experiments, the deposition substrate is not usually transmitting at the energies required, unless Be is used, and therefore either fluorescence or electron yield detection is employed.

4.5. Data Analysis

4.5.1. Preliminary processing and extraction

Usually a number of spectra are averaged to improve the signal to noise ratio in the spectra, especially for dilute samples such as those found in matrix isolation experiments. The data are calibrated using a spectrum of a material with a well defined and calibrated feature, and this is usually the first maximum of the first derivative in the spectrum of a thin metal foil of the element under study [84]. In order to extract the EXAFS oscillations (χ) from the raw data for analysis, there are two "background subtraction" steps that need to be employed, and these are shown in Fig. 10. The first removes the "instrument function", i.e. the spectrum that would be obtained if there was no edge present. This is also known as pre-edge background subtraction, and commonly a linear or quadratic function is used to approximate the instrument function. This results in a normalised absorption spectrum (i.e. an edge height of 1), and these are the spectra used for displaying the XANES spectra. The EXAFS part of the spectrum containing the post-edge oscillations is extracted from this normalised spectrum, by removal of the "atomic component". This is the spectrum that would be observed for the isolated (gas phase) atom, i.e. just an edge without any oscillations (although there are multi-electron excitations). This step is required in order to accurately determine the intensity of the oscillations which contain the structural information, especially occupation number. Apart from the rare gases, the atomic spectra are essentially impossible to acquire, and in all cases

they are approximated by either high order polynomials (order 5 or 6), or coupled polynomials and/or spline functions. The trick is to remove the "atomic component" and not the oscillations themselves. As part of this process the *x* axis is converted from photon energy, (eV) to wavevector (or wavenumber), *k*, Å^{-1}, using Equation 1.

$$k = \sqrt{\left[\left(2m_e/\hbar^2\right)\left(E - E_0\right)\right]} \qquad k(\text{Å}^{-1}) = \sqrt{0.2624628\left(E - E_0(eV)\right)} \qquad \textbf{Equation 1}$$

where E is incident energy, E_0 is the edge position. The first equation uses SI units, the second is in terms of eV and Å, which are the commonly used units.

This results in the extracted EXAFS oscillations plotted as $\chi(k)$ *vs*. *k*. As can be seen from Fig. 10, this results in the information content being concentrated in the low *k* region. To get a more even information content throughout the spectral range, $\chi(k)$ is multiplied by k^n, to give $k^n\chi(k)$, where n = 3 is the most commonly used weighting factor. Each interatomic distance gives rise to a damped oscillation, but in the data given in Fig. 10 there is clearly a more complex "beat" pattern and in order to get a "picture" of what is in the data, the EXAFS in *k* (wavevector, Å^{-1}) is Fourier transformed to *r* (distance, Å)) to give a pseudo radial distribution function which is used to help construct the model for fitting the data. These processes of background subtraction are shown in Fig. 10. Carrying them out properly is absolutely vital to ensure a correct interpretation of the experimental data.

4.5.2. **Simplified EXAFS Equation Using Plane Wave Approximation.**

In order to identify the information that can be obtained from an EXAFS spectrum it is illustrative to make use of an approximate form of the equation describing the propagation and scattering of the photoelectron, known as the plane wave approximation. This is so called because if the curvature of the spherical wave is sufficiently small, then it can be approximated by a plane wave. Whilst this may seem a gross over simplification, the equation contains all the pertinent terms that are included in modern analysis codes that make full use of curved wave or spherical wave theory.

The simplified EXAFS equation using the plane wave approximation is given below.

$$\chi(k) = -S_o^2 \sum_s \underbrace{\left[\left(\frac{N_S}{kR_{as}{}^2} \right) \cdot |F_S(\pi, k)| \cdot \exp\left(-2k^2\sigma_{as}^2\right) \cdot \exp\left(-2R_{as}/\lambda(k)\right) \cdot \sin\left(2kR_{as} + 2\delta_a + \alpha_s\right) \right]}$$

amplitude term frequency term

Equation 2

This equation is summed over all absorber/backscatterer pairs (Σ_s) and can be divided into two parts, one of which describes the amplitude of the oscillations, whilst the other describes their frequency.

k is the photo-electron wavevector defined in Equation 1 above and R_{as} is the distance between the absorbing and backscattering atoms.

4.5.2.1. **Amplitude terms**

N_s is the number of equivalent backscatterers (i.e. the same atom types at the same distance). The amplitude of both the EXAFS and the FT are linearly dependent on this. I.e. an oscillation from 4 similar backscatters will have twice the amplitude of one from 2 backscatterers.

$1/kR_{as}^2$ reflects the solid angle effect where the amplitude decays with distance, R_{as}, between the absorbing and backscattering atom. This puts a limit on how far EXAFS can "see" as a 10 Å R_{as} interaction will have $1/25^{th}$ the intensity of a 2 Å distance in both the EXAFS and the FT.

The $|F_s(\pi, k)|$ term describes the amplitude and phase of the back scattered photo-electron at a given value of *k*. It is very dependent on the type of backscattering atom, for example a large backscatterer like Mo will have a much larger backscattering amplitude than a small atom like O. The phase of the backscattered wave is also significantly affected by the atom type. This is the principal term used to determine the backscattering atom type.

The Debye-Waller term, $\exp^{\left(-2k^2\sigma_{as}^2\right)}$, models the thermal and static disorder in the system, i.e. σ_{as} is the mean square variation of R_{as}. At higher temperature the atoms vibrate more, so giving rise to a larger σ_{as} and therefore a lower intensity. Note that it is *k* dependent.

The electron mean free path term, $\exp^{\left(-2R_{as}/\lambda(k)\right)}$, reflects the fact that the photo-electron has a finite lifetime. $\lambda(k)$ is the electron mean free path, which is typically 10 Å at 100-1000eV. This also affects how far EXAFS can "see", as the outgoing and backscattered photoelectrons need to remain correlated. After a certain distance, the forward scattered photoelectron just dissipates into the surroundings.

The shake up and shake off factor, S_o^2, is used to take account of the fact that not all the photoelectrons participate in the EXAFS, but can get involved double excitation processes.

4.5.2.2. **Frequency terms**

The frequency of the EXAFS oscillations is given by:

$$\sin\left(2kR_{as}+2\delta_a+\alpha_s\right) \qquad \textbf{Equation 3}$$

The principal term in this is $2kR_{as}$, and whilst the frequency of the oscillations is directly proportional to the interatomic distance, the interatomic distance cannot be obtained directly as their frequency is also affected by the atomic potential of both the absorbing atom, *a*, and the backscattering atom, *s*. $2\delta_a$ is the phaseshift experienced by photo-electron on leaving and re-entering the absorbing atom *a*, whilst α_s is the phaseshift experienced by photo-electron when backscattered by the scattering atoms, *s*. Unfortunately, the consequence of this is that unlike other techniques it is not possible to "read off" the interatomic distance just from the frequency of the oscillations, but detailed calculations need to be carried out to accurately determine δ_a and α_s.

4.5.3. **Effect of Changing Parameters on the Data**

In order to fully appreciate the data content it is illustrative to appreciate the effect of changing the various parameters on both the EXAFS and the FT components of prototypical nickel K-edge data.

4.5.3.1. **Interatomic Distance, R_{as}.**

Two principal effects are observed when the interatomic distance, R_{as}, is increased, and these are shown in Fig. 11. Due to the $1/kR_{as}^2$ term the intensity of both the EXAFS oscillations and the peaks in the FT are lower. The frequency of the EXAFS oscillations is affected by the $\sin(2R_{as} + 2\delta_a + \alpha_s)$ term so that longer distances have higher frequencies, i.e. more oscillations in the same k range. The peaks in the FT appear at higher R. The difference in the EXAFS is subtle but the oscillations are more compressed in the bottom spectrum with the longer bond length, together with a lower intensity. The difference in the FT is more clear with a peak at higher r, and also with reduced intensity.

4.5.3.2. **Coordination Number, N.**

The coordination number, N, affects the intensity of both the EXAFS oscillations and the peaks in the FT. The effect on the EXAFS oscillations is linear, so the intensity at k = 4 Å^{-1} and k = 10 Å^{-1} both increase by 1.5 if the coordination number increases from 4 to 6. The FT peak increases by the same amount. This is shown in Fig. 12.

4.5.3.3. **Atom Type (Atomic Number), $|F_s(\pi,k)|$**

The intensity of both the EXAFS oscillations and the FT peaks are dependent on the atomic number of the backscattering atom. The extent of backscattering is proportional to atomic number, with heavier atoms giving a greater backscattering amplitude. In addition, the phase and shape of the amplitude envelope are also dependent on atom type. Lighter atoms (e.g. C, N, O) tend to have their maximum in the EXAFS amplitudes at lower k than heavier atoms, where the amplitude maximum is at higher k. This is the principal means of identifying atom type. When changing from Cl to P backscatters (Fig. 13) there is only a very subtle change in the EXAFS and FT. However, on going from Cl to Br (Fig. 14) the amplitude of the EXAFS oscillations increases, and the maximum of the amplitude moves to higher k. In the FT the peak has higher intensity. By changing the weighting it is possible to enhance the contribution from light and heavy backscatters.

4.5.3.4. **Debye-Waller factor , $2\sigma^2$**

The Debye-Waller factor is used to model the disorder in the system. This is not crystal disorder, but reflects a spread of distances due to either structural or thermal disorder. The effect is to dampen out the EXAFS oscillations and reduce the FT peak intensities. The

thermal disorder can be reduced by cooling the sample to either liquid nitrogen (77 K) or helium (4 K) temperatures. Unlike the change in coordination number, the reduction in the Debye-Waller factor has a non-linear impact on the EXAFS oscillations, with a much more marked increase in intensity at higher *k*, as shown in Fig. 15. It is for this reason that many experiments are carried out at low temperature as there is a significant improvement in signal to noise quality that cannot be achieved by simply averaging more data sets. In matrix isolation experiments low temperatures are always used.

The summary of all of these effects is collected together in Fig. 16.

4.5.4. **Fourier Filtering**

Having seen how changing the bond length, atom type and coordination number affects both the EXAFS spectrum and its FT, this can now be used to help construct the model for fitting the data. Just as a Fourier transform of the EXAFS data in *k*-space ($Å^{-1}$) gives rise to a pseudo radial distribution function in *r*-space (Å), it is also possible to go from *r*-space back to *k*-space (i.e.(Å to $Å^{-1}$). By Fourier back-transforming the whole data in *r*-space an EXAFS spectrum free of noise is obtained, but information content has been lost in this process. As it is impossible to know the original quality of the data it is now not regarded as good practice to use this process to "clean up" the data for publication. However, by putting a "window" over the region of interest in the *r*-space FT (i.e. each peak in turn) then "back transforming" to the *k*-space EXAFS it is possible to identify the most likely atom type contributing to that peak in the FT. This process is known as Fourier filtering and is very useful in preliminary data fitting. The CrO_2Cl_2 Cr K-edge data is a good example as it is expected to contain features due to both Cr=O and Cr-Cl. The windows are chosen so that they only contain the information from each shell. In the case of CrO_2Cl_2 where there is some overlap, the minimum between the peaks is chosen. The process is shown in Fig. 17. Fig. 17(a) gives the experimental EXAFS and FT data. The back-transform of the window over the first peak (Fig. 17(b)) gives rise to a damped sine wave with a frequency of approximately 2.5 $Å^{-1}$ and with the maximum in the amplitude at *ca*. 6-7 $Å^{-1}$. In contrast, the back transform of the second peak (Fig. 17(c)) gives a damped sine wave with a frequency of approximately 1.7 $Å^{-1}$, and the maximum in the amplitude has shifted to higher *k* at *ca*. 8-9 $Å^{-1}$, indicating that it is due to a heavier backscatterer than the first peak. Fig. 17(d) shows the data from the first and second shells summed together. In the backtransform of FF1 there is a minimum at about 5.5 $Å^{-1}$ whereas in the backtransform of FF2 there is a maximum at about this value. When

summed together, they nearly cancel out. However, around 8 $Å^{-1}$ there is constructive interference and the two peaks add together. Therefore, using Fourier filtration it is possible to identify the likely backscattering atom types.

4.5.5. **Modelling of EXAFS data.**

Having obtained the background subtracted and weighted $\chi(k)$ data, it is necessary to fit or model this data using a least squares refinement of Equation 2 in order to obtain the bond lengths, coordination numbers etc. The Fourier transform (FT) and Fourier filtering, together with chemical common sense can often give a good starting point for the analysis of the environment surrounding the absorbing atom. This is shown below in Fig. 18 for CrO_2Cl_2 at 10 K) where the EXAFS analysis [85] gave values of $Cr{=}O_2$ 1.57(2) Å and $Cr{-}Cl_2$ 2.12(3) Å compared to gas phase electron diffraction values of 1.581 and 2.126 Å [86].

4.5.6. **Multiple scattering**

In all of the above examples only what are known as single scattering events have been considered. I.e. the photoelectron leaves the absorbing atom, gets partially backscattered by a surrounding atom and arrives back at the absorbing atom to participate in constructive or destructive interference. However, in many cases, especially in cases such as metal carbonyls, there are additional scattering events which can have a profound effect on the data.

4.5.6.1. **Linear units such as metal carbonyls**

In $[Fe(CO)_5]$ (Fig. 19) there are five CO ligands surrounding each iron atom in a trigonal bipyramidal structure [87-89]. The Fe-C is *ca.* 2 Å, whilst the Fe –C is *ca.* 3 Å. The experimental Fe K-edge EXAFS spectrum and FT of $[Fe(CO)_5]$ at 10 K are shown in Fig. 20(a). From consideration of the earlier sections, it should be immediately clear that the second shell in the FT is much more intense than expected. Fourier filtering of the two shells (Fig. 20(b) and (c)) confirms that both shells comprise similar atom types as the shapes of the backscattering amplitudes are similar, and the change in frequency is as expected. However, one would expect that as the backscattering amplitude of C and O are very similar the intensity of the second shell would be *ca*. 4/9 $[(1/2^2)/(1/3^2)]$ the intensity of the first one. However, the intensity of the second peak is actually larger than that of the first one.

This is a common effect for linear arrangements of atoms such as in Fe-C≡O and is due to multiple scattering, where the atomic potential of the intervening carbon atom can be thought to be acting as a lens and focusing the photoelectron on both its outward and return journey

between the iron and oxygen atoms (enhanced forward scattering), so that a higher proportion of the photoelectron is involved than would be expected simply from the simple $1/R^2$ relationship. The most relevant multiple scattering pathways for metal carbonyl complexes are shown in Fig. 21.

This is confirmed in the theoretical fit using single scattering shown in Fig. 22(b) where the second peak is of the order of 4/9 that of the first peak. However, when the multiple scattering is included (Fig. 22(c)), the intensity of the second peak increases dramatically, and there are also significant differences in the EXAFS data. Fig. 22(d) includes both the experimental data as well as the theoretical fit using multiple scattering.

The intensity enhancement of the second shell due to multiple scattering is very angle dependent and falls off very quickly when the arrangement is non-linear as shown in Fig. 23. At 170° there is a noticeable reduction in the intensity of the second peak in the FT, by 160° the effect has all but disappeared, although the EXAFS is still different from the single scattering case. The multiple scattering cannot only increase, but also decrease, the intensity of the second shell as shown for the data at 150°. Therefore, multiple scattering can act as a sensitive method of determining bond angles, especially where the sine function is very insensitive in near linear geometries.

Metal carbonyl complexes are some of the best examples of the strong effect that multiple scattering can have on the spectra, but multiple scattering effects are noticeable in many metalloproteins especially those containing imidazole/histidine functionality as well as metals in ccp/fcc lattices.

4.5.6.2. **Multiple scattering involving the central atom**

It is also possible to observe multiple scattering at the ligand edge such as the Br K-edge as shown in Fig. 24. In *trans*-[$NiBr_2(PEt_3)_2$] the Br...Br peak (Fig. 24(b) has much enhanced intensity compared to the combined Br...Br and Br...P features in *tetrahedral*-[$NiBr_2(PPh_3)_2$] (Fig. 24(a)) [90, 91]. As for the carbonyl examples, the sensitivity of the multiple scattering effects means that it is a powerful way of determining bond angles. In addition, there are less intuitive multiple scattering pathways through the central metal atom. In the Ni K-edge EXAFS and FT of *tetrahedral*-[$NiBr_2(PPh_3)_2$] (Fig. 24(c)) there is essentially just the first

coordination $NiBr_2P_2$ shell. However, in the Ni K-edge EXAFS and FT of *trans*-$[NiBr_2(PEt_3)_2]$ (Fig. 24(d)) there is a feature in the FT at *ca*. twice the first shell distance, and this is characteristic of multiple scattering through the central metal atom. The relative contributions of the various paths are given in Fig. 25 [90]. As in Fig. 23, these multiple scattering pathways are also very sensitive to bond angle, and are only observable for linear or near linear (>155°) geometries, therefore they can act as very sensitive indicators of geometry.

Whilst multiple scattering is technically present in all spectra, and there are many other examples similar to these, it is often possible to assume that its effects are small, but it is important to beware of linear, or near linear units resulting in enhanced intensity features. It can be modelled either by considering the relevant units such as M-C-O in the presence of the other shells, or by carrying out a full 3D analysis. The former is quicker, but the latter is more accurate as it will include all potential multiple scattering pathways. However, it is necessary to know the structure reasonably accurately before starting the refinement.

4.6. Information obtained from EXAFS spectra

The above discussion indicates that EXAFS gives structural information about the local environment of the absorbing atom, as the backscattered photoelectron carries information about where it has been, i.e. the distance, atom type and number of backscattering atoms there are.

Therefore the following information can be obtained from the EXAFS data

- Interatomic distances between absorbing and surrounding atoms up to about 5 Å. (In special cases, usually involving multiple scattering, it is possible to "see" further than this.) The error of these distances is about ±1% for well defined distances.
- The atom types of the backscattering atoms can be determined. As the differences between the atomic potential of neighbouring atoms is very small, it is hard to tell Cl for S or P, but relatively easy to tell Cl from Br.
- Coordination/occupation number can be determined, but the accuracy is of the order of ±0.5 CN, i.e. can tell 4 from 5 from 6 reasonably well. However, this is correlated with the other parameters that contribute to the amplitude.

4.7. Advantages and Disadvantages of X-ray Absorption Spectroscopy

4.7.1. Advantages

- Element Specific: as the binding energy of the core electrons is different for each element, each element's K-edge (or any other edge) will occur at a unique energy. Therefore, it is possible to study the local environment around one element in the presence of other elements. A classic example is the study of superoxide dismutase (SOD) that contains both Cu and Zn. It is also possible to use multiple edge data in the refinement, together with XRD data (if available) [92].
- Local Structural Probe: as the structural information is derived from the scattering of the photoelectron, the information is a principally concerned with the first coordination shell, and then one or two further ones in favourable circumstances. This is very powerful in combination with the element specificity. The information obtained from the EXAFS part of the spectrum gives interatomic distances (±1%), coordination numbers (±0.5) and atom type of backscatterer (S from Cl challenging, Cl from Br easier). The XANES part of the spectrum gives information about oxidation state and coordination environment.
- No long range order is required: all that is required to observe the EXAFS oscillations are "well defined" interatomic distances which give "local" structural information up to about 5-10 Å. As no long range order is needed, many different types of samples, materials, phases can be studied. The real power comes from being able to study systems *in-situ* or *in-operando* so that it is possible to identify the structural changes occurring after photolysis or annealing of matrix isolated species.

4.7.2. Disadvantages

- XAFS is an averaging technique, so if there are more than one species present which contain the absorbing element, the data is a superposition of all the species present. Whilst it is possible to model systems with more than one component (e.g. high- and low-spin isomers [93]), they do need to be well defined.
- Limited angular information, bond angles can usually only be obtained by triangulation. Need to collect data at several edges to improve information content. Partially overcome by advanced data analysis using 3D coordinates for both XANES [94, 95] and EXAFS [96].

- The calculation of the phaseshift terms ($2\delta_a + \alpha_s$), and especially making them transferable, has historically been the largest constraint on the accuracy of the interatomic distances derived from EXAFS analysis. However, with the current analysis codes there is no need to routinely collect model compound data just to check the phaseshifts, but having data for comparison is very useful.
- Correlation between the amplitude terms (Debye-Waller and N) results in the relatively low accuracy of the coordination numbers, but often sufficient to tell 3 from 4, 4 from 5, etc.
- Whilst the XANES part of the spectrum has the highest signal to noise ratio it has proved challenging to extract and theoretically model all the information that is present. But with the recent developments in XANES codes this is now less of an issue.
- A synchrotron radiation source is required, these are expensive and have limited access.

X-ray absorption spectroscopy is a very powerful and useful technique for providing structural information from phases and systems that are not amenable to diffraction. It provides one of the few methods of obtaining direct structural data from matrix isolated species.

4.8. Data analysis programs and considerations

There are a number of programs and data analysis suites employed for the analysis of EXAFS data, and the most widely used are probably based on FEFF/IFEFFIT [97] including Athena, Artemis and Hephaestus [98], EXCURV [99], GNXAS [100] and FDMNES [101]. Whilst all of these based on the same theoretical background, there are some subtle differences with implementation and some use *k*-space fitting whilst others use *r*-space refinement. Whilst the EXAFS data is usually presented in the same manner in all of them, the FTs can be presented as the real, imaginary or modulus. In addition, some codes present the raw FT, and others include phaseshift effects (usually the first shell), so that care is needed in reading off interatomic distances from the FT. The errors reported in EXAFS refinements are either those given as statistical errors from the least squares analysis program, or the authors' estimate of the systematic errors. The latter are typically an order of magnitude larger than the refinement errors. In this review the errors are as given by the authors in the original report.

5. Experimental considerations of applying XAFS to matrix isolation experiments

For experiments involving relatively high energies (> 5 keV) the vacuum chamber for the matrix isolation experiments can be kept separate from the beamline and synchrotron vacuum system. However, at lower energies, the matrix experiment becomes an integral part of the machine vacuum. This clearly has implications for sample preparation and monitoring, whilst maintaining the rigorous UHV conditions of the beamline and especially the source. There is not space to discuss in detail the beamline optical components which are widely available from the facility websites, instead just the special considerations for matrix XAFS experiments.

The deposition substrate must either be made of a low Z element, usually Be, if X-rays are required to pass through the sample for transmission experiments. However, as most of the experiments are carried out in fluorescence mode, solid deposition substrates can be employed, such as Al. However, these need to be of high purity to avoid contamination of the data with low level impurities in the substrate. If (highly) crystalline materials are used, then the data can be plagued with Bragg reflections from the deposition substrate, and these can appear in different detectors (or channels) at different energies. Both of these problems, can be reduced to a certain extent by applying a coat of a highly absorbing material such as Kr or Xe to the deposition substrate.

The choice of matrix gas is also important in terms of its transparency at the energies used, as well as avoiding absorption edges due to the matrix. The attenuation length ($1/e$) of the commonly used matrix gases are plotted against photon energy in Fig. 26. As expected the penetration depth increases with energy, but reduces by about an order of magnitude after an absorption edge. As a result of this argon can be a fairly challenging matrix gas for the first row transition metal K-edges, and we have used CH_4 as this is even more transparent than Ne. As expected hydrogen matrices are essentially completely transparent above about 2 keV.

6. Combined *in-situ* FTIR – XAFS facility.

If the experiments involve pre-prepared gas mixtures then it is probably safe to assume that the conditions are very similar to those in the home laboratory if the same equipment is used.

However, for high temperature and/or reactive species it is usually necessary to prepare the samples *in-situ* at the synchrotron source using furnaces etc.. In this case there is the problem of knowing whether the sample is what is intended, even if "identical" conditions are used as at the home laboratory. For some of the early iron cluster work, Mössbauer spectroscopy was carried out on the samples before they were transferred to the beamline (see section 7.2.1). In a similar vein Young and Spicer carried out the first combined *in-situ* FTIR and EXAFS study of a matrix isolated molecule (CH_2Br_2/Ar) [102]. This employed sequential recording of the IR spectrum and the Br K-edge EXAFS spectrum, with the cryostat and vacuum chamber needing to be transferred between the two. Whilst this was practicable for experiments utilising gas mixtures, it was not feasible for those using furnaces, and does not allow for true *in-situ* monitoring of the deposition as it is taking place, or for monitoring of any subsequent annealing or photolysis reactions. Therefore, a facility that enabled the simultaneous collection of both IR and EXAFS data was established by Wilkin and Young [103]. Whilst this was initially designed to allow for collection of the IR data in either transmission geometry using a split CsI/Al deposition substrate or reflectance geometries with a high purity polished aluminium block used for both XAFS and IR, after the initial experiments it was used in the reflectance IR geometry and this is shown in its final form in Fig. 27 [103].

The IR and XAFS data can be collected simultaneously during deposition as shown in Fig. 28, which shows the monitoring of the deposition of $RbReO_4$ heated to *ca*. 500 °C and deposited in a nitrogen matrix at *ca*. 10 K [103]. The growth of the white line at *ca*. 10540 eV in the Re L_3-edge XANES spectra can be seen to grow at the same rate as the $\nu_{Re\text{-}O}$ modes in the IR spectra and as these are in very good agreement with those published previously [104-107], indicating the formation of a quality sample. A summary of the structural data obtained from both the Re L_3- and Rb K-edges of $RbReO_4$ is shown in Fig. 29 and this represented the first structural data for this molecule, and they are in good agreement with the previously known electron diffraction data for $KReO_4$ [108], $CsReO_4$ [109] and $TlReO_4$ [110].

7. XAFS studies of matrix isolated microclusters and small metal particles

7.1. Introduction

There are many definitions of what constitutes a cluster, but for the work that follows the original authors considered clusters composed of only a few atoms as molecules (dimers, trimers etc.); microclusters as small aggregates with significantly different properties from bulk samples; and clusters as larger particles having properties closely resembling the bulk, especially the crystallographic structure [111]. It is properties of the smallest clusters that are most interesting due to the large number of surface atoms [112].

As XAFS is essentially an averaging technique it is important to identify when it will be able to discriminate the structural properties of the surface atoms of the cluster, which have reduced coordination numbers, from those in the bulk. Fig. 30 shows how the surface fraction of a cubic cluster rapidly drops off with cluster size. The plot is based on a prototypical cubic cluster of iron with an interatomic distance of 2.5 Å using the approach of Roduner [112] and whilst this is an oversimplification, it is illustrative. It is important to note that for even quite small clusters the structure can be dominated by the "bulk". For example, for clusters larger than 25 Å (1000 atoms) less than half of the atoms are at the surface, so that the EXAFS data becomes dominated by the "bulk" crystallographic structure. The nearest neighbour distances in the clusters are given as *nn* and the next nearest neighbour distances as *nnn*.

Whilst there are a large number of investigations of clusters, there are relatively few that have combined matrix isolation and XAFS. The combination of a local structural probe and of being able to spatially separate the clusters in an inert rare gas matrix to avoid agglomeration with minimal perturbation, is a particularly powerful approach. (Recent work has used mass selection and soft landing to study clusters such as Cu_{19} [113]) It needs to be borne in mind that the structural motif of large clusters will essentially be that of the bulk as the fraction of surface atoms is small. It should be noted that it is only possible to get exclusively atomic species for very dilute matrices with greater than a 1000:1 dilution [114, 115].

7.2. Iron microclusters and small molecules

7.2.1. Fe K-edge studies

The first reported matrix EXAFS study was in a conference abstract published in 1979 describing experiments on iron atoms and small molecules condensed in solid argon or nitrogen [116]. For a 0.02% Fe/Ar sample, only iron monomers (corroborated by off-line Mössbauer experiments) were observed (hence no Fe-Fe distances) with a Fe...Ar distance of 3.85 Å compared to 3.76 Å expected for Ar-Ar in an fcc lattice. In the case of a 0.1% Fe/N_2 matrix three different distances were observed, with only one of them corresponding to Fe-Fe, but the value was not reported in the abstract. This preliminary work was built on by Montano and co-workers over the next decade or so.

Further investigations of a 0.1% Fe/Ar argon matrix (shown to contain only Fe monomers and dimers by off-line Mössbauer spectroscopy) were carried out by Montano *et al.* [117] The iron atoms and dimers were prepared using a resistively heated furnace. It is clear from the data in Fig. 31 that these were incredibly challenging experiments to carry out in 1980. The data analysis at this time was also still in its early stage of development and used tabulated phase shifts (which were known for iron, but had to be extrapolated from chlorine for argon) as well as the beat analysis method, rather than a least squares fitting routine now routinely employed. This data analysis indicated a Fe-Fe distance of 1.87(13) Å for Fe_2 in argon. In addition there were other features in the Fourier transform at longer distances which were interpreted as due to $Fe...Ar_{(interstitial)}$ at 2.82(8) Å and $Fe...Ar_{(subsitutional)}$ at 3.72(9) Å. The 2.82 Å interaction was considered to be very close to the sum of the atomic radii of Fe and argon, but the values of these were not given in the original paper. The atomic (metallic, bcc) radius of iron is 1.24 Å, and for argon the van der Waals radius is 1.88 Å, the radius of the octahedral hole in a fcc lattice is 0.78 Å and the radius of the tetrahedral hole in a fcc lattice is 0.43 Å [12, 14]. Therefore, it is not clear how close this value really is or what it relates to. The 3.72(9) Å value was close to that expected for a subsitutional hole in the Ar lattice (3.75 Å), but is different from that reported in the previous study of 3.85 Å [116]. The Fe-Fe distance of 1.87 Å and Fe...Ar distance of 2.82 Å were obtained by use of the "beat method", whilst the Fe...Ar distance at 3.72 Å used the "Martens" method. This method of data analysis has long been superseded by a least squares approach.

The Fe K-edge was shifted to higher energies by about 8 eV for the dimer compared to the bulk metal and this was explained on the basis that the electron binding energy is larger for

"almost" free atoms, which are in the $3d^6 4s^2$ configuration, compared to the bulk metal where the configuration is closer to $3d^7 4s^1$ [117]. It was also noted that there was a higher proportion of dimers present in these data than the notional iron composition would indicate, and this was explained by the propensity of the iron atoms to migrate in the argon matrix during the condensation process to form dimers (and higher multimers) [117].

This work was then extended to include neon matrices, using the same experimental approach (resistively heated furnace) but with higher Fe/Ne ratios of 0.4 atom %, 0.5 atom % and 1.5 atom % [118], and the data for the 0.4 at % Fe/Ne is shown in Fig. 31. The data analysis was more sophisticated employing least squares fitting rather than beat analysis. In neon matrices, the propensity for migration and oligomerisation is higher than in argon, to such an extent that the Mössbauer studies indicated the formation of iron multimers at low metal concentrations (*ca*. 1%), and that even for highly dilute samples there was no evidence for iron monomers [118]. The FT of the Fe K-edge EXAFS revealed two peaks, a shorter one comprising the Fe-Fe distances, and a second one from the Fe...Ne interactions. For the 0.4 and 0.5% Fe/Ne samples it was thought that dimers, trimers and quadrumers would be present in the matrix based on off-line Mössbauer experiments. For these two samples, the Fe-Fe distances were 2.02(2) and 2.05(3) Å, respectively. In contrast, for the 1.5 atom % Fe/Ne sample, which Mössbauer spectroscopy had shown had larger clusters (Fe_5 and above), the Fe-Fe distance had increased to 2.30(5) Å which is closer to that in α-Fe (2.48 Å). For all three of the Fe/Ne samples, the Fe...Ne interaction was very similar at *ca*. 2.4 -2.5 Å. The substitutional hole in a neon fcc lattice has a radius of 1.58 Å, whilst the radii of the octahedral and tetrahedral holes are 0.66 and 0.36 Å, respectively [12, 14], so as for the argon data it is not immediately obvious what this corresponds to.

A detailed analysis of the XANES part of the spectrum showed a shift of *ca*. 3 eV to higher energy for the small iron clusters in neon matrices compared to metal foil, which was reported to be consistent with that observed for small particles of Ni and Cu on amorphous carbon substrates [119]. This is in contrast to a value of *ca*. 8 eV reported for the argon matrix containing Fe monomers and dimers [117].

The iron small molecule work in neon matrices was also presented in conference proceedings which included a comparison of Mössbauer data in Ar and Xe matrices [120, 121]. The work on small iron molecules, and dimers in argon matrices in particular, appears to have been

continued as a revised Fe_2 bond length of 1.94(2) Å was reported in a variety of conference proceedings but scant experimental data or its analysis was presented [122-125].

The work on iron particles trapped in argon matrices was extended in 1989 to include microclusters with mean diameters of 9, 10, 12 and 15 Å prepared using a gas aggregation source [123]. (The gas aggregation source consisted of a Knudsen cell in an argon atmosphere and the metal clusters were transported by the gas stream through an aperture into a liquid helium cryopump, where most of the gas was condensed. A collimated molecular beam passed through a second aperture and was condensed with excess argon or neon onto a high-purity aluminium plate held at 4.2 K. [126].) In the case of the larger clusters it was claimed that the EXAFS data showed the presence of 3-4 shells [123], but unfortunately, there is no report which contains a detailed analysis of these data, and very sparse experimental data has been presented. Instead there are textual reports and some graphical representation of the bond lengths, but no tables of bond lengths. For example, no experimental data was presented in [123], but the FT of the Fe K-edge EXAFS data for the 9 Å particles was presented in a different set of conference proceedings in 1989 [124]. The FT for the 12 Å particles appeared in a paper in 1989 on the effect of electron mean free paths on coordination numbers [127] and the FTs for the 9, 12 and 15 Å particles were published in conference proceedings in 1993 [125] and these are shown in Fig. 32. From this rather disjointed presentation of the data it is difficult to extract a coherent picture, especially as there are no detailed reports of the data analysis, but it is clear from Fig. 32 that in the 12 and 15 Å particles the intensity of the peaks at greater distance indicate that there is much greater long range order than in the 9 Å particle.

The iron microcluster samples were prepared with mean diameters from 9 to 15 Å (with uncertainty of 1 -2 Å) using a gas aggregation source [123, 124] (with a more abbreviated report in [122]). The analysis was claimed to show the presence of 3-4 Fe-Fe shells, compared to 5 shells in bcc Fe at 78 K. However, no data was presented in [123], and whilst the FT of 9 Å particles was presented in [124] which showed one main peak and a very weak second shell, no EXAFS data was given The *nn* distance vs. particle size for the larger particles (Fig. 33) showed a small contraction of about 1% compared to bulk iron (2.48 Å), except for the smallest particles (9 Å) where a contraction of about 3% was observed. This 9 Å cluster showed the presence of a Fe-Fe distance at 3.52 Å, which was not consistent with a bcc structure. It was claimed that the ratio of 0.682 of the first and second shell distances in

the 9 Å microcluster was close to that expected for either hcp of fcc lattices and therefore indicated a crystallographic transformation around 9 Å from bcc to fcc/hcp.

A distance of 1.94(2) Å for the Fe_2 dimer was reported in the abstract of [123], but there was no mention of this in the body of the article, but it was mentioned in the text of [122, 124, 125], but with no experimental data given and no data analysis was presented.

EXAFS analysis of the 12 Å iron particles (presented as a FT) gave a coordination number of 2.9, compared to a value closer to 6 expected from analysis of the particle size [127]. This reduction in apparent coordination number for small particles is now a well known effect, but this was one of the early examples given to demonstrate the effect that particle size has on the electron mean free path and hence apparent reduced coordination number in small particles.

The final publication from Montano's group on iron molecules and clusters was in 1993 [125], when the previous work was summarised. In particular the FTs of the Fe K-edge EXAFS for the 9, 12 and 15 Å iron clusters were compared with those of Fe metal (Fig. 32) (but no EXAFS data or fits, or tabulation of the data were given). It is clear that the FT of the 9 Å cluster data is quite different from that of the 12 and 15 Å (see Fig. 32), and especially the bulk (bcc) iron as it only has one strong peak due to the first iron coordination shell, and one weak one, compared with a much more developed set of longer distance peaks. A bond length of 1.94(2) Å for the Fe_2 dimer in argon was again given, but with no supporting evidence and analysis, other than a comment that it was consistent with the earlier value of 1.87(13) Å [117].

The Fe-Fe nearest neighbour distances for these small molecules and clusters are collected together in Fig. 33. Those in the left of Fig. 33 are for the small molecules (and compared to the bulk at 100%) [118, 120, 121], whilst those in the right of Fig. 33 are for the microclusters [123, 124]. Unfortunately, the authors have not combined the data apart for the dimer.

The iron interatomic distance in Fe_2 derived from these matrix EXAFS experiments appears to be the only experimental value for this molecule [128]. Authors comparing experimental data with their calculations [129-134] usually quote the original argon matrix value of 1.87(13) Å [117] and the neon matrix value of 2.02(2) Å [118], although it is clear in the

neon matrix paper that this value has contributions from trimers and quadrumers as well as dimers. It should be noted that the commonly quoted argon value of 1.87 Å is derived using some very early data and rudimentary data analysis methodology [117], and the data that may well have some instrumental artefacts (see Fig. 31), and that Montano reported a value of 1.94(2) Å in several subsequent reports [122-125], but without any experimental evidence or analysis.

There has been considerable controversy over the ground state of Fe_2, with competing demands for $^7\Delta_u$ and $^9\Sigma_g^-$ ground terms, but it appears that the $^9\Sigma_g^-$ state is lower in energy by *ca*. 0.6 eV at all levels of calculation [131], and that the calculated bond length is *ca*. 2.2 Å (2.178 or 2.187 Å [129]; 2.190 Å [130]; 2.166 Å [135]; 2.229, 2.189, 2.164 Å, [131]), which is greater than the EXAFS derived experimental value. However, it was noted recently that the bond length in the $^7\Delta_u$ state (1.99 Å [136], 2.00 Å [137]) is closer to the experimental EXAFS data results than that of the $^9\Sigma_g^-$ state (2.16 Å) using OPBE/TZV level of theory [137].

Therefore, the experimental value of the Fe_2 bond length which is critical to identifying the ground state of Fe_2 may not be that well defined, largely because the data was collected and analysed in the very early stages of the development of X-ray absorption spectroscopy.

7.2.2. **Fe L-edge studies**

The only report of the use of 3d L-edge XAFS for matrix isolated species is an Fe L_3 edge X-ray magnetic circular dichroism (XMCD) study of small, 65-70 iron atom, clusters embedded in an Ar film on a HOPG graphite surface [68].

Fig. 34 indicates that X-ray magnetic circular dichroism (XMCD) was only observed for the iron clusters in the presence of Ar, and that when it was removed there was no dichroism due to interaction of the iron cluster with the graphite surface. The data in the absence of a magnetic field (Fig. 34) is very different for the argon matrix isolated clusters and those on HOPG. As the net magnetization is zero in the absence of argon, this was interpreted as meaning that the clusters were being driven to a non-magnetic state on interaction with the graphite surface. Preliminary L-edge experiments were reported to have been carried out Ni and Co, but there appear to be no further details.

7.3. Ag microclusters and small molecules

7.3.1. Ag K-edge studies

As for the case of iron molecules and small clusters trapped in rare gas matrices, the work on the analogous silver system has appeared in a number of full papers [111, 138], together with a selection of conference reports [120-124].

In contrast to the iron work, the larger silver particles with sizes of 25 to 130 Å prepared using gas aggregation source, were studied first [138], with the small molecule data being published later [111].

For the larger clusters no significant difference was observed between the Ag K-edge XANES of a Ag metal foil at 78 K and the 25 Å diameter Ag clusters in argon at 4.2 K [138]. The FT of the Ag K-edge EXAFS data of the 25 Å particles showed a prominent first peak, with weaker peaks due to more distant Ag...Ag shells, as well as Ag...Ar from the surface silver atoms. The first shell was used to obtain the Ag-Ag interatomic distance in the different clusters, and whilst the data was presented graphically, no tables of data were included in any of the reports. The coordination number of the first Ag-Ag shell was estimated to be 11 ±2 for the 25 Å cluster, and for the larger clusters this was 12, as expected for a fcc silver structure, with the comment that the authors did not regard the differences as being statistically significant. The observed contraction of Ag-Ag distance, was most significant when the particle size was less than 70 Å, and the contraction trend could be accounted for by a surface stress of 2286 dyne cm^{-1} (2.286 N m^{-1}) (Fig. 35).

In the absence of argon, the Ag-Ag distance was the same as that for Ag foil, confirming that the argon matrix protects and preserves the clusters. In this paper only particles down to 25 Å were studied [138], and at 25 Å it is not clear whether the additional peaks observed at longer distances in the FT were really genuine as they were only just above the noise level, and there was no attempt at fitting shells beyond the *nn* peak. This data was reported briefly in a number of subsequent conference proceedings [120, 121].

The work on silver microclusters was extended to smaller particles, including dimers, in 1989 through one major paper [111] and a series of conference proceedings [122-124]. Ag

microclusters with a wide range of cluster sizes from two to several hundred atoms in size, were prepared using a gas aggregation source and trapped in solid Ar at 4.2 K with *ca*. 0.1 at% Ag [111]. The presence of monomers and dimers was confirmed by mass spectrometry. The FTs for the 20 and 14 Å clusters are shown in Fig. 36, together with the FT for Ag foil at 78 K. Although the FTs were presented for the EXAFS data for the 9, 14 and 20 Å particles, only the 9 Å particle data was included in the table of refined parameters, together with values for 15 and 17 Å particles as well as the dimers and small multimers. There are no EXAFS spectra, or fits included in the FTs, and no data is presented for the dimer or other multimer molecules. The graphical data presented in the figure in [111], does not completely correspond to the data in the table, in terms of particle size. For example, the figure implied values of 2.49 and 2.54 Å for the multimers, but the table gave a single value of 2.51 Å.

Notwithstanding the slightly chaotic way of presenting the data, the analysis clearly indicates a strong contraction of the Ag-Ag distances for Ag dimers and small multimers compared to the larger clusters. The previous work had shown that clusters larger than 25 Å showed a small contraction of the *nn* distance and a structure consistent with an fcc lattice [138]. In the subsequent study [111] microclusters between 9 and 16 Å diameter exhibited a small *nn* expansion, together with a strong reduction or even absence of *nnn* and higher shells, indicating a different crystallographic structure for these Ag microclusters.

For clusters smaller than 14 Å, only *nn* distances were observed due to either an increase in disorder of the structure and/or reduction in coordination number due to the presence of a significant number of surface atoms for these small clusters. In the smaller clusters, Ag dimers and multimers (trimers and quadrumers) were detected, and for the very smallest clusters, dimers and monomers were observed. As the surface atoms form a considerable fraction of the cluster for the very small clusters a large number of Ag-Ar distances above 2.6 Å were identified as they could not be fitted with silver backscattering phase and amplitude parameters. Whilst it was not possible to identify a unique model to describe the location of the monomers and the multimers in the argon matrix, the data suggested that there was multiple-site trapping for the monomer, and probably the dimer as well. The interatomic distance for Ag_2 was found to be 2.47(2) Å, which was claimed to be in good agreement with the known value from optical measurements [139], but is only in reasonable agreement with the value of 2.53350(48) Å obtained subsequently from a supersonic jet experiment [140].

Fig. 37 shows a summary of the data from both reports [111, 138]. The plot of *nn* distance vs. mean cluster size revealed three main regions. From *ca*. 150 to 25 Å there was a significant and measurable decrease in the *nn* distance but the structure was still consistent with a fcc lattice. For clusters smaller than 20 Å, there was a small expansion in the *nn* distance for particles of *ca*. 16 Å diameter, indicating a change in the crystallographic structure from fcc to possibly icosahedral (in comparison with Pd data [141]). The authors reported that this significant expansion was observed in a number of independent experiments for particles in this size range. After this expansion, no significant contraction was observed as the particle size was reduced until the presence of small multimers (Ag_2, Ag_3 and Ag_4) dominated the spectrum when the Ag-Ag distance was again very dependent on particle size and there was a considerable contraction in the *nn* distances. The particle diameter for the dimer was assumed to be 4.94 Å and that for the multimers 5 and 6 Å.

Ag_8 clusters have been isolated in erionite, where the Ag K-edge EXAFS indicated a polyhedron with D_{2d} symmetry, and weak Ag-O interactions with the erionite channels [142].

7.4. Copper microclusters

7.4.1. Cu K-edge studies

Copper microclusters (7 to 15 Å mean diameter) were formed in a gas aggregation source and trapped in solid argon [126]. The Cu K-edge threshold in the XANES spectrum was found to be 1.4 eV higher in the clusters than in copper metal, and the absence of two features on the edge for particles less than 15 Å diameter was taken to indicate the absence of fourth and higher shells in these clusters. As the cluster size decreased from 15 to 6-7 Å, there was an increase in the contribution of the copper dimer to the spectra and this is shown in Fig. 38 for copper metal, 10 Å clusters and 6-7 Å clusters. The Cu-Cu distance in Cu_2 was found to be 2.23(2) Å, in excellent agreement with the existing vapour phase value of 2.220 Å [143] and subsequently published value of 2.21927(3) Å [144]. The variation in the Cu-Cu distance with cluster size is shown in Fig. 39. The microclusters of thirteen or more copper atoms (5 Å or larger) appeared stable, and to have a fcc structure, and that only small clusters showed appreciable deviation from the bulk structures. (Cu_3 and Cu_4 were not observed in this work, and this was put down to their poor stability.) Whilst considerable EXAFS analysis of the interatomic distances and coordination numbers expected for a range of structural types was presented in this paper, there was little detailed analysis of the EXAFS data of the clusters

themselves, other than a graph summarising the *nn* distance *vs*. particle size which is given in Fig. 39.

The preparation of ultra-fine (70 Å) Cu and Cu-Ag powders was carried out using what the authors claimed was "Prep-Scale Matrix Isolation" [145]. This involved the gas aggregation of copper clusters in SF_6, which was subsequently condensed, the SF_6 was then removed on heating, and the resultant sample transferred to a drybox for sample presentation as a solid.

7.4.2. **Cu L-edge studies of copper clusters in argon shells**

Mazalova *et al*. have studied small copper clusters (Cu_{13}) embedded in argon shells with a pick-up technique, and deposited onto a cold (10 K) gold substrate as well as free Cu_{13} clusters [69]. The Cu L_3-edge date for the Cu_{13} cluster embedded in an argon shell are shown in Fig. 40, together with the calculated spectra for icosahedral and cuboctahedral $Cu_{13}Ar_{42}$ clusters, the structures of which are given in Fig. 41. Peaks B and C in Fig. 40 were taken to indicate that the structural motif of the Cu_{13} core was icosahedral, which was also found for "free" Cu_{13} clusters. [69]. Analogous experiments have been conducted on mass selected Cu_{19} clusters deposited using soft landing techniques onto natural oxide layer of a Si wafer surface [113].

7.5. **Chromium microclusters and small molecules**

7.5.1. **Cr K-edge studies**

The work on small chromium clusters appeared in two conference proceedings together with data on iron and silver clusters [120, 121]. The Cr clusters were formed using an atomic beam of chromium, co-deposited with Ne onto ultrapure Al foil at 4.2 K. The Cr K-edge XANES data (Fig. 42) showed an edge shift of 5 eV for 0.1 % Cr, and 4 eV for 0.8 % and 1% Cr, compared to the bulk metal and indicated an increase in the K-electron binding energy for the small clusters.

A value of 1.70(2) Å for bond length in Cr_2, was in good agreement with earlier measurements that gave 1.68(1) Å [146] and 1.6788 Å [147]. A plot of *nn* distance *vs*. metal concentration of 0.1, 0.8, 1% and bulk, is given with the iron data in Fig. 33, and although there is evidence of a Cr-Ne interaction in the FT (Fig. 43) no analysis was given in the papers.

7.6. Manganese microclusters

7.6.1. Mn K-edge studies

There is a solitary conference proceeding report on Mn clusters in the range 8 to 18 Å which were prepared using a gas aggregation source and condensed in solid argon [124]. For clusters with mean diameters of 14, 16 and 18 Å, the structure was consistent with that of the very complex α-Mn. For smaller clusters, the Mn-Mn *nn* distance was about 0.09 to 0.13 Å shorter than in the larger clusters and the 1st and 2nd shells appeared to coalesce into a single shell. For 8 Å clusters the ratio of the first two shells at 2.65 and 3.64 Å of 0.723, was regarded as consistent with that of 0.707 expected for either fcc or hcp lattices. These results were indicative of a simpler structure (probably fcc/hcp but possibly icosahedral) for the smaller clusters than the larger ones which seemed to adopt the complex α-Mn structure. It was noted that more experiments on smaller clusters would be beneficial, but there do not seem to be any available.

7.7. Germanium microclusters

7.7.1. Ge K-edge studies

Ge clusters were the subject of three conference proceedings in 1989 [122-124]. The spectra observed for Ge microclusters (7-8 Å and 10-15 Å) deposited very fast into solid argon at 4.2 K showed a clear temporal evolution of the XANES [122-124], and also a significant increase on annealing [122]. This was ascribed to an increase in the number of empty *p* states. In contrast, samples prepared more slowly, showed no time dependence [122-124]. Only *nn* distances of 2.42 Å (7-8 Å clusters) and 2.45 Å (10-15 Å diameter clusters) were observed which were reported to be within experimental error of the bulk Ge values [122-124]. No *nnn* distances were observed. In addition to the matrix experiments, measurements were also performed on free Ge clusters travelling perpendicular to the SR beam, which were claimed to be consistent with the matrix data in one report [123], but this is contradicted elsewhere [124].

7.8. SiO clusters

7.8.1. Si K-edge

SiO clusters in solid argon were prepared with different Ar:SiO ratios from 2810:1 to 19:1 by controlling the interaction of the argon and the SiO molecular beam produced in an evaporation source [148]. The effective thickness of the Ar layer was kept below 1 μm. The

Si K-edge edge spectra (Fig. 44) were different for each of the different ratios and were different to that observed for SiO vapour [149]. The spectrum of the sample with the smallest Ar:SiO ratio resembled that of a bulk SiO film. Peak 1 at 1840 eV was assigned to the Si^{+} oxidation state, in which the Si is surrounded by three other Si and one O atom. Peak 2 at 1843.5 eV was attributed to the Si^{3+} oxidation state of a central Si atom in a $Si\text{-}SiO_3$ tetrahedron. Peak 3 at 1847 eV was attributed to Si^{4+} in which a Si atom is surrounded by four O atoms. Peaks U_1 and U_2 in the more dilute samples were assigned to two and three unsaturated Si bonds of the matrix isolated SiO clusters. There was no evidence for Si^{2+} in the spectra, even at the highest dilution and all spectra were therefore interpreted as containing tetrahedral sp^3 silicon with Si^{+}, Si^{3+} and Si^{4+} oxidation states. No direct information on the cluster size as a function of dilution was given in the paper, but analysis of possible geometries for the various oxidation states indicates that there must be at least 4-6 molecules in the clusters in the argon matrix. The vapour phase spectrum has three lines followed by a single weak absorption step, whereas the cluster spectra consist of consecutive lines and steps resulting in a rising background. There is no reference to the previously published IR work on Si_2O_2 and Si_3O_3 [150, 151] but reference is made to the theoretical work on dimers that show that the cyclic dimer is more stable than linear or OSi-SiO dimers [152]. The lack of Si^{2+} has also been noted for SiO_x thin films on a silicon substrate, where Si^{3+} and Si^{+} progressively converted to Si^{4+} as the oxygen partial pressure was increased [153].

7.9. **Rare earth clusters**

The vacant d states of the rare earths (lanthanides/lanthanoids) can be probed with L-edge spectroscopy (2p – 5d) in the energy regime of 5 – 10 keV, whereas the vacant f orbitals can be studied with M-edge spectroscopy (3d – 4f transitions) at 800 – 1700 eV.

The lanthanide/lanthanoid, or rare earth, elements have been studied in matrices as the electronic configuration changes between the atomic and bulk state for some of them depending on the size of the cluster. The nomenclature used by the physics community to describe this can be ambiguous and confusing for chemists. In the physics literature, divalent lanthanide atoms are those that are neutral but with a $4f^n6s^2$ electronic configuration, whereas trivalent means neutral atoms with a $4f^{n-1}(5d6s)^3$ electron configuration. This has been derived from the usage in the solid state for genuinely divalent and trivalent species, and because the number of f electrons is the same, its usage has been carried over by some

workers to atomic species in the gas phase and clusters in matrices. Of the rare earths, Ce, Gd, Eu, Yb and Lu atoms have divalent, $4f^n6s^2$, electronic configurations for both atomic and bulk states, whereas the remainder have a divalent $4f^n6s^2$ atomic configuration and a trivalent $4f^{n-1}(5d6s)^3$ configuration in the bulk [154, 155]. Due to the relative ease of controlling cluster size, matrix isolation techniques have been used to probe this change in electronic configuration on going from atom to bulk structures.

The L-edges (2p and 2s to 5d transitions) of samarium have been the most studied [155-158], with neodymium [155, 157] and praseodymium [155, 157] also receiving some attention. There is a solitary investigation of thulium clusters using the M_{IV} and M_V edges (3d to 4f transitions) [159].

7.9.1. **Sm L-edge, Nd L-edge, Pr L-edge studies**

For the rare earth elements that change from atomic "divalent" to metallic "trivalent" configurations the spectra show characteristic features. The intense white line peaks due to the $2p_{3/2} \rightarrow 5d$ transitions are shifted to higher energy in the metallic case as the 2p core-level binding energy is larger in the trivalent $4f^{n-1}(5d6s)^3$ configuration compared to the divalent $4f^n6s^2$ configuration. The formation of the metal 5d bands also results in additional broadening.

For Nd/Ar clusters (Fig. 45) there was an abrupt change from a "divalent" to a virtually "trivalent" configuration at M/R ratios around 500:1, which was interpreted to correspond to a critical cluster size of *ca*. 5 atoms [155, 157]. Below this size all the Nd atoms were "divalent", and above this the bulk valency of three was quickly reached. Pr behaved very similarly to Nd [155, 157].

For Sm/Ar matrices at high dilution (500:1 to 204:1) the spectra (Fig. 46) resembled those of atomic Sm, but as the Sm concentration was increased (204:1 to 6:1) the spectra increasingly took on the appearance of the metallic spectra with the $2p_{3/2} \rightarrow 5d$ transition 7.5 eV higher than in the atomic case [155, 156]. At around 100:1 there was an abrupt change from "divalent" to mixed valence (*ca*. 2.6) with a slow increase towards the bulk value of 3 as the concentration was increased (Fig. 46). This was in marked contrast to the case for Nd, where the transition occurred at much lower concentrations, and reached the bulk trivalent state

much more quickly. It was predicted that Sm required a coordination number of 10 to adopt a "trivalent" state, and as a surface atom only has 9 nearest neighbours, this explains why clusters of 13 atoms appear completely divalent as all but one of the Sm atoms are on the surface. In contrast, for Nd the predicted critical size of 5 atoms is close to a critical coordination number of 4 and the critical coordination number was 3 for Pr.

For Sm/Ne matrices (Fig. 46) much higher dilutions were required to observe atomic like spectra, and the valency was found to be dependent on the thickness of the aluminium substrate. Thinner substrates required higher dilution to obtain the same proportion of divalent atomic Sm [158]. In contrast for Sm/Kr atomic-like spectra were observed (Fig. 46) down to concentrations of around 100:1. (It should be noted that the cluster size ordering is reversed for Sm/Ar [141, 142] in Fig. 46, compared to Sm/Ne or Sm/Kr [158].)

The Sm L_3-edge EXAFS data for neon matrices with M/R of *ca*. 100 gave an average coordination number for each Sm of 6 ±1 [158]. For Sm this critical cluster size was found from EXAFS to be 13 (±3) as the coordination number was implying a central Sm surrounded by twelve other samarium atoms, implying that the vast majority were surface atoms. Below this all the Sm atoms were "divalent", with a slow increase in valency above this, so that there was mixed-valence.

The EXAFS spectra of Sm/Rg with valency of > 2.5 (more dilute samples were too challenging) showed only Sm-Sm interactions and no Sm-Rg shells. In contrast to the previous work on micro-clusters, the larger clusters had shorter metal – metal distances (see Fig. 47) as divalent Sm has a larger atomic radius [158]. The coordination number dropped from 12 for the bulk samples to around 5 – 6 for the clusters with an intermediate valence of 2.6 (Fig. 47). On the assumption of fcc structures this was taken to mean that the cluster sizes were 13 ±3 atoms. A cluster size of 13 can be interpreted in terms of magic numbers where there is a closed shell of 12 atoms surrounding a single central atom. This was much smaller than the predicted value of around 1000 atoms to get a mean valence of 2.5, which was in agreement with a 30 Å particle size determined by electron microscopy. The low critical size for Sm/Rg systems was surprising and means that for clusters larger than 13 mixed valence is present, and this was attributed to matrix effects, and in particular the internal pressure exerted on the clusters by the distorted rare gas lattice. For Ne, Ar and Kr, the Sm critical valence was between 2.60 and 2.55.

The Ar K-edge EXAFS and FT data for solid Ar and of Sm clusters with a mean valence of 2.85 trapped in solid argon were nearly identical, with only Ar-Ar distances being observed and no Ar-Sm contributions being detected. For the solid argon data an Ar-Ar first shell distance of 3.75 Å was obtained, compared to 3.70 Å for the argon matrix containing the samarium clusters [158].

7.9.2. **Tm and Sm M-edge studies**

The 3d – 4f, M_5 spectra of Tm clusters in argon matrices are shown in Fig. 48 and indicate a very sudden change in valency/4f orbital occupancy. The very dilute matrices (M/R >3000) gave spectra very similar to those of the vapour with just one peak due the single allowed transition from the $3d^{10}4f^{13}$ ($^2F_{7/2}$) to the $3d^94f^{14}$ ($^2D_{5/2}$) level [159]. In contrast, spectra for ratios of 220:1 and below resembled the spectrum of solid Tm with four features in the spectrum (a weak feature observed on the M_4 edge for Tm solid was not shown in Fig. 48). For Tm, the trivalent state persisted down until the cluster size was 6 whereas for Sm the clusters were exclusively divalent for N < 10. As surface coordination is 9, this means that all the surface atoms in Sm clusters will be divalent, but for Tm surface divalence can only occur on rough surfaces.

The Sm M-edge experiments indicated that the spectrum of the hot vapour required the inclusion of both the ground level ($^7F_0$) as well as a Boltzmann distribution of excited levels ($^7F_1$ and $^7F_2$), and was similar to that of solid divalent Sm, whereas the spectrum of the matrix isolated cluster closely resembled that calculated by Dirac-Fock calculations if only the $^7F_0$ level was included. The M-edge rare earth work has been reviewed [160, 161].

7.10. **Alkali halide clusters**

7.10.1. **K K-edge studies**

Teodorescu *et al.* have studied alkali halides in the vapour [162, 163] and the solid state [163], and have used matrix isolation [164, 165] to identify the critical cluster size (<N>) when the behaviour resembled that found in the solid state. Fig. 49 shows that as the cluster becomes smaller, the spectral features change from those of the bulk. However, for small KF cluster sizes (<N> = 2) a spectrum characteristic of molecular behaviour in the vapour phase was not observed, instead it was characteristic of an alkali metal with just an absorption jump

at the Fermi level [164]. This was taken to imply that small cluster sizes are non-stoichiometric, with a higher relative abundance of alkali metal compared to halogen. This was confirmed by mass spectrometric observations. In addition, a shoulder on the edge (M) was assigned to matrix isolated monomeric KF, which was not observed in the analogous NaF spectra [165]. This shoulder was not visible in the spectrum of a cluster with average size <N> of 18 atoms, but started to become observable in the spectrum of a 9 atom cluster. The peak (N) was tentatively assigned to the presence of negative alkali ions in the rare gas matrix. It needs to be noted that the spectra for the smallest clusters, especially <N> = 2 have quite poor signal:noise characteristics, thus making firm conclusions quite challenging.

7.10.2. **Na K-edge studies**

In the analogous NaF system, the three peaks (1), (2), (3) observed in the Na K-edge spectrum (Fig. 50) for solid state NaF become less and less resolved as the cluster size (<N>) decreased [165]. Band 1 was attributed to discrete exciton structures of mainly 3p character of the absorbing Na^+ and to a transition on a state resulting from the hybridisation of the 4p, 5s and 3d orbitals of the absorber. Band (2) was attributed to transitions to a state resulting from the hybridisation of the 4p, 5s and 3d orbitals of the absorber with some contribution from higher unoccupied orbitals of the second-order Na^+ neighbour. Band (3) which lies in the continuum of inner-shell excitations of a free Na^+ ion, is interpreted as a multiple scattering feature in which the photoelectron in the continuum is trapped inside the 'anionic cage' formed by the surrounding six F^- ions. For the spectrum of the NaF molecule, band (b) was interpreted as being the $1s \rightarrow 3p$ transition in the Na^+ absorbing atom, where this state is highly localised on the absorber. Band (a) represents transitions on a state formed mostly by hybridisation of the 3s and 3p orbitals of the free Na^+ ion. For small clusters with around 11 atoms, the threshold (edge) region was more similar to that of Na metallic clusters than of the vapour phase NaF molecule. This was interpreted to mean that low sized NaF clusters exhibit metallic character, as observed for the KF clusters, and this was confirmed by mass spectrometry.

Analogous work on NaCl clusters generated using an argon pick-up method and then studied either as free clusters or embedded in solid argon has also been published, where the changes in the Na-Cl bond lengths with cluster size could be extracted from the multiple scattering features (marked as g in Fig. 51, the assignment of the other peaks is given in the original

papers [166, 167]) and compared with theoretical calculations [166, 167]. This gave values of 2.68(5) Å for a 50 molecule clusters, 2.69(5) Å for 36 molecule clusters, 2.68(5) Å for 30 molecule clusters and 2.59(5) Å for 9 molecule clusters.

7.11. **Alkali metal clusters**

7.11.1. **Na K-edge studies**

In contrast to the work on the alkali halides, there is a transition from metallic to non-metallic behaviour for sodium clusters [165]. The vapour phase spectrum had been published previously [168]. The spectra (Fig. 52) of the clusters with an average <N> of 7.3 and 28.1 atoms were very similar to those of solid sodium with just an absorption jump. The spectrum of a cluster with an average <N> of 1.6 atoms was very noisy and was thought to be significantly different from those of the larger clusters, although it is not very clear that there is much more information as only the edge was present. In particular the weak feature **B** at 1075 eV, barely above the noise level, was attributed "with no doubt to the $1s^{-1}3s3p\ ^3P$ state of matrix isolated Na atoms" [165]. A second weak peak, **A**, in the pre-edge region was tentatively assigned to the dipole forbidden 1s → 3s transition, activated by the inhomogeneous field in small aggregates. Sodium clusters of a few atoms were essentially metallic as no well-resolved individual excitation spectra were observed. The only exception was the sodium dimer to which the weak pre-edge feature was assigned.

7.12. **Conclusions**

What is clear from this work on clusters is that at the very high dilutions sometimes required for matrix experiments, the interpretation of the data can often be hampered by the signal to noise characteristics. However, it does enable structural data to be obtained from the very smallest clusters that are stabilised in cryogenic matrices.

8. **XAFS studies of matrix isolated organic compounds**

There are very limited reports of matrix XAFS of carbon species utilising the C K-edge at 284 eV, or other low z elements, as these can be experimentally very challenging. The only report [169] involves calculations of neopentane in a Ne cluster to support C K-edge NEXAFS experiments on vapour phase and condensed phase neopentane which gave very different spectra. The advent of X-ray Raman spectroscopy (see section 12.2) may open up the study of carbon and other second period elements.

Young and Spicer investigated CH_2Br_2 in an argon matrix using the Br K-edge whilst demonstrating the feasibility of recording IR and EXAFS data from the same sample [102]. The Br-C (1.95(2) Å, Br...Br (3.19(3) Å), and Br...Ar distances (3.75(4) Å) were in good agreement with previous work.

9. XAFS studies of matrix isolated inorganic compounds and complexes

One of the major applications of X-ray absorption spectroscopy to matrix isolated species has been in investigating the structural chemistry of inorganic species, as absorption edges for both the transition metals and heavier main group elements are readily accessible. This work was originally pioneered by Beattie, and later developed by Young, and there are other reports as well.

9.1. Chromyl chloride (CrO_2Cl_2) – Cr K-edge

To confirm the suitability of matrix-EXAFS to the study of transition metal halides, CrO_2Cl_2 was used as a demonstration molecule both in a nitrogen matrix and as a condensed solid at 10 K and 130 K (see section 4.5.5 and Fig. 3, 10, 17, 18 for spectra) [85]. Whilst vapour phase electron diffraction data were available for CrO_2Cl_2 [86], there was no structural data for the solid state. The Cr-O and Cr-Cl bond lengths of 1.58(2) Å and 2.10(3) Å were in good agreement with the electron diffraction, r_g, values of 1.582(2) Å and 2.126(2) Å [86]. Other than an improvement in signal to noise quality, there were no significant differences between the structural parameters obtained from a nitrogen matrix and the solid state at either 10 or 130 K.

9.2. 3d transition metal carbonyl halides

9.2.1. *cis*-iron carbonyl halides – Fe K-edge studies

The *cis*-iron carbonyl halides are well known [170] whereas the *trans* analogues are much less stable and are best prepared using metal halides trapped in either CO doped argon matrices or neat CO matrices. A preliminary report on *cis*-$[Fe(CO)_4I_2]$ studied at the Fe K-edge after being sublimed at 2-4°C into a methane matrix at *ca.* 10 K yielded the bond lengths given in Table 1 [81], which included multiple scattering as described in section

4.5.6.1. This work was subsequently repeated and expanded to include *cis*-$[Fe(CO)_4Br_2]$ trapped in a methane matrix at 15 K [170] and the data are given in Table 1. Although other spectroscopic data was reported on the mixed carbonyl halides [170], Fe K-edge EXAFS data was not collected as there would be appreciable proportions of the diiodide and dibromide complexes as well as well as *cis*-$[Fe(CO)_4BrI]$, making the analysis complex. The difference in Fe-C bond lengths in *cis*-$[Fe(CO)_4I_2]$ between the early analysis using EXCURV88 [81] and later analysis using EXCURV98 [170] is quite marked, and reflects the increasing accuracy of data analysis, especially the treatment of multiple scattering as the analysis programs and computational resources improved. For $[Fe(CO)_5]$ there was much less of a change in the accuracy of the Fe-C and Fe-O distances compared to electron and X-ray diffraction data on going from EXCURV90 [171] to EXCURV98 [170]. As the original *cis*-$[Fe(CO)_4I_2]$ data [81] was analysed using EXCURV88, a more significant improvement is to be expected in this case. This is an important point and should be borne in mind when dealing with relatively old EXAFS analysis, especially where multiple scattering is present.

9.2.2. *trans*-$[Fe(CO)_4Cl_2]$ and *trans*-$[Cr(CO)_4Cl_2]$ – Fe and Cr K-edge studies

As part of a detailed investigation of the formation of 3d transition metal carbonyl chlorides stabilised in cryogenic matrices, a combination of IR and EXAFS was used to characterise *trans*-$[Fe(CO)_4Cl_2]$ and *trans*-$[Cr(CO)_4Cl_2]$ [171]. The IR data for $FeCl_2$ isolated in solid CO at *ca.* 10 K, using $^{12}CO/^{13}CO$ and $C^{16}O/C^{18}O$ isotopic substitution showed the unambiguous presence of *trans*-$[Fe(CO)_4Cl_2]$. The Fe K-edge EXAFS and FT of $FeCl_2$ isolated in solid carbon monoxide are shown in Fig. 53(a) and the Fe-C, Fe-O and Fe-Cl interatomic distances (obtained from EXCURV90) are given in Table 1, together with values for $[Fe(CO)_5]$ analysed at the same time (where it was not statistically valid to separate the axial and equatorial distances). The stoichiometry of the complex was confirmed by varying the number of CO ligands in the refinement and recording the fit index, and in this case (Fig. 54) the best fit was obtained for four CO ligands. The Fe-C distance in *trans*-$[Fe(CO)_4Cl_2]$ was slightly longer (1.85(3) Å) than that in $[Fe(CO)_5]$ (1.80(2) Å), whilst the Fe-O distance was very slightly shorter in *trans*-$[Fe(CO)_4Cl_2]$ (2.96(4) *vs.* 2.97(4) Å), both of which are compatible with the differences in π-bonding.

In the case of $CrCl_2$ in neat CO matrices the IR data were unable to give an unambiguous assignment of the number of CO ligands attached to the metal centre [171]. However, by

using the Cr K-edge EXAFS data (Fig. 53(b)) and the same approach as for iron and plotting the fit index against the CO occupation number (Fig. 54) it was possible to confirm that *trans*- $[Cr(CO)_4Cl_2]$ was formed when $CrCl_2$ was condensed in solid CO at 10 K. The Cr-C and Cr-O distances were both longer in *trans*-$[Cr(CO)_4Cl_2]$ (2.00(3) Å and 3.11(5) Å) than in $[Cr(CO)_6]$ (1.89(3) Å) and 3.02(4) Å).

IR data obtained for $NiCl_2$ in neat CO matrices indicated the formation of *trans*-$[Ni(CO)_2Cl_2]$ and *tetrahedral*-$[Ni(CO)_2Cl_2]$ [171]. The data for $CoCl_2$ isolated in neat CO also indicated the presence of more than one species, but it was not possible to determine the stoichiometry of these [171]. EXAFS experiments were not carried out on either the $NiCl_2$/CO or $CoCl_2$/CO systems, because of problems of unravelling the spectra of mixtures at that time.

9.3. Fe_2Cl_6 – Fe K-edge

The Fe K-edge XANES and EXAFS spectra of Fe_2C1_6 isolated in N_2, Ne and Ar matrices were used to confirm the suitability of the approach to investigate vapour phase transport reactions utilising either $FeCl_3$ or $AlCl_3$ [172]. The Fe K-edge XANES spectra (Fig. 55(a)) of each of these had a relatively intense pre-edge feature at *ca.* 7115 eV (N_2, 7114.7 eV; Ar, 7114.9 eV; Ne, 7115.0 eV), and these together with the overall spectral features are essentially identical to the spectrum of $(Et_4N)[FeCl_4]$ published a few years afterwards [173]. Therefore, the spectra are completely consistent with tetrahedral coordination, indicating the presence of the chlorine bridged Al_2Cl_6 dimer. After the matrix was allowed to boil off (Fig. 55(d)), this feature was replaced by a weaker pre-edge feature at 7112.5 eV, which is characteristic of iron in an octahedral environment [173]. The analysis of the Fe K-edge EXAFS data for Fe_2C1_6 isolated in solid nitrogen gave values of 2.12(3) Å and 2.30(3) Å for the terminal iron chlorine and bridging bond lengths, respectively and 3.15 (5) Å for the Fe ...Fe interaction yielding a Cl_b-Fe-Cl_b bond angle of 94°. A summary of this data is given in Fig. 56. The previous electron diffraction values for the Fe-Cl values in a puckered four-membered ring structure were 2.127(4) Å and 2.326(5) Å whilst the Fe...Fe distance was 3.234(8) Å [174]. The argon matrix data were similar in terms of Fe-Cl distances, but the Fe...Fe distance was more poorly defined with a large Debye-Waller factor, and there was no identifiable Fe...Ar interaction. Although the Fe K-edge XANES data for the Ne matrix data were similar, there was a loss of resolution and the EXAFS data was poorer, both reflecting the problems of using Ne matrices at *ca.* 9 K.

9.4. First row transition metal dichlorides – Cr, Fe, Ni and Zn K-edges

A detailed investigation of first row transition metal dichlorides isolated in a variety of matrices showed that there was a very good correlation between the EXAFS determined bond length and the vibrational frequency using a Badger's rule approach [175]. Initially, the validity of this approach was verified using bond lengths derived from gas phase electron diffraction data and vibrational data from argon matrices. The plot of EXAFS derived M-Cl bond lengths *vs* $k^{-1/3}$ for the matrix isolated data (assuming linearity) is shown in Fig. 57 (*k* is the SVFF force constant derived from the asymmetric stretching mode of the dichloride). The correlation is excellent (99.55%) for the $CrCl_2$, $FeCl_2$ and $ZnCl_2$ data, but the two points for the $NiCl_2$ data lie quite a way off the line. The IR spectra of $NiCl_2$ in nitrogen matrices [176, 177] indicated that it was severely bent *(ca.* 130°) and if this is taken into account in the force constant calculation (1.90 mdyne $Å^{-1}$) the point moves to the left to 0.8073 (mdyne $Å^{-1})^{-1/3}$ which brings it into closer agreement with the other data. The $NiCl_2/CH_4$ data point lies on the other side of the line implying that for the observed IR vibrational frequency, the EXAFS derived Ni-Cl bond length is too long. The Ni and Cl isotope pattern in the IR spectra were consistent with a linear geometry [176, 177], and if the IR data are used to predict the bond length using the best fit straight line, then a value of 2.07 Å is obtained which is in very good agreement with the electron diffraction r_g value of 2.076(4) Å [178]. Therefore, it appears that the Ni-Cl bond length for $NiCl_2$ in solid CH_4 derived from EXAFS is too long. This is most probably due to the presence of species other than monomers in the matrix, and this kind of observation was the driving force in developing *in-situ* IR monitoring during the deposition and any subsequent photolysis or annealing as described in section 6 [102, 103]. The IR data for $FeCl_2$ in a nitrogen matrix indicated a slight loss of linearity (150°) [177] and $CrCl_2$ is expected to be subject to a Renner-Teller distortion and the electron diffraction data and computational studies indicate a bond angle of 150° in the vapour [179], although the earlier argon matrix IR data for $CrCl_2$ [180] and $CrBr_2$ [181] were consistent with a linear geometry. Using these bond angles results in the data points for both $FeCl_2/N_2$ and $CrCl_2/N_2$ moving horizontally by *ca*. 0.01 (mdyne $Å^{-1})^{-1/3}$ compared to *ca*. 0.03 (mdyne $Å^{-1})^{-1/3}$ for the $NiCl_2/N_2$ data.

In addition to the metal chlorine interactions other features were observed in the FTs at more remote distances that were fitted to M...Ar, N or C interactions [175]. However, some of

these are almost certainly due to multiple scattering paths through the central atom in linear MCl_2 units described in section 4.5.6.2 [90, 91], and this is especially the case for the $ZnCl_2/N_2$ data presented in [175]. These were not able to be modelled at the time, but could be with more recent versions of the analysis code. Therefore, their interpretation needs to treated with some caution. As highlighted previously, some caution needs to be exercised when considering the analysis of old data.

9.5. $NiBr_2$ – Ni and Br K-edges

As it had been shown previously using IR spectroscopy that that $NiCl_2$ was severely bent in a N_2 matrix [175, 177] and the Ni K-edge EXAFS derived bond length had been consistent with this [176] it was decided to use the newly commissioned combined IR/EXAFS facility described in section 6, to investigate $NiBr_2$ in CH_4 and N_2 matrices. $NiBr_2$ is advantageous as it allows for a direct determination of the $NiBr_2$ bond angle from triangulation using the Br K-edge data, which is at a more tractable energy (13474 eV) than the Cl K-edge (2822 eV). The ν_3 asymmetric stretching mode for $NiBr_2$ trapped in an argon matrix was at 419.2 cm^{-1}, and the well resolved nickel isotope pattern was consistent with a bond angle of 180° [182]. For neon (423.4 cm^{-1}), krypton (413.2 cm^{-1}), xenon (410.6 cm^{-1}), methane (410.6 cm^{-1}) and oxygen (409.1 cm^{-1}) matrices small shifts were observed, and the nickel isotope pattern was consistent with a linear geometry. In contrast, when a N_2 matrix was used, the ν_3 mode was located at 331.9 cm^{-1} and the nickel isotope pattern was consistent with a bond angle of *ca*. 125° [182].

In the original publication [182] no ν_{NN} modes were reported for $NiBr_2$ isolated in N_2. However, with the later use of $^{15}N_2$ matrices it was possible to identify ν_{NN} modes on deposition at 2263.8 and 2259.4 cm^{-1} [183] in addition to the perturbed ν_{NN} mode of $^{15}N_2$ at 2250.0 cm^{-1} [184]. With this information it was then possible to identify ν_{NN} modes in $^{14}N_2$ matrices at 2336.9 and 2342.8 cm^{-1} on deposition [183] very close to the CO_2 bands, as well as the perturbed ν_{NN} mode of $^{14}N_2$ at 2327.8 cm^{-1} [184]. Without the $^{15}N_2$ data it was impossible to identify the $^{14}N_2$ features with any certainty. On broad band Hg-Xe photolysis a small proportion of these physisorbed species were converted to $NiBr_2(\eta^1\text{-}N_2)_2$ complexes with ν_{NN} modes at 2205.7 and 2186.4 cm^{-1} for $^{14}N_2$ and 2281.4 and 2261.4 cm^{-1} for $^{15}N_2$ [183], close to those previously observed for $Ni(\eta^1\text{-}N_2)_2(\eta^2\text{-}O_2)$ complexes [185, 186].

For the XAFS experiments CH_4 was used as a matrix as it is much more X-ray transparent than Ar (see Fig. 26), and the cryostat available had a base temperature of *ca*. 10 K which was not suitable for Ne matrices, especially for high temperature species. The Ni K-edge XANES for $NiBr_2$ isolated in CH_4 and N_2 matrices are given in Fig. 58 and they show a very dramatic change from methane to nitrogen matrices. Whilst metal K-edge XANES spectra are well known to be diagnostic of metal oxidation state, coordination number and geometry (see section 4.3.1) there are very few examples in the literature of XANES data for triatomic first row transition metal species. The best examples of these are for copper where Kau *et al.* demonstrated that the intensity of a characteristic 1s-4p edge feature in Cu(I) complexes was dependent on the copper coordination number [187]. This has subsequently been widely used as a diagnostic probe of the electronic and geometric structure of copper in metalloproteins [188]. Of more relevance to this work is that of Fulton *et al*. who investigated $[CuCl_2]^-$ and $[CuBr_2]^-$ formed under hydrothermal conditions [189, 190]. In both cases, a very intense edge feature was observed and based on the work of Kau *et al.*[187] these were assigned to 1s-4p transitions. Therefore, this pre-edge feature can be taken as an indicator of linearity in triatomics, and the fact that it was clearly absent from the Ni K-edge XANES of $NiBr_2$ in N_2 confirmed a radical change in geometry.

The Ni K-edge and Br K-edge EXAFS and FTs for $NiBr_2$ isolated in CH_4 and N_2 matrices are shown in Fig. 59. It is also clear from these that there are significant differences between the CH_4 and N_2 data. The Br K-edge data are straight-forward to interpret and analyse with a Br-Ni shell and a Br...Br shell, and by simple triangulation the Br-Ni-Br bond angle can be determined. The greater intensity in the FT of the $NiBr_2/CH_4$ data is due to the multiple scattering in the linear Br-Ni-Br unit (see section 4.5.6.2). With light matrix scatterers such as C and N there is as expected very little contribution from the matrix. The Ni K-edge data is not so straight-forward, and rather surprisingly there is an intense feature at *ca*. twice the Ni-Br distance in the FT for the CH_4 matrix data, and evidence of light scatterers in the low *k* region of the N_2 matrix data. The first of these is due to multiple scattering through the central Ni atom (see section 4.5.6.2), but this could not be modelled with the analysis programs available (EXCURV92) at the time of the original publication [182]. Subsequently these features were shown to be due to multiple scattering through the central atom, and also to be very diagnostic indicators of linearity [90, 91] (see section 4.5.6.2). Therefore, the theoretical fits shown in Fig. 59 for $NiBr_2$ in a CH_4 matrix are those derived using this

approach with the more recent analysis suite (EXCURV98), and for consistency the other data in Fig. 59 has also been re-analysed.

The original Br K-edge EXAFS data for $NiBr_2$ in a CH_4 matrix gave $r_{Br\text{-}Ni}$ of 2.19(3) Å and $r_{Br\ldots Br}$ of 4.36(6) Å [182], whilst re-analysis gave essentially the same values of 2.20(2) Å and 4.38(4) Å, respectively. Both of these sets of data imply a bond angle of 170°, which given the insensitivity of the sine function close to 90° can be taken as linear in both cases. These values are in good agreement with the r_g value of 2.201(4) Å derived from electron diffraction experiments [178]. For $NiBr_2$ in a N_2 matrix the original analysis of the Br K-edge data gave $r_{Br\text{-}Ni}$ 2.27(3) Å and $r_{Br\ldots Br}$ of 4.34(6) indicating a bond angle of 145° [182], whilst re-analysis yielded similar values of $r_{Br\text{-}Ni}$ 2.29(3) Å and $r_{Br\ldots Br}$ of 4.33(5) Å, indicating a bond angle of 142°. The most recent analysis of the Ni K-edge data using the full multiple scattering approach for $NiBr_2$ in a CH_4 matrix gave a Ni-Br bond length of 2.20(2) Å (compared to the original of 2.19 Å), with a good fit to the feature at *ca*. 4.35 Å indicating a linear geometry. Whilst the re-analysis for these three sets of data made no significant difference to the overall picture, the re-analysis of the $NiBr_2/N_2$ data does have more significant implications. It is clear from the Ni K-edge EXAFS (Fig. 59) that there are light scatterers involved, and there is a feature at *ca*. 3.2 Å in the FT with which these are associated. However, it was not possible to fit the data to a Ni-Br shell at *ca*. 2.3 Å and just a Ni...N interaction at 3.2 Å, a second Ni...N shell at a shorter distance was required. In the original analysis the Ni-Br distance was 2.25(3) Å (compared to Br-Ni of 2.27(3) Å) and it was not possible to fit the data with a short Ni-N distance, but the best fit was to a shell of four nitrogen atoms at 2.61(4) Å and 12 nitrogen atoms at 3.21(5) Å [182]. This led to the conclusion that "there appears to be no *convincing* evidence for a short Ni-N interaction" [182]. When this data set was re-analysed, a similar solution with Ni-Br of 2.26(3) Å, and Ni-N of 2.6 and 3.2 Å was still a possibility, but the occupation numbers for the nitrogen shells were now two. However, a second fit involving Ni-Br of 2.29(3) Å and Ni-N of 2.12(3) and 3.19(5) Å was also located which was not found in the original refinement. This latter fit is in much better agreement with the Br K-edge data (2.29 Å) and the fitting parameters, including the E_f parameter, are also much more reasonable, and therefore it is believed that this is a more physically realistic model. The Ni-N distance of 2.12(2) Å is longer than that found in either end-on (1.792 Å) [191] or side-on (average of 1.92 Å) [192] complexes and indicates the formation of a relatively weak bond due to limited back bonding from Ni(II). The N≡N distance of 1.07 Å is in good agreement with that of N_2 in the solid state (1.075 Å [193]).

This is also consistent with the observation of ν_{NN} modes observed to high wavenumber of free N_2 in the IR spectra on deposition [183]. Therefore, the combination of the IR data and the analysis of the EXAFS data using more accurate analysis program indicates that there are most probably two nitrogen ligands weakly associated with the bent $NiBr_2$ unit on deposition, akin to physisorption, and that a small fraction of these can be converted by photolysis to a species where there is greater back-bonding resulting in a situation closer to chemisorption. As the fraction of the physisorbed species converted to chemisorbed on photolysis was very low, EXAFS was not recorded for these experiments. A detailed description of this work, together with other dibromides is in preparation.

9.6. $PtCl_2$ – Pt L_3 -edge

As part of an investigation of the products formed between the reaction of Pt atoms generated in a hollow cathode sputtering device and Cl_2 doped argon, Pt L_3-edge XAFS was used to characterise the species present [194]. From IR and UV-vis-NIR data it was clear that with a Cl_2/Ar ratio of 1% or 0.5% there were at least two species present, whereas at 5% Cl_2/Ar there appeared to be only one species present. Unfortunately, the Cl isotope pattern was not resolvable in such concentrated matrices. The XAFS experiments were carried out using a 5%Cl_2/Ar sputtering mixture to ensure the greatest probability of producing just one species. The Pt L_3-edge at *ca*. 11560 eV was used for these experiments as the Pt K-edge at 78395 eV is beyond the range of current spectrometers, and the core hole lifetime/broadening at these energies would significantly wash out any structure in the spectra. Whilst the edge position and shifts of XANES data are useful in oxidation state determination at the K-edges, at the L_3-edge they are less useful because the spectra are dominated by intense, dipole allowed, transitions arising from $2p^6 5d^n$ to $(2p_{½})^2(2p_{3/2})^3 5d^{n+1}$ transitions. The positions of these so-called "white lines" are affected by changes in the energy of the 2p core states and the 5d valance orbitals in different coordination environments as much as the change in the formal oxidation state. However, the intensity of the white line can be used diagnostically to identify oxidation states as it is very dependent on the number of holes in the 5d manifold, as shown in Fig. 60 where the intensity of the "white line" is greater for $K_2[PtCl_6]$ (Fig. 60(a)) than for $K_2[PtCl_4]$ (Fig. 60(b)). The intensity of the white line in the spectrum of the products when Pt was sputtered with 5% Cl_2/Ar (Fig. 60(c)) was very similar to that of $K_2[PtCl_4]$ (Fig. 60(b)) indicating the formation of a Pt(II) compound. The lack of any significant Pt atom concentration was confirmed by comparison with Fig. 60(d). Analysis of the Pt L_3-edge

EXAFS data gave a bond length of 2.19(2) Å for molecular, linear $PtCl_2$, shorter by 0.12 Å than observed for $K_2[PtCl_4]$ or $K_2[PtCl_6]$, and this represented the first structural data for this molecule [194]. The combination of IR, UV-vis-IR and XAFS data as well as DFT calculations was necessary to identify the species present in this case.

9.7. $AuCl_3$ – Au L_3 edge

A similar investigation of vapour phase gold chlorides was also carried out, and a combination of IR, UV-vis-NIR, XAFS and DFT calculations showed conclusively that $AuCl_3$ did not have D_{3h} symmetry in an argon matrix, but that the data were consistent with it having a T-shaped Jahn-Teller distorted geometry [23]. The Au L_3-edge EXAFS data (Fig. 61) indicated the Au-Cl bond length was 2.22(2) Å in $AuCl_3$, 0.06 Å shorter than in $[AuCl_4]^-$.

9.8. HgF_2 and HgF_4 - Hg L_3 edge

Compounds with mercury in oxidation states higher than Hg(II) are elusive species, but are very significant. Once confirmed this would result in re-thinking the boundaries of transition and main group elements in the periodic table as both Hg(III) and Hg(IV) would have partially filled d manifolds. Whilst there had been calculations indicating the stability of higher mercury oxidation states for a reasonable time [195-201], there was only one experimental report in 1976 of the electrochemical generation of a short-lived Hg(III) intermediate [202], but this was regarded as inconclusive as the reported ESR spectrum is not that expected for a d^9 Hg(III) compound [200]. In 2007, HgF_4 was reported in a neon matrix from the reaction of Hg atoms and F_2 after photolysis, using a combination of IR experimental data and calculations to assign a band at 703 cm^{-1} to the E_u mode of HgF_4 [203]. A very weak band in argon matrices at 682 cm^{-1} was also assigned to HgF_4. During this time Young *et al*. had also been carrying out experiments using a combination of IR, UV-vis-NIR and Hg L_3-edge XAFS spectroscopy to investigate the formation of HgF_4 using both HgF_2 and Hg atoms in F_2/Ar matrices [204]. The IR and UV-vis-NIR data provided no evidence for the formation of HgF_4 in argon matrices and the Hg L_3-XAFS experiments were an important part of confirming this, and also provided the first experimental evidence for the Hg-F bond length in HgF_2.

The IR and UV-vis-NIR data had indicated that on deposition of Hg atoms into F_2/Ar matrices, a weak Hg...F_2 complex was formed, which was readily converted to HgF_2 on photolysis. The initial aim of the Hg L_3-edge XAFS experiments was to deposit Hg atoms

into a F_2/Ar matrix, characterise the Hg...F_2 complex, and then photolyse this complex *in-situ* to generate HgF_2, monitoring the product formation using the combined IR-EXAFS facility. The Hg L_3-edge XANES spectrum would also indicate the presence of Hg(IV) as this would have a white line feature similar to that in $[AuCl_4]^-$ (see Fig. 62(d)). The initial deposition of Hg atoms in 10%F_2/Ar was carried out in the dark, but it was obvious from the *in-situ* IR data that some $HgF_2$was being formed due to photolysis by radiation from either the IR source or the He-Ne laser in the FTIR spectrometer or the X-rays. Therefore, the rest of the deposition was carried out in the absence of either IR or XAFS monitoring. Fig. 62 (b) shows the Hg L-edge XANES spectrum in the early stages of deposition, with very little HgF_2 present in the IR spectra. The spectrum is fairly featureless, as it that for Hg atoms in argon (Fig. 62(a)). Fig. 63 shows the *in-situ* monitoring of the Hg lamp broad band photolysis once deposition was complete using both IR and Hg L_3-edge XANES. The peak at 644 cm^{-1} in the IR spectrum is the asymmetric ν_3 stretching mode of HgF_2, and the bands at 667 and 662 cm^{-1} are due to atmospheric and matrix isolated CO_2, respectively. It is clear from the initial IR spectrum that there is a small fraction of HgF_2 present at the end of the deposition (formed due to photolysis from the IR source, Hg-Ne laser and X-ray) and that the subsequent growth of this on photolysis correlates with the appearance of the edge structure in the Hg L_3-edge XANES spectra recorded at the same time. The Hg L_3-edge XANES spectrum after photolysis is shown more clearly in Fig. 62(c), and this is entirely consistent with the presence of a Hg(II) species [205, 206]. The spectrum obtained when Hg atoms were trapped in solid F_2 was essentially identical to this, confirming the formation of the same Hg(II) species in both 10%F_2/Ar and 100% F_2 matrices, and that there is no evidence of a significant white line characteristic of Hg(IV). XANES spectra

Whilst it was not possible to structurally characterise the initial Hg...F_2 complex due to its instability, the Hg L_3-edge EXAFS and FT of HgF_2 formed after photolysis are shown in Fig. 64. The first peak in the FT is due to a Hg-F distance of 1.94(2) Å and this represents the first experimental structural data for molecular HgF_2. This is in good agreement with the computational reports where it was found that the Hg-F bond shortens by *ca*. 0.10 Å from *ca*. 2.05 to *ca*. 1.95 Å when relativistic effects were included [196, 197, 201, 203, 207, 208]. The second feature in the FT has contributions from both multiple scattering within the linear HgF_2 unit as well as Hg...Ar interactions at 3.90(5) Å.

In addition to the work of Beattie and Young on EXAFS studies of matrix isolated inorganic compounds described above there have been a number of other reports as well.

9.9. **Diborane – B K-edge**

Diborane was investigated as a solid and in argon matrix and monitoring by mass spectrometry showed the characteristic pattern for diborane, with no evidence for larger boranes [209]. A liquid nitrogen cooled graphite target was used for neat B_2H_6, and a 15 K silver film for 5% B_2H_6/Ar. The B K-edge NEXAFS of the neat B_2H_6 were different from those of the matrix isolated B_2H_6/Ar spectrum as shown in Fig. 65.

The matrix spectrum was similar to the previously reported electron energy loss spectrum [210, 211]. The peak at 192.5 eV (1') was interpreted as a transition from the B 1s to π^* level and the peak 2.5 eV above it (2') as the B 1s to σ^* transition. The features above 195 eV were thought to be due to Rydberg states, shape resonances or multi-electron excitations. For the neat sample on graphite there was no significant variation in the spectrum when the data were collected at different angles of incidence of the HOPG substrate with respect to the incident radiation indicating little or no orientational ordering of the molecules. (HOPG can act as a template for epitaxial growth). Differences in matrix and the neat spectra were ascribed to differing intermolecular interactions when the diborane was condensed. The B K-edge spectrum of pure condensed diborane was remarkably similar to that of pentaborane. However, any association was reversible as diborane was evolved when the samples were heated to 100 – 110 K, indicating weak interactions rather than bond breaking or formation. The photoemission spectrum of solid diborane also had features characteristic of tetraborane and pentaborane indicating that on condensation the bonding in diborane changed.

9.10. **Application of cryogenic (matrix free) conditions**

The apparatus used for the matrix isolation studies by Beattie and Young was also used by Levason and Ogden to structurally characterise a wide selection of highly reactive and unstable species such as: CrO_2F_2, MnO_3F [212]; WF_6, ReF_6, OsF_6, IrF_6, PtF_6 [213]; MoF_6, RuF_6, RhF_6 [214]; and OsO_3F_2 [215], and structural characterisation of the bromine oxides used liquid nitrogen based apparatus [216, 217]. Other cryogen free experiments include KrF_2 [218, 219].

10. XAFS studies of matrix structures and guest-host interactions.

As indicated in section 3 diffraction experiments either of ideal matrix hosts [37-39] or those more representative of rapid vapour deposition [42-45, 47-52] can yield structural data about the matrix. This work has shown that cryogenic matrices originating from gas phase deposition are generally microcrystalline, porous solids, with crystallites of 400 – 500 Å (for Ar), which may also contain amorphous or nearly amorphous domains [44, 45, 47, 49, 52]. However, EXAFS is ideally suited to obtaining structural information from the perspective of **both** the host and the guest, especially as it does not require any long range order.

10.1. Pure rare gas matrices

10.1.1. Solid Neon

A number of workers have used X-ray absorption spectroscopy to study solid neon, with the emphasis on understanding the one and two electron processes occurring in the NEXAFS/XANES region [220-226], rather than the structural information in the EXAFS part of the spectrum. Complementary resonant X-ray absorption experiments of neon clusters with 15-4000 atoms in molecular beams have been carried out [227, 228] as have calculations using improved coupled cluster techniques [229].

10.1.2. Solid Argon

The Ar K-edge EXAFS analysis of solid Ar was first reported in 1984 [230] giving a nearest neighbour distance of 3.76(1) Å, in excellent agreement with known value of 3.755(4) Å. Subsequent work gave an Ar-Ar first shell distance of 3.75 Å [158]. During later investigations of OCS in Ar matrices, Ar K-edge data on pure Ar was obtained (Fig. 66) which revealed an Ar...Ar first coordination shell distance of 3.75(1) Å [231], in very good agreement with the earlier data [158, 230, 232]. Although the FT of the EXAFS data clearly showed the presence of four shells characteristic of an argon fcc lattice only the first shell was modelled via the use of Fourier filtering [231].

There have been a series of complementary gas phase cluster experiments at both the Ar K-edge [232-234] and L-edges [233, 235-237].

10.1.3. **Solid Krypton**

Of the rare gases, krypton has elicited the most study as its K absorption edge at 14326 eV is readily accessible.

The Kr K-edge XANES spectrum of solid Kr at 4.2 K was dominated by continuum state transitions whereas in solid KrF_2 at 77 K there were also very strong bound state absorptions at lower energy than the continuum state transitions [218]. The XANES spectra of gaseous Kr were dominated by 4s – np atomic transitions [238, 239], whilst the EXAFS region that would be expected to be featureless displayed a number of multi-electron excitations [240], which are present in most spectra, but usually go unobserved, although they can have a pernicious effect on the quality of the background subtraction.

The nearest neighbour Kr-Kr distance in solid krypton derived from Kr K-edge EXAFS experiments in 1983 was reported as 4.03 Å (using the tabulated phase shift correction of 0.34 Å.) [241], compared to the known distance of 4.00 Å [40]. Solid Kr at 10 K and gas phase Kr were studied as part of an investigation of Kr on graphite, and this used the known Kr-Kr distance of 3.99 Å to parameterise the Kr-Kr backscattering phase and amplitude to give Kr-C values of *ca*. 3.7 Å [242]. A subsequent report of solid Kr at 10 K gave a Kr-Kr distance of 3.98 Å [81] in good agreement with the X-ray data of 3.99 Å. When the matrix was annealed to 30 K and recooled to 10 K, there was no significant difference in the EXAFS spectrum, but at 30 K the amplitude of the oscillations was reduced by about 50%. The presence of at least three more distant shells was consistent with Kr in a fcc lattice. A more recent study investigating liquid krypton under pressure reported the spectra of gaseous Kr at RT, liquid Kr at 118 K and solid Kr at 30 K [243], but as the emphasis was on removing the second excitation features from the liquid and solid spectra [240], no interatomic distances were reported.

An X-ray [244] and EXAFS [245] study of solid krypton up to 20 GPa was extended to lower and higher pressure and with an extended energy range [246], however, the pressures obtainable were below those predicted for the fcc to hcp and metallic transitions. The variation of the first Kr-Kr shell in solid krypton under pressure at room temperature is shown in Fig. 67 [246] and is in good agreement with both the X-ray data and calculations. Double excitation channels from the gas phase spectra [239, 247] were used to improve the quality of the background subtraction for the liquid and solid spectra.

The thermal expansion and anharmonicity of solid Kr over the temperature range 24 -43 K was studied by Kr K-edge EXAFS, using the 1st, 3rd and 4th shells. The 3rd and 4th shells were able to be fitted using a using Gaussian distance distribution, but the 1st shell required a cumulant expansion [248].

The Kr L-edge spectra (1660-1760 eV) for gas phase, cluster and solid Kr have been published [249].

10.1.4. **Solid Xenon**

In solid xenon the nearest neighbour distance derived from the Xe L_3-edge EXAFS data was 4.355(10) Å [230], slightly longer than the diffraction data of 4.335 Å reported by Horton [39]. The gas phase spectra at the Xe K-edge [250-253] and Xe L-edges [254-258] are well studied because of the interest in the multi-electron excitations.

10.2. **Mixed rare gas systems**

10.2.1. **Kr, Xe and Ar in Neon matrices**

Kr, Xe and Ar atoms in Ne matrices behaved very differently compared to Kr or Xe atoms in Ar matrices [230]. The example of Kr/Ne was discussed in some detail which indicated the formation of Kr clusters in Ne matrices due to the presence of Kr-Kr features at 3.915(30) Å in addition to those at 3.485(30) Å due to Kr-Ne. The Kr-Kr value (3.915 Å) was slightly smaller than that observed in solid Kr (3.97 Å), and it was noted that this contraction behaviour was also observed for the Ar/Ne and Xe/Ne systems. For 1% Kr/Ne the coordination number for the Kr-Kr shell was 2 indicating the formation of a trimer. For the 3% and 10 % samples it was 9, implying the formation of small clusters of Kr in the Ne matrix. SR XPS was used to identify that binary argon-neon clusters adopt a core-shell structure with the argon in the core and the neon in the shell [259].

10.2.2. **Kr in Argon matrices and Kr in Nitrogen matrices**

For 1% Kr/Ar matrices a Kr-Ar nearest neighbour distance of 3.81 Å was observed together with a 2nd shell at 5.53 Å and a 3rd shell at 6.69 Å [241]. The *nn* distance is longer than that observed for solid Ar of 3.76 Å [230], but shorter than that for solid Kr of 4.03 Å [241] .This behaviour was observed for Kr/Ar matrices with up to 10% Kr, indicating the Kr atoms take

up substitutional sites in the Ar lattice. For Kr/N_2 matrices the presence of features in the FT close to those expected for Kr-Kr interactions implied the formation of Kr clusters in solid N_2 [241].

A subsequent Kr K-edge study of a 0.7% Kr/Ar matrix gave a Kr-Ar distance of 3.78 Å [81], closer to that expected for Ar-Ar distances (3.76 Å) [230] and less than the Kr-Kr distance of 3.98 Å [81]. The remaining Kr-Ar distances were also very similar to those expected for Ar-Ar indicating that the Kr occupies a subsitutional site in the Ar fcc lattice and only appears to only have a minimal affect on the Ar fcc lattice [81].

10.2.3. **Xe in Argon matrices**

The Xe-Ar nearest neighbour distance of 3.99(2) Å was found to be independent of concentration between 1 and 10% of xenon in argon [230]. This was noted to be smaller than some previous calculated values, but larger than others. For Xe concentrations < 3% a coordination number of 12 (+3, -1) was calculated, with the Debye-Waller factor the same as for solid Ar. The authors concluded that the Xe atoms showed a statistical distribution and took up substitutional sites in Ar matrices, which was similar to the case of Kr in Ar [241].

10.2.4. **Noble gas atoms in unconventional matrices**

EXAFS studies have also been used to study rare gas atoms and clusters in unconventional matrices such as: Ar atoms implanted in amorphous carbon films [260] or Si, SiO_2 or HOPG [261]; Ar and Kr atoms in highly stressed amorphous carbon films [260]; over-pressurised Kr bubbles in copper and nickel [262]; Xe bubbles in single crystal silicon. [263]; Kr clusters in Be and Si [264]; Xe bubbles in UO_2 [265, 266] and amorphous carbon [267]. A combination of XAFS and XRD was used to identify xenon clathrates as having structure type I, and Kr clathrates as structure type II, and that when Xe was added to Kr clathrates the structure transformed from type II to type I [268].

10.3. **OCS, HCl and SiH_4 as a probe of host-guest interactions**

Roubin *et al*. studied OCS trapped in argon matrices at a dilution of 1:100 and deposited on an aluminium foil at *ca*. 25 K [269]. Whilst peaks A and B in the FT of the S K-edge EXAFS data (Fig. 68(c)) were assigned to the S-C and S-O distances, respectively, the analysis concentrated on the S...Ar interactions (peak C in Fig. 68(c)) as the purpose of the paper was to investigate the use of EXAFS in unravelling the complexities of the host-guest

interactions. The calculations of Winn and Lang [270, 271] which had indicated that the OCS molecule would be trapped in a two-hole trapping site and these were used to predict the S-Ar distances for OCS in an argon matrix at 1:100 dilution. However, the best fit to the data was for a single S-Ar shell with 11 argon atoms at 3.78 Å, compared to the calculated values of one argon atom at 3.59 Å, four argon atoms at 3.68 Å. 2 at 3.76 Å and 4 and 3.84 Å, giving a total of 11 nearest neighbours. The Debye-Waller factor had to be increased, reflecting the presence of static disorder. Although there are likely to be dimers, trimers and other multimers present in matrices as concentrated as these, which will yield a variety of S...C, S...O, S...S and S...Ar distances, these were not modelled as it was anticipated that the resultant EXAFS oscillations would not add coherently, so would not be detected in the EXAFS spectrum. The value of 3.78 Å for the S...Ar distance is slightly larger than that for solid Ar (3.76 Å) indicating the presence of a trapped molecule results in a slight expansion of the argon cage. It should be noted that Winn's experiments [270, 271] were carried out with near homeopathic dilutions of 1:50000 compared to the 1:100 used in the EXAFS experiments, and that broadening and multiplets involving shifts of a few wavenumbers are present for concentrations greater than 1:1200, and that this was used to explain the less organized structure than that predicted from the experiments and calculations of Winn [270, 271]. This kind of phenomenon has also been observed for SF_6 where very high dilution was required to obtain IR spectra consistent with single trapping sites [272].

This work was built upon in a subsequent investigation using not only OCS, but also SiH_4 and HCl in noble gas, nitrogen and methane matrices [231]. In addition, Ar K-edge data on pure Ar was obtained which revealed an Ar...Ar first coordination shell distance of 3.75(1) Å, in very good agreement with the earlier data [158, 230, 232]. Although the FT of the EXAFS data clearly shows the presence of four shells (Fig. 66) characteristic of an argon fcc lattice only the first shell was modelled via the use of Fourier filtering [231].

The earlier work on OCS in argon matrices was subsequently extended to include Xe, N_2 and CH_4 matrices and the S K-edge XANES spectra are shown in Fig. 69. As in the previous work, the analysis only utilised Fourier filtering of the S...Ar shell, rather than including the intramolecular distances as well. However, they concluded that by comparison with a spectrum of pure OCS the oscillations in the higher energy part of the spectrum (100 – 350 eV beyond the edge) were dominated by contributions from the S-C and S-O intramolecular distances. In contrast the low energy part (<100 eV) contained features characteristic of

scattering involving the matrix atoms, and hence different spectra were observed for Ar, Xe, N_2 and CH_4 matrices (Fig. 69). In general the Debye-Waller factor for the shells involving the matrix atoms were much larger, so the oscillations were more heavily damped, especially at high *k*. In addition, the backscattering amplitude is dependent on the atomic potential of the matrix atoms, which is minimal for H, small for C and N, larger for Ar and Xe. For these reasons the spectrum of OCS in CH_4 matrices was fairly similar to that of pure OCS. The spectra of OCS in argon and xenon matrices were similar to each other in this low energy region, with clearly identifiable oscillations, which were absent from the spectra of OCS in N_2 or CH_4 matrices. But the sulfur-rare gas contributions were more dominant for argon than xenon, due to the problems of absorption by the xenon of both the incident and fluorescence photons used for detection (see Fig. 26). Therefore, only detailed analysis of the OCS-Ar system was reported which was a repeat of that in [269], but there has been a subsequent computational paper [273].

In addition to the investigation of OCS guest:matrix interactions, those involving HCl and SiH_4 were also studied [231]. The Cl K-edge spectrum (Fig. 70) of HCl/Ar was very similar to that of pure argon, except for the presence of a molecular antibonding π^* state before the main edge peak, which was assigned to a $1s \rightarrow 4p$ Rydberg transition. There was no significant difference between the Cl K-edge EXAFS of HCl/Ar and the Ar K-edge EXAFS of pure argon indicating that the argon lattice readily accepts an HCl molecule in a substitutional site. It was noted that HCl in argon is well known to undergo almost free rotation in argon [274-277], which no doubt contributed to the observation of a single Cl...Ar distance of 3.75 Å. Whilst there was evidence for the presence of more distant shells, there was no attempt to fit them. There appeared to be no discussion concerning the presence of small oligomers of HCl [278-280] where the Cl...Cl distances may be of a similar magnitude to the Cl...Ar distances.

Silane, which is a sphere of radius of *ca*. 5 Å, cannot be accommodated within a one or two atom hole in the argon lattice [231]. Whilst a four atom vacancy was considered, the theoretical spectrum for this and the one hole model were not consistent with the experimental data and the authors were not able to draw a conclusion regarding the validity of either model. This may be a result of the fact that the IR spectrum of SiH_4/Ar reveals two distinct trapping sites [281].

The authors concluded at the end of this work "that probing the matrix environment of a dilute sample with the EXAFS technique in the soft X-ray region is not a simple task because of the poor signal to noise ratio and the problem of absorption by the matrix itself." but that "even if a quantitative analysis is not always possible, it can provide valuable information about the ordering around the molecule" [231].

10.4. CH_2Br_2 in argon matrices

As part of a demonstration experiment showing how IR and EXAFS data could be collected from the same sample, Young and Spicer [102] identified a Br...Ar distance of 3.75 Å for a 0.67% CH_2Br_2/Ar matrix, consistent with the sum of the van der Waals radii.

10.5. Hg atoms in argon matrices

The Hg L_3-edge EXAFS data from Hg atoms trapped in solid argon (Fig. 71) was studied as part of the investigation into the possible formation of HgF_4 (see section 9.8). The EXAFS gave an intense Hg–Ar shell in the FT at 3.86(4) Å with a coordination number of approximately 9 [204]. The weaker features in the FT could also be modelled reasonably satisfactorily for an argon fcc lattice (5.31, 6.54, 7.71 Å) thus indicating that the Hg is located in a substitutional site in the argon matrix. The lack of Hg-Hg interactions at around 3 Å, confirmed that the evaporation of Hg at 298 K resulted in a high monomer fraction. The Hg...Ar distances for all of the shells are slightly longer than those expected for a perfect Ar fcc lattice, e.g. the value of 3.86(4) Å for the first Hg–Ar shell is slightly larger than that for solid Ar (3.756 Å) [38] indicating some distortion of the argon lattice by Hg. For HgF_2 formed in an argon matrix by photolysis of Hg atoms in the presence of F_2, the first shell (Fig. 64) was due to the intra-molecular Hg-F distances, but there was evidence for a Hg...Ar shell at 3.90(5) Å, but due to multiple scattering within the HgF_2 unit at similar distances it is hard to pinpoint the coordination number, but is probably between 3 and 4. The inference is that there are four argon atoms around the Hg waist of the linear HgF_2 molecule.

10.6. Summary of host-guest interactions

Table 2 gives a summary of all the host-guest interactions described in this section as well as elsewhere in the review.

11. Application of other Synchrotron Radiation techniques to matrix isolated species.

Although the bulk of this review has been concerned with the application of X-ray absorption spectroscopy to matrix isolated species, synchrotron radiation sources are also intense sources of radiation from the hard X-ray to far-IR, and these other regions have been utilised to characterise and study matrix isolated species. A review of high resolution spectroscopy utilising vacuum-UV radiation which included some SR studies of matrix isolated species was published in 1995 [282], a review of luminescence spectroscopy with SR was published in 2006 [283], together with reviews on electronic excitations [284] and molecular photodynamics in rare gases solids [285]. A review of the use of SR vac-UV to study gas phase clusters was published in 1999 [286].

11.1. SR vacuum ultraviolet studies of matrix isolated species

Whilst intense line sources (both laser and gas discharge) are available for laboratory based vac-UV experiments, SR vac-UV provide a tuneable source of radiation, which is especially useful for selective excitation experiments. Examples include the study of matrix isolated: Ag [287]; Cu [288]; Xe [289]; Cl [290]; Hg [291]; Cd [292]; Zn, Cd, Hg [293]; Mg atoms [294]; the reaction products of Al with N_2O in Kr matrix using 2-8 eV SR radiation [295]; as well as alkali noble gas excimers [296, 297]. The thermally stimulated luminescence and conductivity of doped Ar solids has also made use of SR vac-UV radiation [298].

The tunability of the SR source also allows for the study of photodissociation and photoionisation such as: H_2O in Xe matrices [299]; Cl_2 in Ar, Kr and Xe matrices [300, 301]; Cl_2 in Ar matrices [302]; Me_2Zn in argon matrices [303]; CH_4 in Kr matrices [304]; CH_3OH in solid Ar and Ne [305]; as well as the photochemistry of HCl in rare gas matrices [306-308]. SR vac-UV radiation has been used to identify the photoionisation threshold of CS_2 [309] and C_6F_6 [310] in solid Ne, and the valence photoionisation of $CH_3C(O)SCH_3$ [311].

The study of a variety of physical processes in (doped) solid rare gases has utilised vac-UV SR radiation including: N_2 in Ne [312]; NO in N_2 and N_2/Kr matrices using both tuneable SR and ArF laser excitation [313]; luminescence of ArXeH, ArKrD in Ar and KrXeD in Kr [314]; ArF and KrF exciplexes studied over the range 50 to 600 nm [315]; F_2 in Ne [316]; NgCl, Ng_2Cl NgNeCl (Ng = Ar, Kr, Xe) excimers formed in Cl_2 [317]; resonant 2 photon

photoemission from solid Kr [318]; soft X-ray emission spectra of solid Kr (4p-3d) and Xe (5p-4d) [319]. Zimmerer *et al.* have made extensive use of luminescence spectroscopy with vac-UV SR [283] including: a detailed study of the 3rd molecular continuum in Kr [320]; desorption of selectively excited Kr atoms from a solid surface of Ar [321]; charge centres in solid Ar [322]; photon yield from solid Kr and Xe at the edge of the exciton absorption [323]; exciton trapping diatomic and triatomic molecular complexes in xenon cryocrystals [324]; luminescence spectra of Kr atoms in Ar excited with selective SR excitation [325]; excimer desorption from solid Ar under selective excitation by photons in the 10-35 eV range [326]; excitonic mechanisms of selective inelastic radiation induced processes in solid Ar [327]; permanent lattice defects via exciton self trapping in Xe [328], lattice deformation in Ne [329]; inelastic photoelectron scattering in CO doped Ar by SR [330] and thermoluminescence of CO doped Ar [331].

The vac-UV absorption spectra of: CO in solid Ar [332], MeOH in argon [333], and small molecules (O_2, NO, CO_2, N_2O, H_2O and NH_3) as solids and solid NH_3/Ar mixtures [334] have also been reported.

SR Vac-UV MCD and absorption spectra of matrix isolated organic compounds includes: zinc phthalocyanine in argon matrices and benzene in argon matrices [335-337]; phthalonitrile in argon [338]; and zinc tetrabenzoporphyrin in argon [339]; as well as P_4 in argon matrices [340].

SR vacuum-UV radiation has also found application in the study of systems prototypical of the inter-stellar medium (ISM) as a photolysis source. The photolysis of CH_4 in solid Ne with vac-UV from SR led to bands assigned to C_5H radicals [341], photolysis of solid H_2 containing NO resulted in *trans*-HNOH [342], carbamic acid (NH_2COOH) was formed in neutral form when ice mixtures containing H_2O, CO_2, NH_3 were irradiated by 4 – 20 eV photons [343], amino acid formation was observed following 4 – 20 eV irradiation of H_2O, CO_2, NH_3 ice at 16 K [344]. Photolysis of C_2H_2 in solid Ar with 107 – 220 nm SR was used as a potential simulation of Titan's atmosphere [345]. Irradiation of H_3CF in solid Ne with 124 nm SR light resulted in a broad spectrum of products [346]. Polarized vac-UV fluorescence of anthracene and pyrene in Ar up 75000 cm^{-1} [347] as well as CO...anthracene and O_2...anthracene complexes [348] are of relevance to the identification of the unidentified IR (UIR) bands. The absorption spectra of the C_3 molecule in solid neon or argon from 1100

to 5600 Å using SR [349] may help identify the carriers of the diffuse interstellar bands (DIBs).

11.2. **Far-infrared studies**

Synchrotron radiation also extends to the far-IR (THz) region, but there are very few studies published, probably because there is little to gain for the matrix experiment in the UV, visible and IR region compared to conventional laboratory sources, unless the SR time structure is required for dynamics or time-resolved luminescence experiments, or the high brilliance is required for micro-focus experiments. However, it does allow access to the FIR region which is often unavailable in laboratories.

As part of the investigation into the effect of the matrix on the structure of $NiBr_2$ (see section 9.5) SR-FIR spectra [350] were obtained for $NiBr_2$ in Ar, CH_4 and N_2 matrices (Fig. 72) to try to locate the low energy bending modes, which had been previously reported at 68 cm^{-1} for $NiBr_2$ in argon matrices [351]. The SR-FIR experiments utilised heavy deposits as calculations had indicated that the intensity of the ν_2 bending mode would be low. Unfortunately, it is clear from the SR-FIR argon spectrum (Fig. 72(a)) that the low energy part of the spectrum (< 100 cm^{-1}), where the bending modes are expected, is dominated by the Ar phonon bands (32.4 and 70.8 cm^{-1}), nearly freely rotating water molecules (< 40 cm^{-1}) and argon hydrates between 40 and 100 cm^{-1} [352, 353]. Whilst the intensity of the water bands could be reduced by prolonged pumping and baking, this was not feasible in the limited amount of SR-FIR time available, and water bands are essentially impossible to remove completely from matrix spectra. In nitrogen matrices (Fig. 72(c)) the spectrum was also badly affected by the lattice and phonon modes of the nitrogen matrix [352, 353] which are usually obscured when CsI optics are used down to 200 cm^{-1}. However, in the spectrum of $NiBr_2$ isolated in solid CH_4 (Fig. 72(b)) there is a band at 55 cm^{-1} which is in reasonable agreement with the earlier Ar matrix value of 68 cm^{-1} [351]. These FIR spectra down to 20 cm^{-1} probably represent some of the lowest energy spectra ever recorded at the Daresbury Synchrotron Radiation Source.

12. **Conclusions and Future Directions**

The discussion above indicates how synchrotron radiation, and X-ray absorption spectroscopy in particular, have been used to provide unique structural insights concerning

both the matrix isolated species, and its interaction with the host. XAFS is one of only a couple of techniques capable of providing direct structural information from matrix isolated species, and is arguably the most powerful. The largest limitation is probably a combination of the need to use large national or international facilities, and that matrices with a large number of different trapped species will give rise to averaged data. The experiments carried out at energies where the matrix vacuum chamber can be kept isolated from the machine vacuum are reasonably mature, but there is scope for further development of *in-situ* monitoring of photolysis and annealing using UV-vis, or even Raman spectroscopy. The soft X-ray energies above about a 1000 eV have also been exploited, it is at lower energies where more radical developments might be expected.

12.1. **3d L-edge XAFS**

As indicated in section 4.3.1, there is plenty of scope for the development of first row transition metal L-edge spectroscopy for matrix isolated species as the intense 2p-3d transitions would give a much greater insight into the electronic structure than that which is available experimentally at either the K-edges (1s-3d) or from conventional d-d spectroscopy where the transitions are forbidden (or weak) due to the selection rules. There have also been significant recent advances in the theoretical treatment of these transitions which will aid spectroscopic interpretation [70, 71].

12.2. **X-ray Raman scattering**

The K-edges of the important ligand elements such as C, N, O, F fall within the soft X-ray region (200 – 750 eV) and these can present considerable challenges to the experiment design in terms of sample penetration depth, sensitivity and having to be compatible with the UHV conditions of the beamline and source. One alluring option is to use non-resonant inelastic X-ray scattering (NRIXS) where excitations of core level electrons can be probed. This is usually known as X-ray Raman scattering where it is possible to obtain the EXAFS data from the light elements using much higher energy photons, where the energy required to excite a core electron is provided by an inelastically scattered X-ray photon [354-356]. Fig. 73 shows the processes occurring in X-ray Raman spectroscopy where an X-ray photon with incident energy, E_0, is inelastically scattered and provides a fraction of its energy, ΔE, to excite a core electron into an empty bound or continuum state leaving it with final energy, E_f [354]. As this is a scattering technique a large acceptance high-resolution analyser is required to collect the XRS X-ray Raman scattering data [354, 357, 358]. The inherent weakness of the X-ray Raman scattering process, compared to either Rayleigh (elastic) or Compton and scattering

from graphite is shown in the bottom of Fig. 73 [354]. Therefore, X-Ray Raman scattering provides a means for obtaining the information content of soft X-ray spectra while maintaining the experimental benefits of hard X-ray techniques. This gives considerable freedom to select the incident photon energy compatible with the experimental requirements. Due to the low cross section for the inelastic process, X-ray Raman spectroscopy has only been achievable relatively recently using high intensity, 3rd generation sources, coupled with improvements in X-ray optics. There has been significant work on water [359], and the field was reviewed in 2002 [354, 355]. More recent work has included: N_2, N_2O, CO_2 [360]; further work on H_2O [361-370]; hydrocarbons and asphaltenes [356, 371, 372]; C_{60} [373]; acetonitrile solutions [374]; ethylene and benzene [375]; B K-edge of MgB_2 [376]; B K-edge and Li K-edge in $LiBH_4$ [377]; Be K-edge [378]; polyfluorene [379]; silicates using O K-edge and Si L-edge [367, 380]; borate glasses using the B K-edge and Li K-edge [381, 382]; Si L-edge and Ba N-edge in Ba_8Si_{46} [383]; as well as theoretical developments [384, 385].

State of the art spectra obtained from neat materials are shown in Fig. 74 and these data clearly show the quality data that can achieved [357]. As the spectrometer has a fixed analysing energy (using the Si(440) or Si(660) reflections) the beamline monochromator (Si(311)) is scanned in order to acquire the energy transfer measurements, hence why the spectra have x axes labelled incident photon energy. The data for HOPG at different angles of incidence shows that when the *c*-axis of the HOPG is perpendicular to the spectrometer's momentum transfer vector (**q**) a maximum π^* (285 eV) to σ^* (292 eV) intensity ratio is observed (red line), but the σ^* transition becomes dominant when the *c*-axis approaches the **q** orientation (pale blue line) (Fig. 74(a)). Each C K-edge spectrum took 5 min. to acquire. The high quality oxygen 1s XRS spectrum (Fig. 74(b)) was obtained in less than 10 min. The Fe L-edge XRS spectrum of a $LiFePO_4$ charged battery cathode material in Fig. 74(d) used the Si(660) reflection due to strong-photo-absorption of the incident beam from the Fe 1s absorption when the Si(440) reflection was used.

Whilst the above spectra demonstrate the quality that can be achieved with concentrated samples, there is still a significant challenge in obtaining data from more dilute systems, as shown for oxygen XRS K-edge data for aqueous MeCN solutions in Fig. 75 [374]. The pure water spectrum is comparable to that above, but the quality reduces quite noticeably as the fraction of MeCN increases. Therefore, these spectra demonstrate what is currently achievable, and indicate that for realistic matrix dilutions X-ray Raman scattering may still be

a real challenge, but it does offer the tantalising possibility of obtaining structural information from the low Z elements such as C, N, O or F.

In addition there are reports of X-ray Raman scattering in the vicinity of the 3d L-edges which has been used to probe the electronic structure [386-392].

In addition to X-ray Raman scattering, other high resolution X-ray spectroscopic and inelastic scattering techniques employing similar experimental facilities to X-ray Raman such as X-ray emission (XES) (including X-ray K_β fluorescence which contains information about spin state and oxidation state [60, 393]) and resonant inelastic X-ray scattering (RIXS) [394-401] could in principle yield important and interesting data from matrix isolated species, but may suffer the same problems of sensitivity as X-ray Raman scattering.

It should be noted that 3rd generation SR sources equipped with nuclear spectroscopy beamlines can be used for Mössbauer experiments [402].

13. Acknowledgements

The research students and fellows from the Southampton, Manchester and Hull groups over the years who have contributed to the work reported here are gratefully thanked for all the late nights and early mornings collecting data at the synchrotron sources, as well as lugging a laboratory over the Pennines for each trip in the latter years. Prof. Ian Beattie, Dr Steve Ogden, Prof. Bill Levason and Prof. John Evans are thanked for their significant contribution to starting me on this journey, and their continuing support. None of the experiments carried out by the author would have been possible without the dedication of the station scientists (Bob Bilsborrow, Fred Mosselmans, Ian Harvey, Gert van Dorssen, Mark Surman) who have contributed enormously to the successes of these projects. The various funding councils (SERC, EPSRC, CCLRC, STFC) are thanked for providing beamtime and computational resources for the author's experiments.

Table 1. Refined EXAFS parameters for iron carbonyl halide complexes.

	r_{Fe-C} /Å	r_{Fe-O} /Å	r_{Fe-X} /Å	Ref
cis-$[Fe(CO)_4I_2]$	1.81	2.97	2.60	[81]
cis-$[Fe(CO)_4I_2]$	1.87	2.96	2.63	[170]
cis-$[Fe(CO)_4Br_2]$	1.85	2.96	2.43	[170]
$[Fe(CO)_5]$	1.80(2)	2.97(4)		[171]
$[Fe(CO)_5]$	1.81(2)	2.95(4)		[170]
$[Fe(CO)_5]$ (electron diffraction)	1.833(eq) 1.806(ax) 1.822 (mean) 1.827(eq) 1.807(ax)	2.970(9)(eq) 2.947(1)(ax)		[87] [88]
$[Fe(CO)_5]$ (X-ray diffraction)	1.801 1.804 1.811	2.937 2.921 2.939		[89]
	r_{M-C} /Å	r_{M-O} /Å	r_{M-Cl} /Å	Ref
trans-$[Fe(CO)_4Cl_2]$	1.85(3)	2.96(4)	2.25(3)	[171]
$[Fe(CO)_5]$	1.80(2)	2.97(4)		[171]
trans-$[Cr(CO)_4Cl_2]$	2.00(3)	3.11(5)	2.27(3)	[171]
$[Cr(CO)_6]$	1.89(3)	3.02(4)		[171]

Table 2. Host-guest distances determined by X-ray absorption spectroscopy

System	Interaction	Conditions	Distance	Reference
Ar	Ar...Ar		3.755(4)	[230]
			3.75	[158]
			3.75(1) Å	[231]
Kr	Kr...Kr		4.03	[241]
	Kr...Kr		3.97	[230]
	Kr...Kr		3.98 5.62 6.92 8.09	[81]
Xe	Xe...Xe		4.355(10)	[230]
Xe/Ar	Xe...Ar	3%Xe/Ar	3.99(2)	[230]
Kr/Ne	Kr...Ne	1-10%Kr/Ne	3.485(30)	[230]
Kr/Ar	Kr...Ar	1%Kr/Ar	3.81 5.53 6.69	[241]
	Kr...Ar	0.7%Kr/Ar	3.78 5.34 6.49 7.62	[81]
OCS/Ar	S...Ar	1% OCS/Ar	3.78	[231, 269]
HCl/Ar	HCl...Ar	1%HCl/Ar	3.75	[231]
CH_2Br_2/Ar	Br...Ar	0.67% CH_2Br_2/Ar	3.75(4)	[102]
HgF_2/Ar	Hg...Ar	Hg atoms + 10%F_2/Ar	3.903(5)	[204]
Hg/Ar	Hg...Ar	Hg atoms/Ar	3.86 5.31 6.54 7.71	[204]
$RbReO_4/N_2$	Rb...N_2		3.45 4.12	[103]
Fe-Ar		0.02% Fe/Ar	3.85	[116]
Fe-Ar	Fe-$Ar_{(interstitial)}$	0.1% Fe/Ar	2.82(8)	[117]
Fe-Ar	Fe-$Ar_{(subsitutional)}$	0.1% Fe/Ar	3.72(9)	[117]
Fe-Ne		0.4% Fe/Ne	2.47(2)	[118]
Fe-Ne		0.5% Fe/Ne	2.50(2)	[118]
Fe-Ne		1.5% Fe/Ne	2.41(5)	[118]

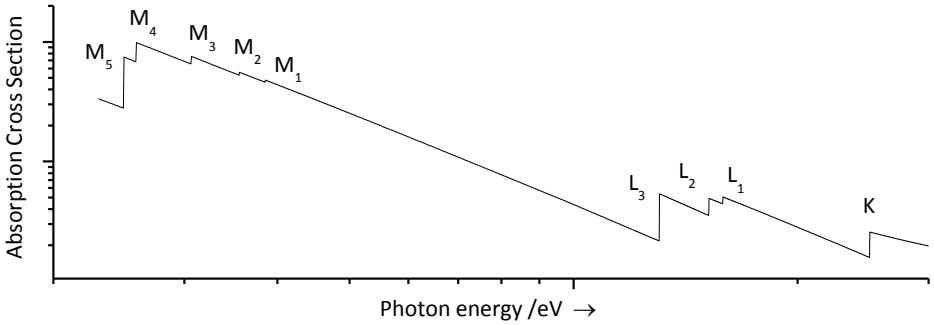

Figure 1. Schematic diagram of X-ray absorption edges.

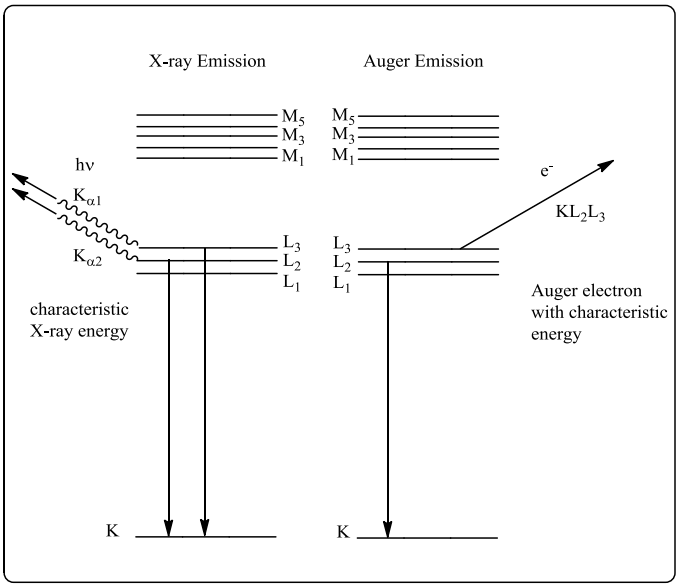

Figure 2. Schematic energy level diagram showing relaxation processes resulting in emission of characteristic X-rays or Auger electrons after creation of a 1s core-hole. (For clarity on the initial relaxation processes involving the L-shell are shown.)

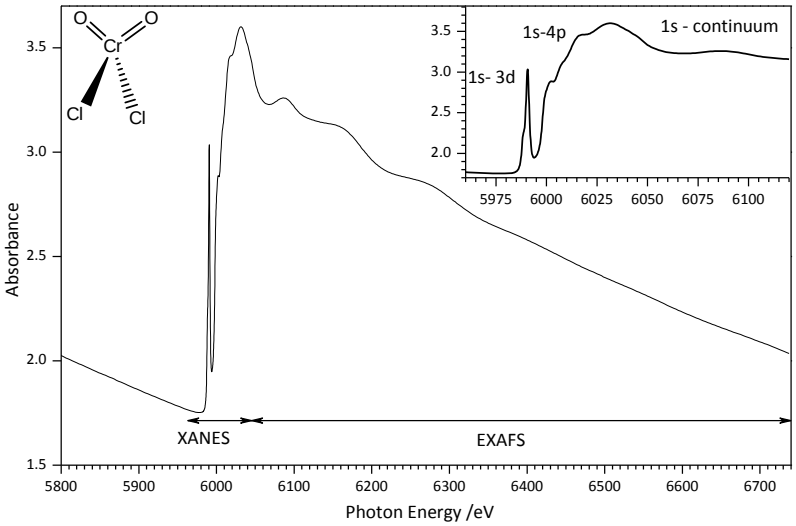

Figure 3. Cr K-edge XAFS spectrum of CrO_2Cl_2 at 10 K showing division of the XAFS spectrum into the XANES and EXAFS regions.

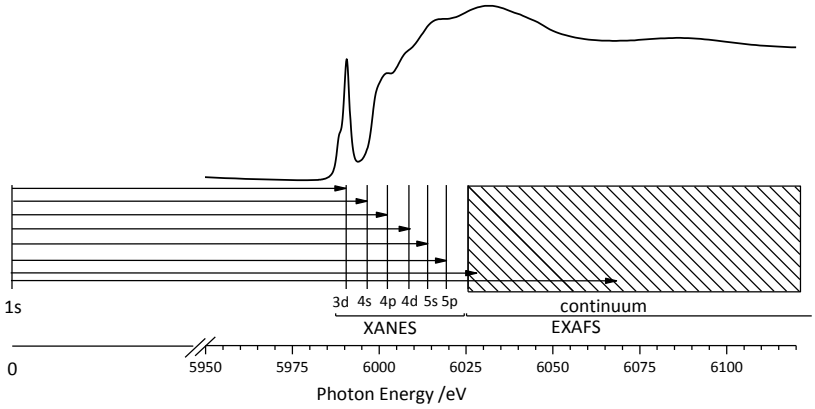

Figure 4. Schematic diagram of transitions occurring at the Cr K-edge in CrO_2Cl_2.

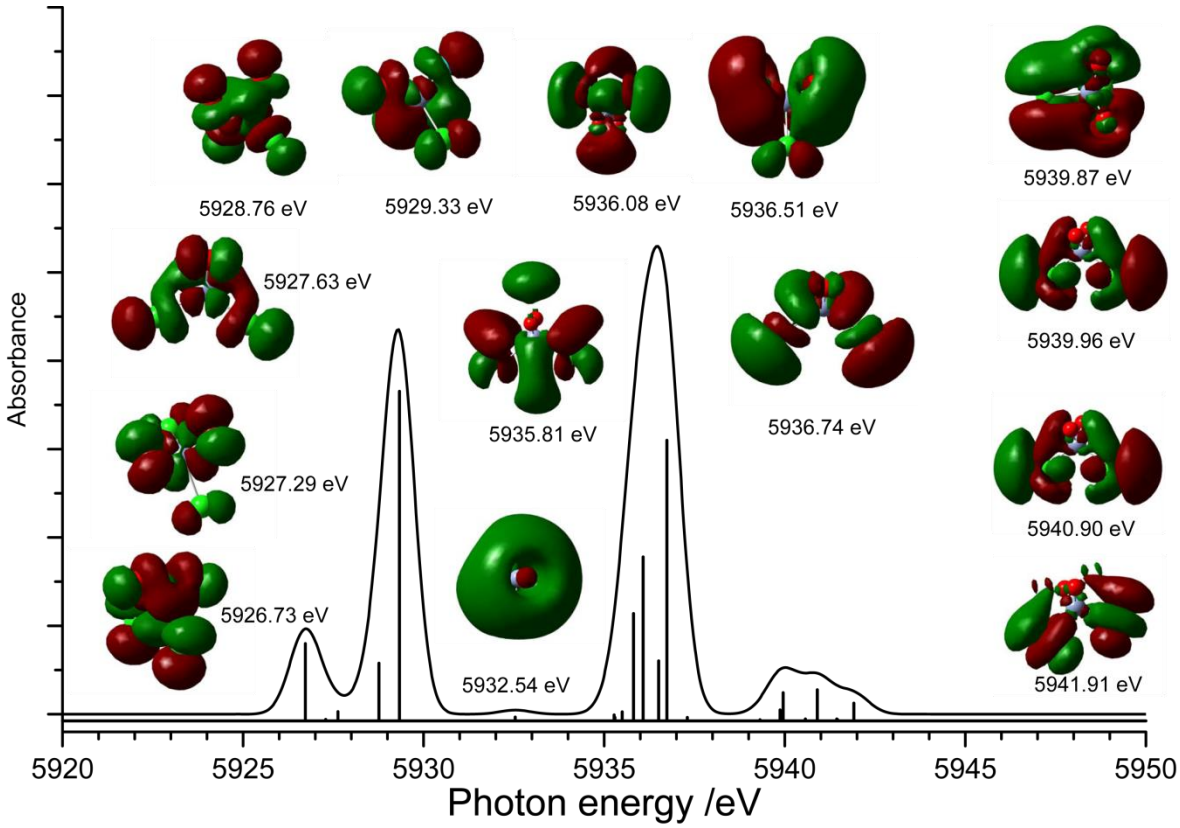

Figure 5. TD-DFT calculated XANES spectrum for CrO_2Cl_2.

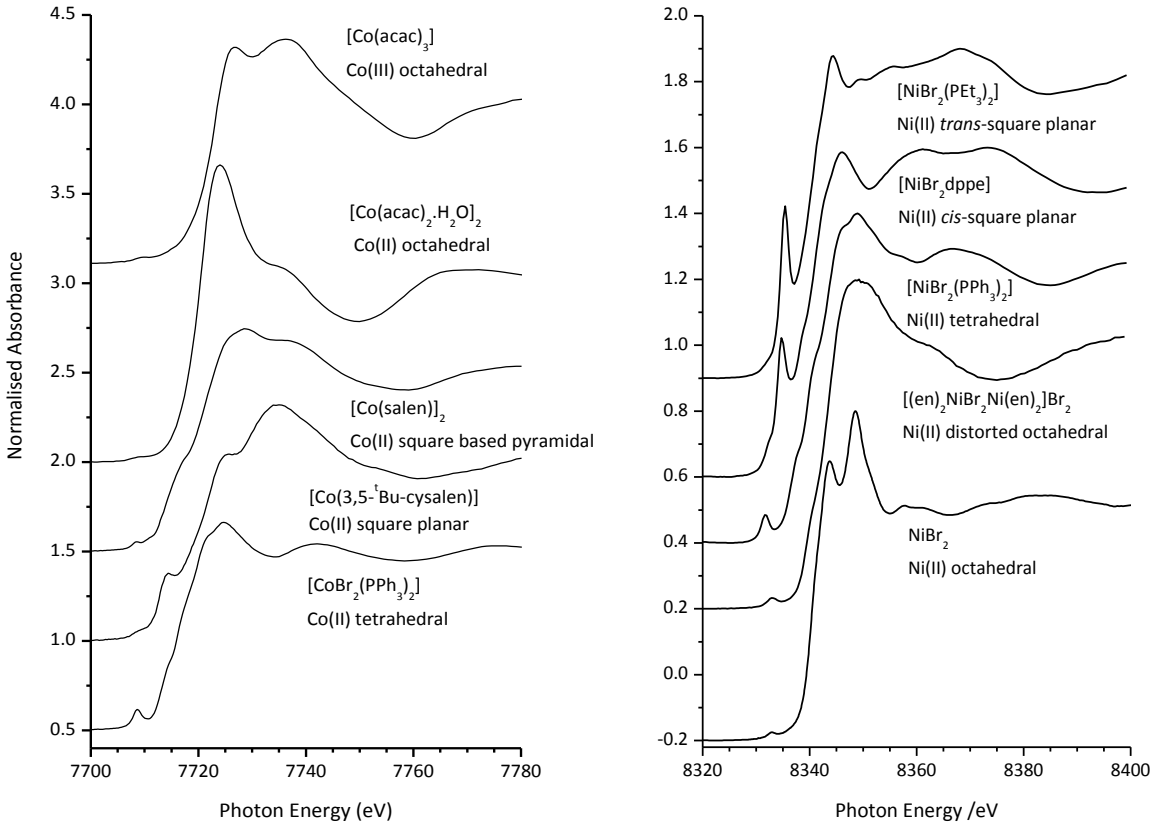

Figure 6. Representative Co K-edge XANES spectra (left) (data redrawn from A.D.J. Barnes, T. Baikie, V. Hardy, M.B. Lepetit, A. Maignan, N.A. Young, M.G. Francesconi, J. Mater. Chem., 16 (2006) 3489, [65]) and Ni K-edge XANES spectra (right).

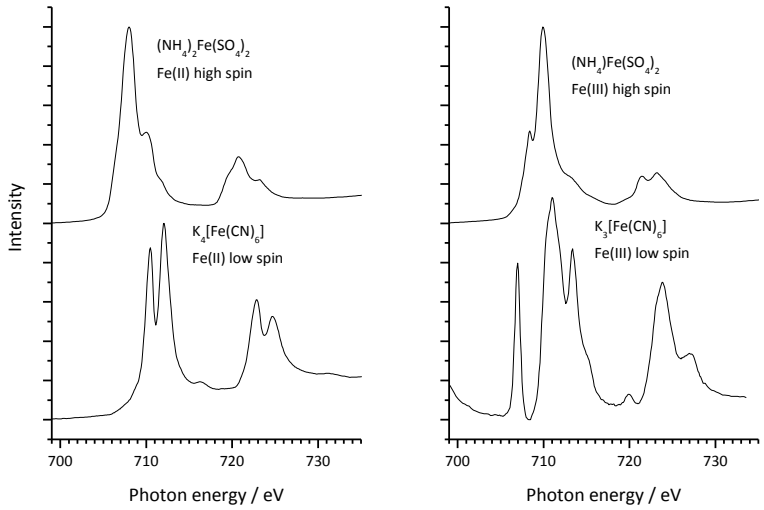

Figure 7. Representative Fe L-edge spectra of high- and low-spin Fe(II) and Fe(III) complexes (data redrawn from D. Collison, C.D. Garner, C.M. McGrath, J.F.W. Mosselmans, M.D. Roper, J.M.W. Seddon, E. Sinn, N.A. Young, J. Synchrotron Rad., 6 (1999) 585, [67]).

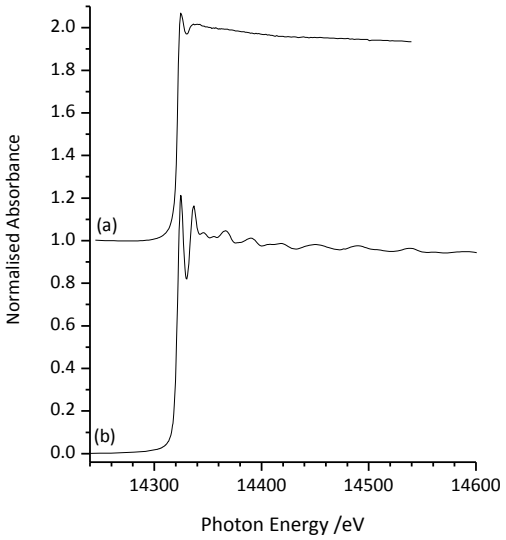

Figure 8. Kr K-edge spectra of (a) Kr liquid at 0.1 GPa and 298 K in a diamond anvil cell [82, 83] and (b) Kr solid at 10 K [81].

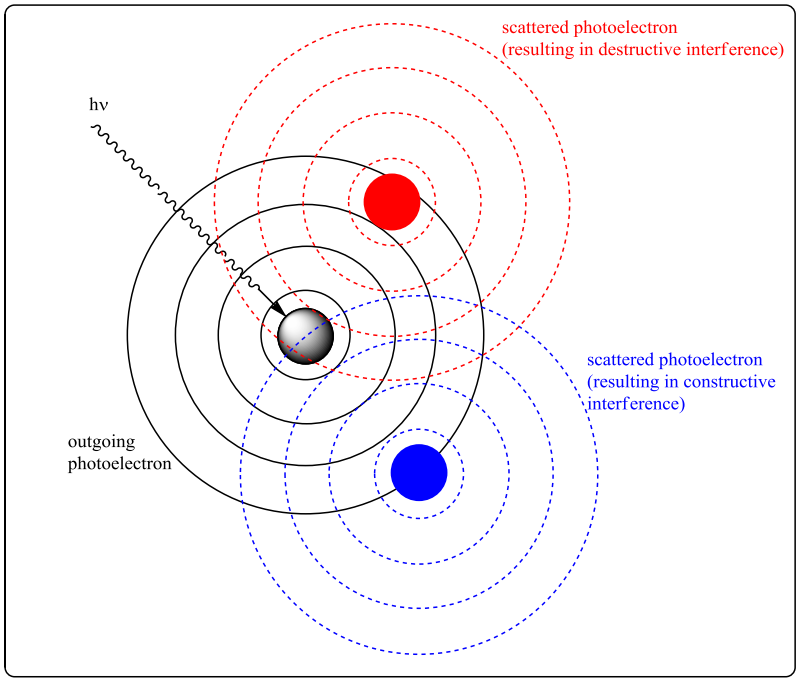

Figure 9. Schematic illustration of processes giving rise to oscillations in an EXAFS spectrum.

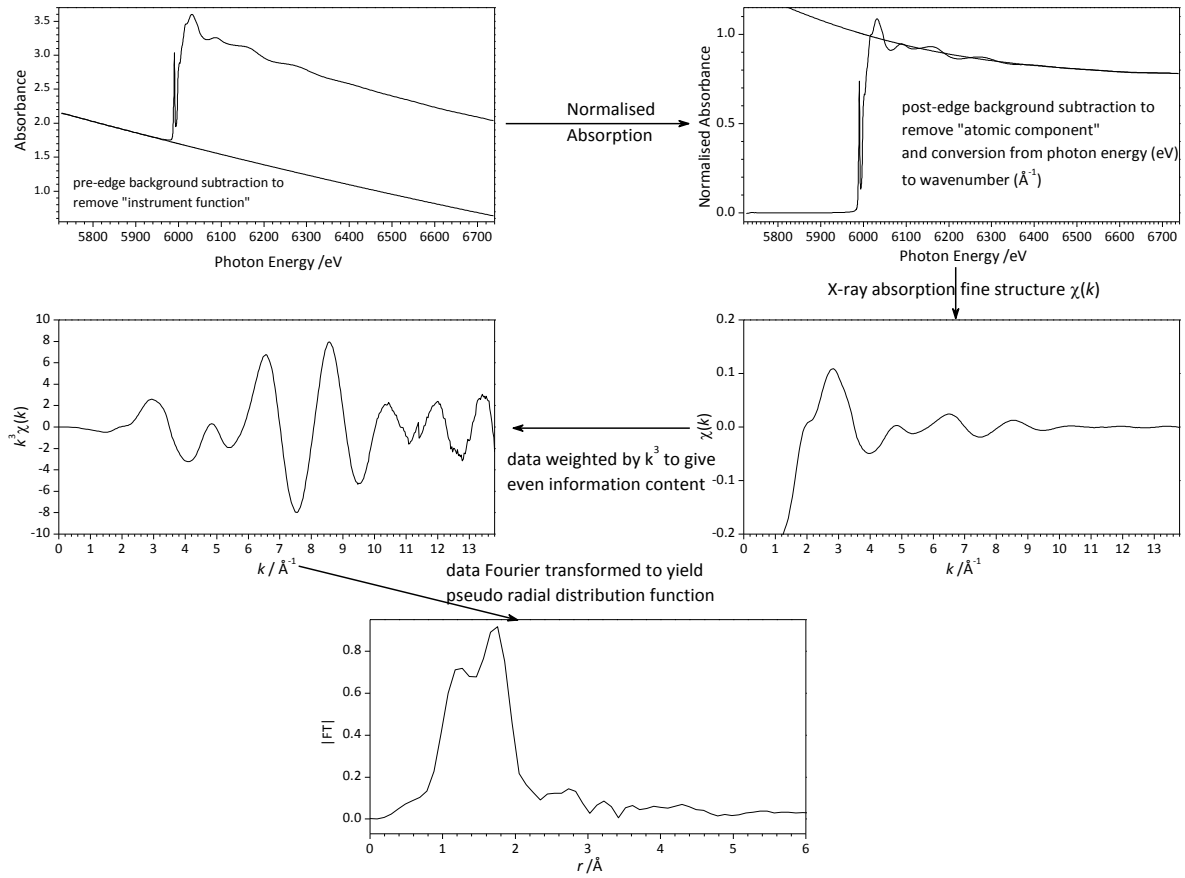

Figure 10. Background subtraction procedures used to extract EXAFS oscillations from raw data for CrO_2Cl_2.

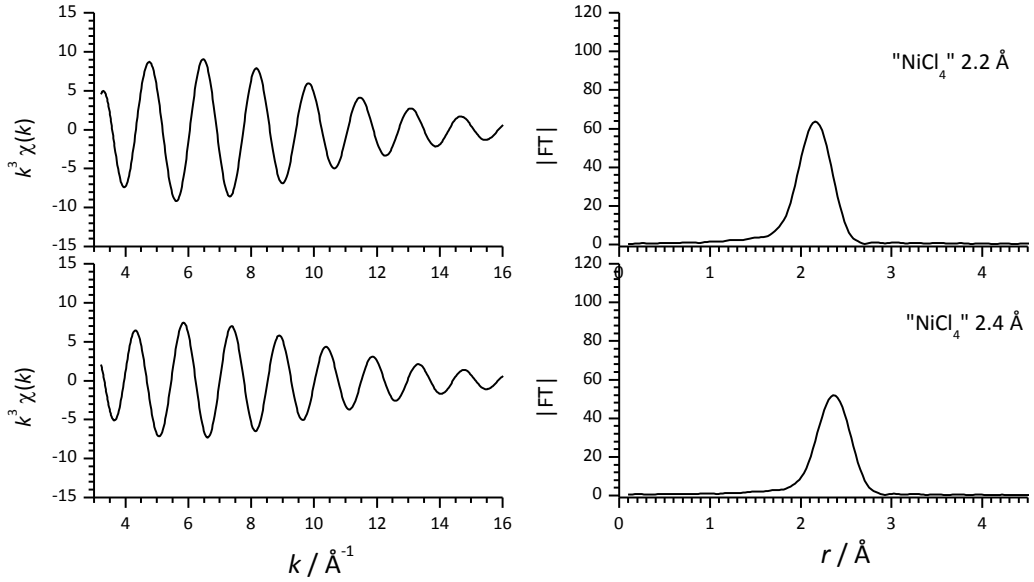

Figure 11. Effect of changing Ni-Cl interatomic distance, R_{as}, on Ni K-edge EXAFS and FT

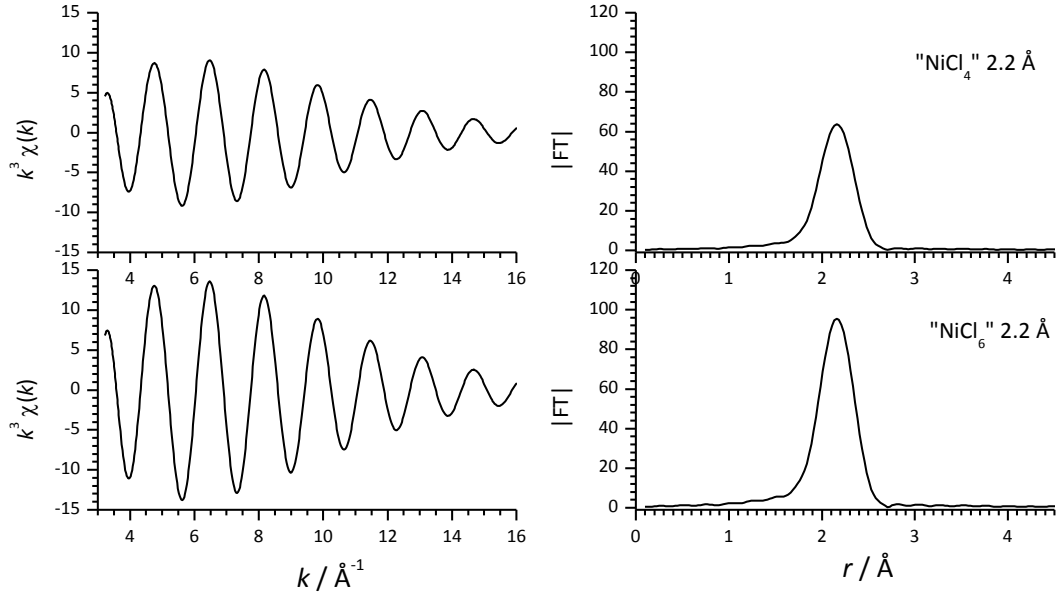

Figure 12. Effect of changing coordination number, *N*, on Ni K-edge EXAFS and FT

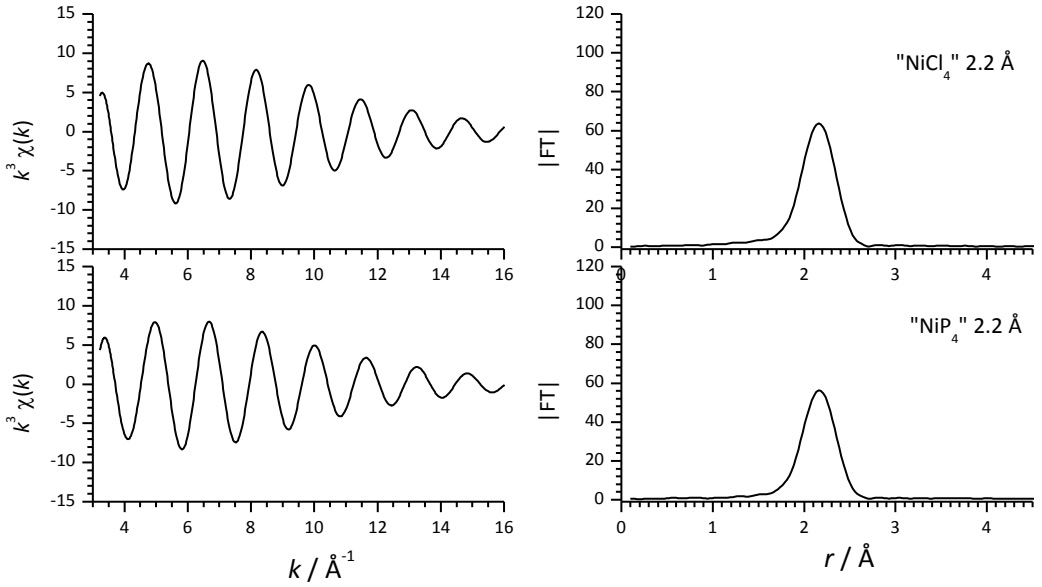

Figure 13. Effect of changing backscattering atom from Cl to P on Ni K-edge EXAFS and FT

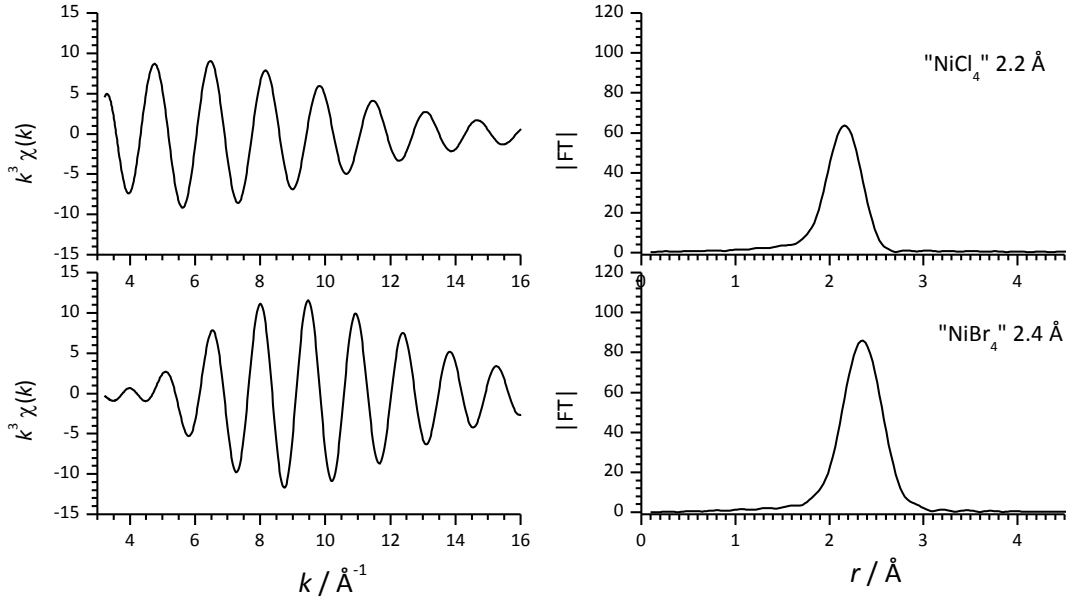

Figure 14. Effect of changing backscattering atom from Cl to Br on Ni K-edge EXAFS and FT.

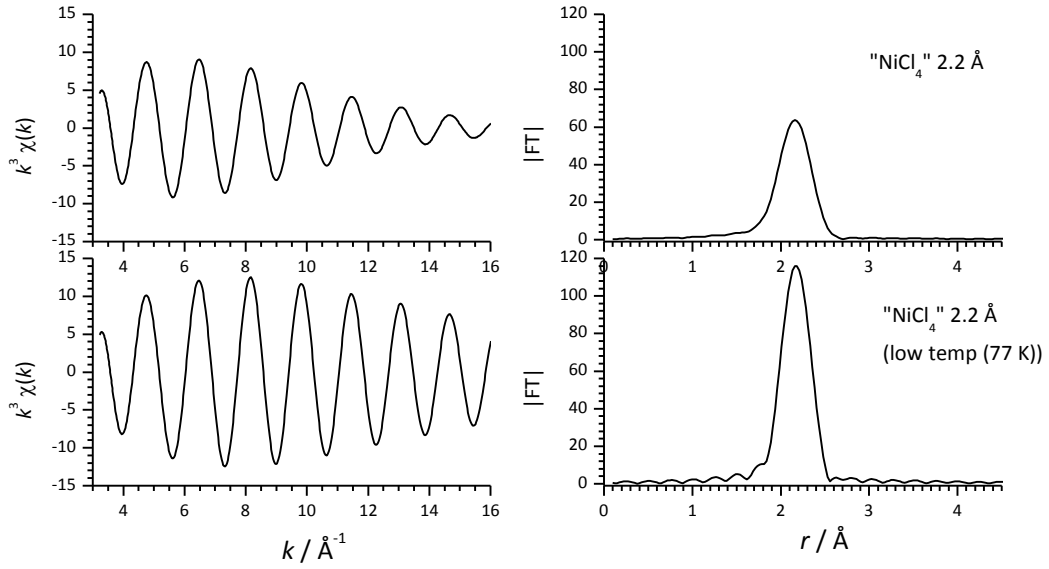

Figure 15. Effect of reducing Debye-Waller factor (reducing temperature) on Ni K-edge EXAFS and FT.

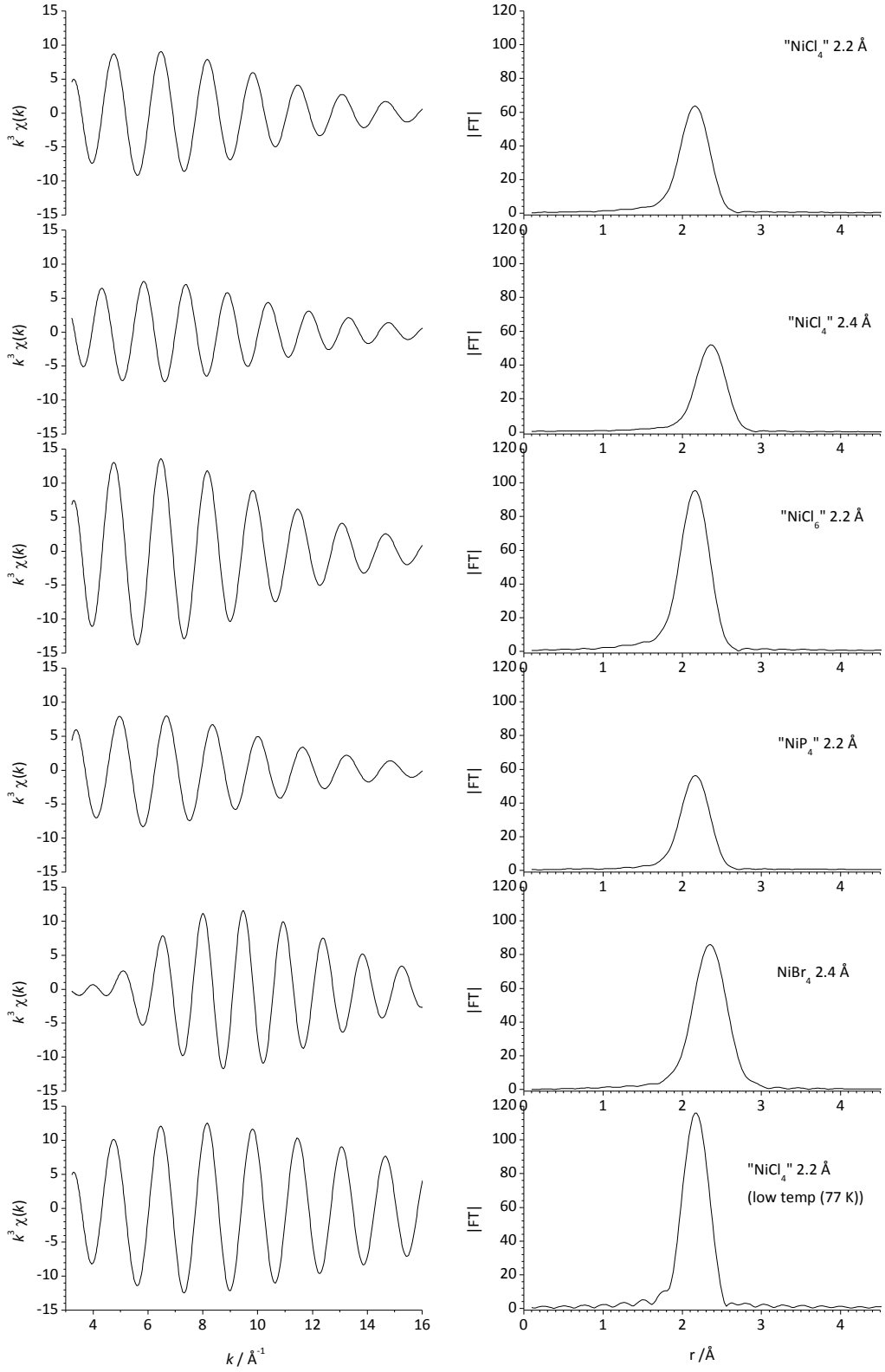

Figure 16. Summary of effects of changing parameters on Ni K-edge EXAFS and FT.

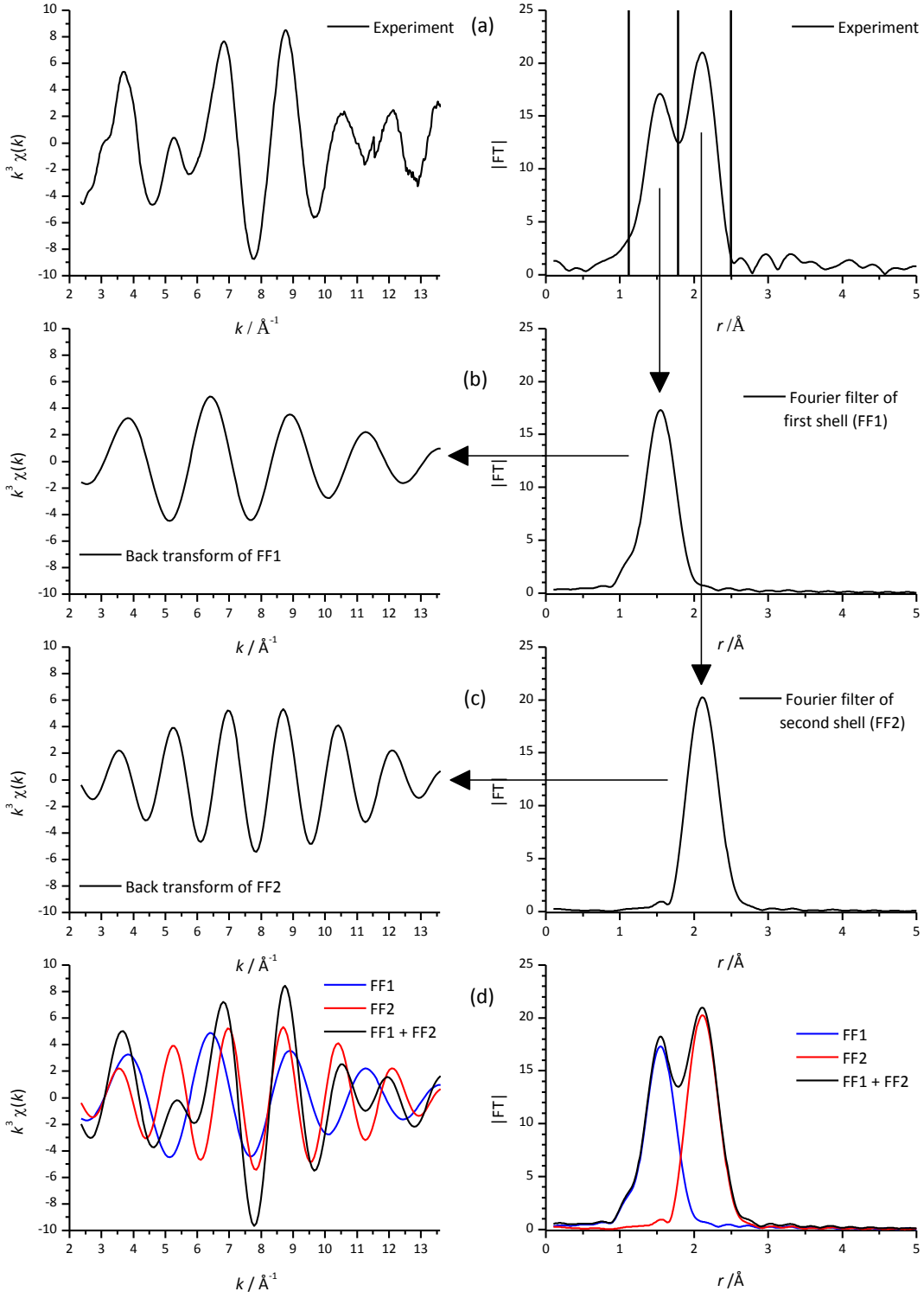

Figure 17. Example of Fourier filtering for Cr K-edge data for CrO_2Cl_2.

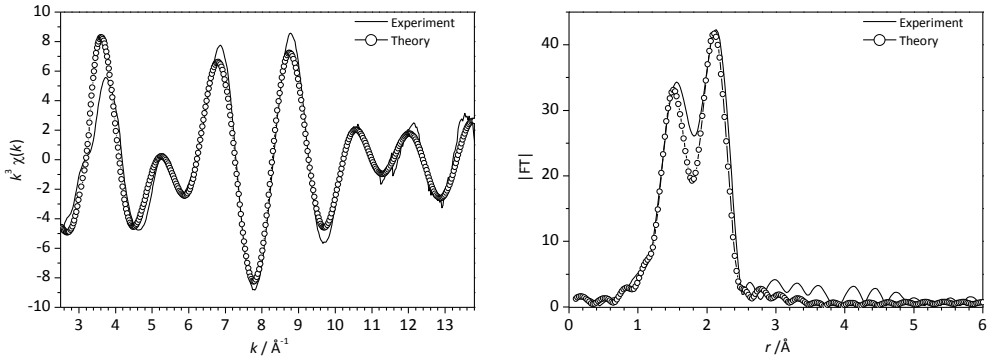

Figure 18. Cr K-edge EXAFS and FT for CrO_2Cl_2 at 10 K (data redrawn from M.D. Spicer, N.A. Young, J. Chem. Soc., Dalton Trans., (1991) 3133, [85]).

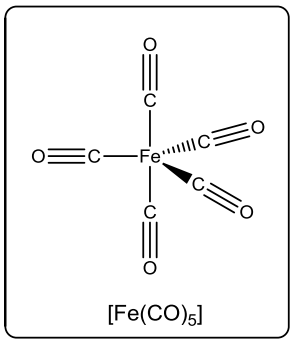

Figure 19. Structure of $[Fe(CO)_5]$

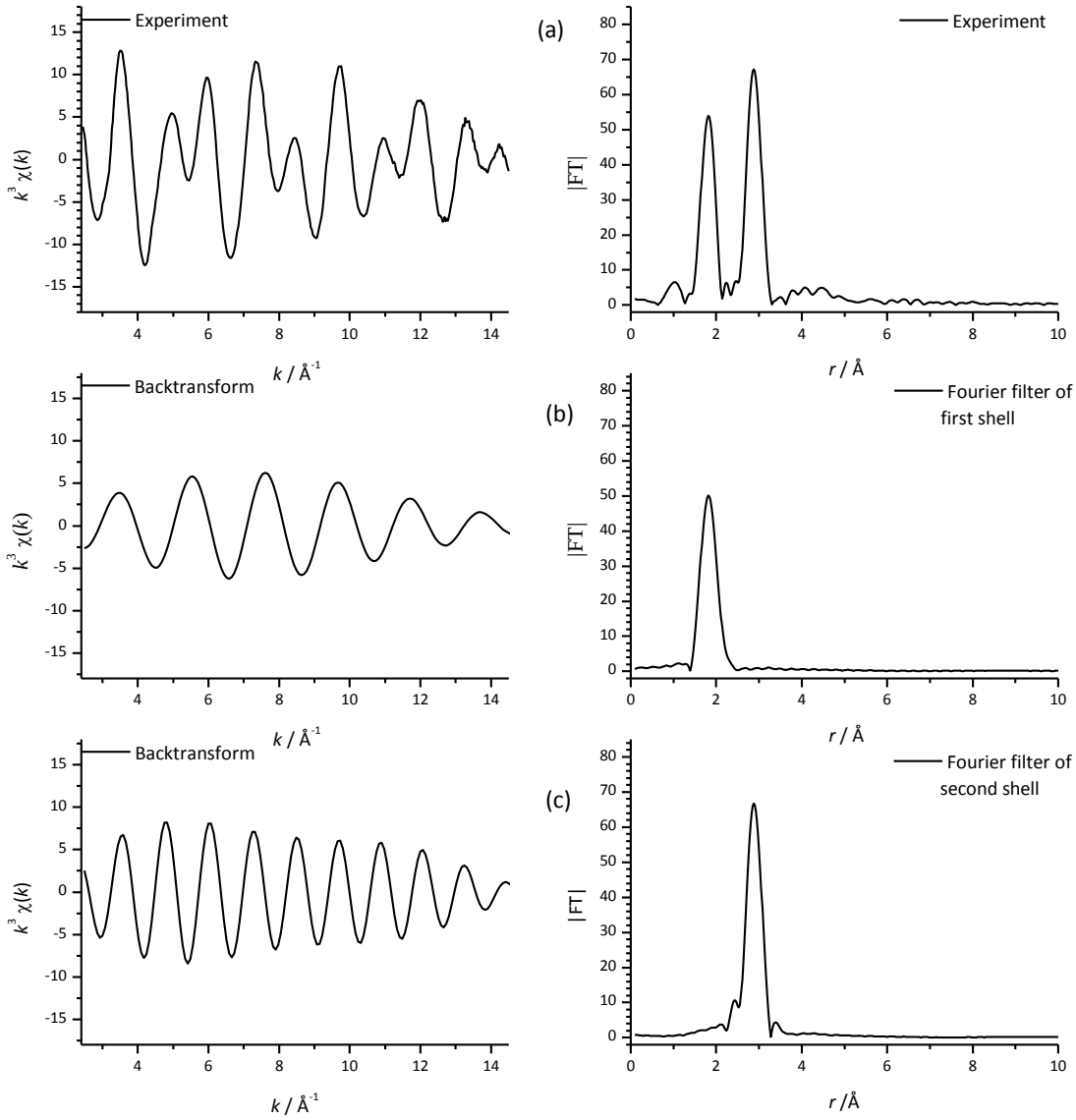

Figure 20. Fourier filtering of the Fe K-edge EXAFS data of [$Fe(CO)_5$] at 10 K.

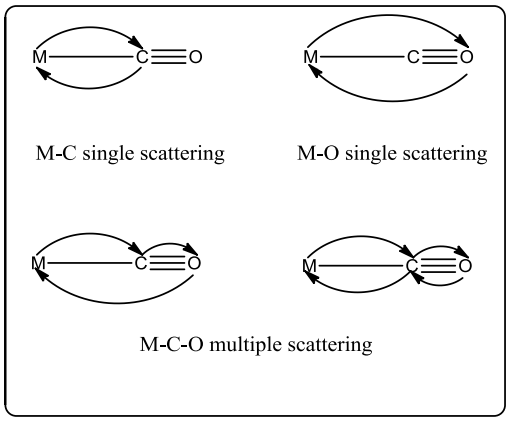

Figure 21. Significant single and multiple scattering pathways in metal carbonyl complexes.

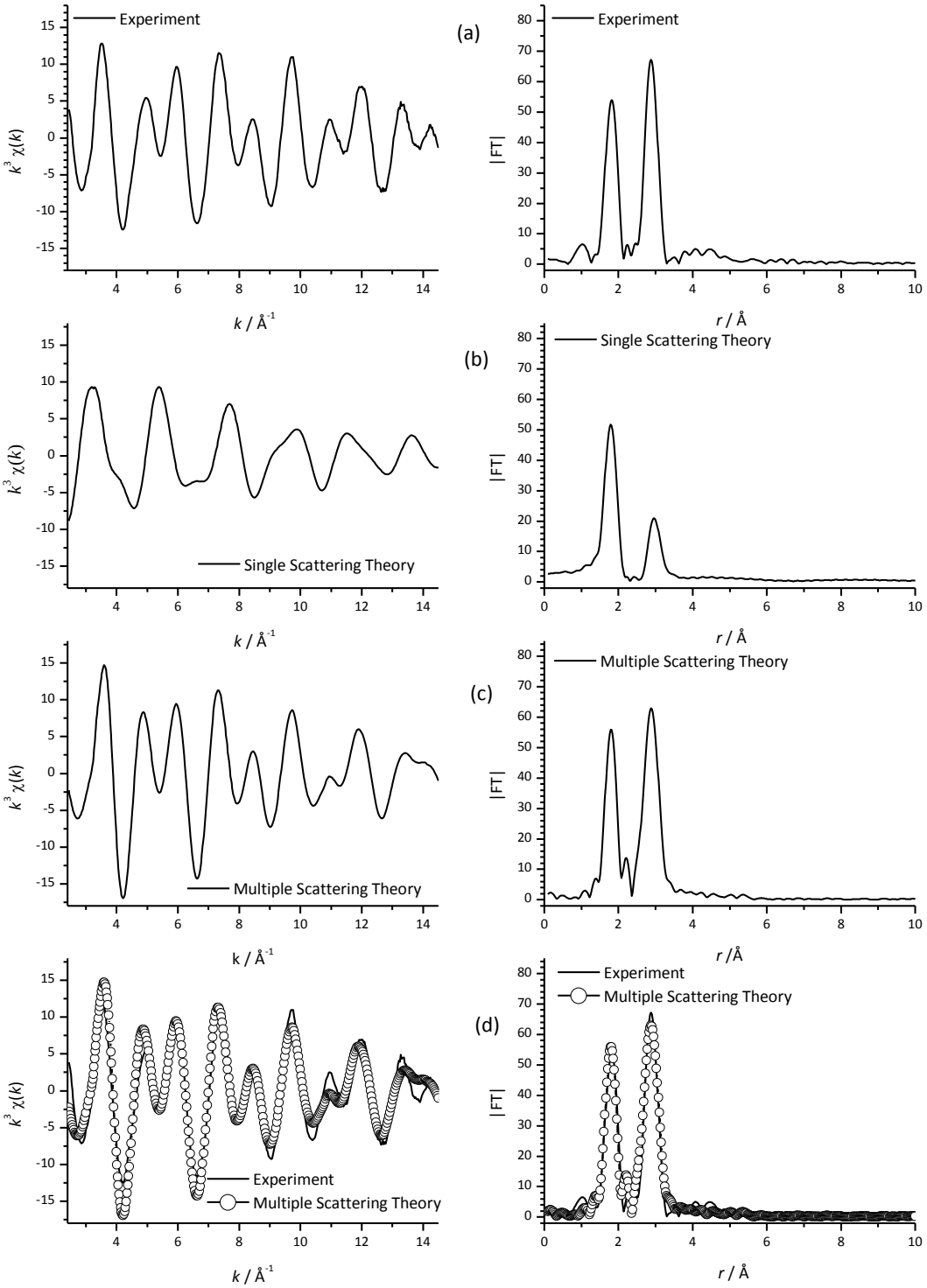

Figure 22. Fitting of Fe K-edge EXAFS and FT of [$Fe(CO)_5$] at 10 K (data redrawn from E.W. Robertson, O.M. Wilkin, N.A. Young, Polyhedron, 19 (2000) 1493, [170]).

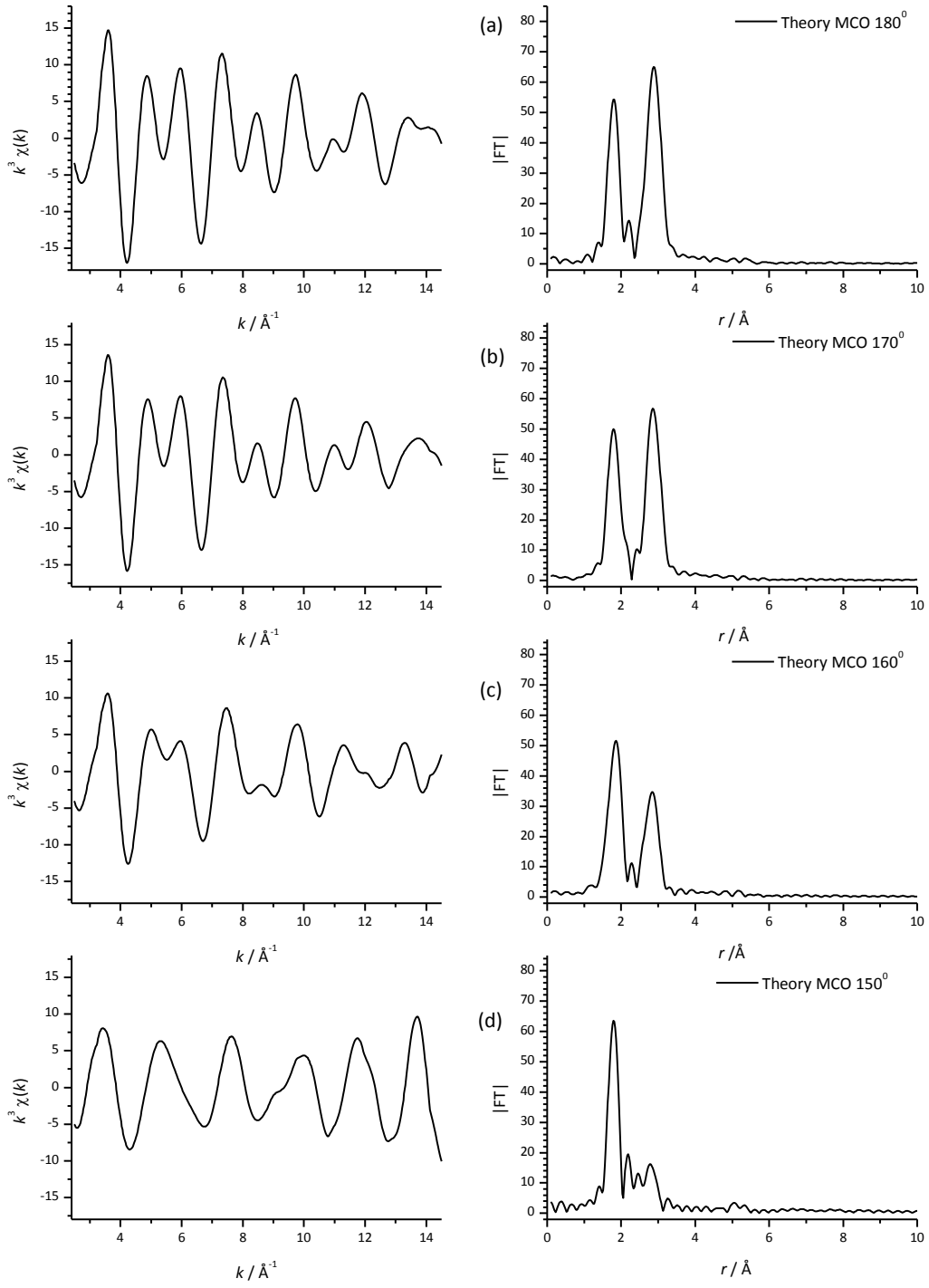

Figure 23. Effect of MCO bond angle on multiple scattering in Fe K-edge EXAFS and FT of $[Fe(CO)_5]$ at 10 K.

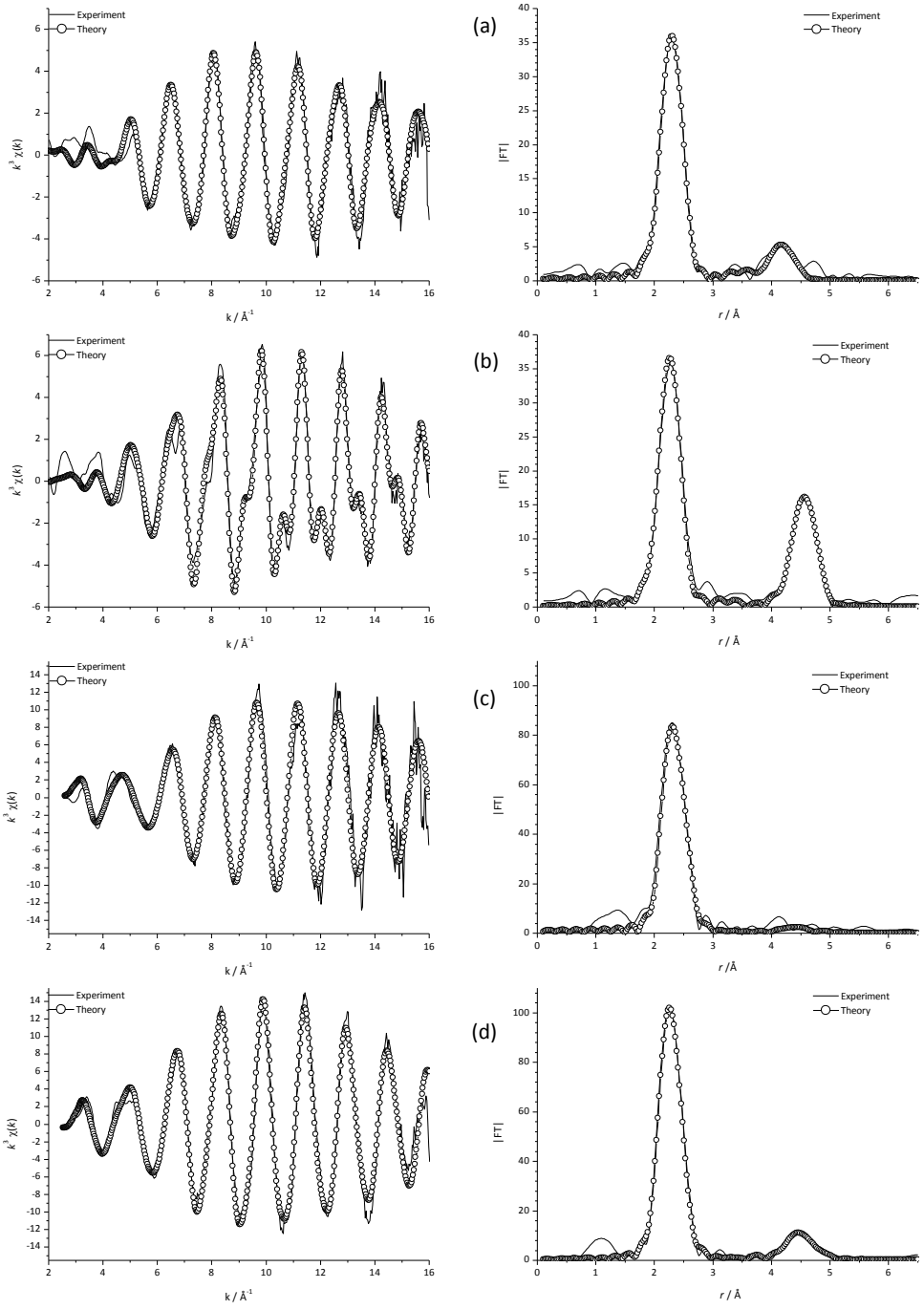

Figure 24. Br K-edge EXAFS (left) and FT (right) for (a) *tetrahedral*-[$NiBr_2(PPh_3)_2$] and (b) *trans*-[$NiBr_2(PEt_3)_2$]. Ni K-edge EXAFS (left) and FT (right) for (c) *tetrahedral*-[$NiBr_2(PPh_3)_2$] and (d) *trans*-[$NiBr_2(PEt_3)_2$]. All at 10 K. (Data redrawn from A. van der Gaauw, O.M. Wilkin, N.A. Young, J. Chem. Soc., Dalton Trans., (1999) 2405, [90], N. Binsted, A. van der Gaauw, O.M. Wilkin, N.A. Young, J. Synch. Rad., 6 (1999) 239, [91]).

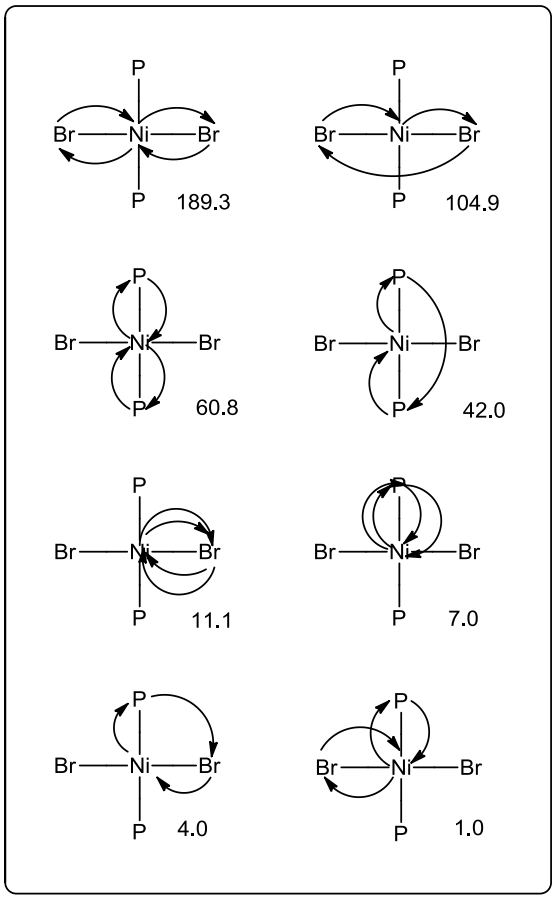

Figure 25. Diagrammatic representation of the relative importance of multiple scattering paths that contribute to the 2*R* features in Ni K-edge XAFS data of *trans*-[$NiBr_2(PEt_3)_2$] ((Data redrawn from A. van der Gaauw, O.M. Wilkin, N.A. Young, J. Chem. Soc., Dalton Trans., (1999) 2405, [90], N. Binsted, A. van der Gaauw, O.M. Wilkin, N.A. Young, J. Synch. Rad., 6 (1999) 239, [91]).

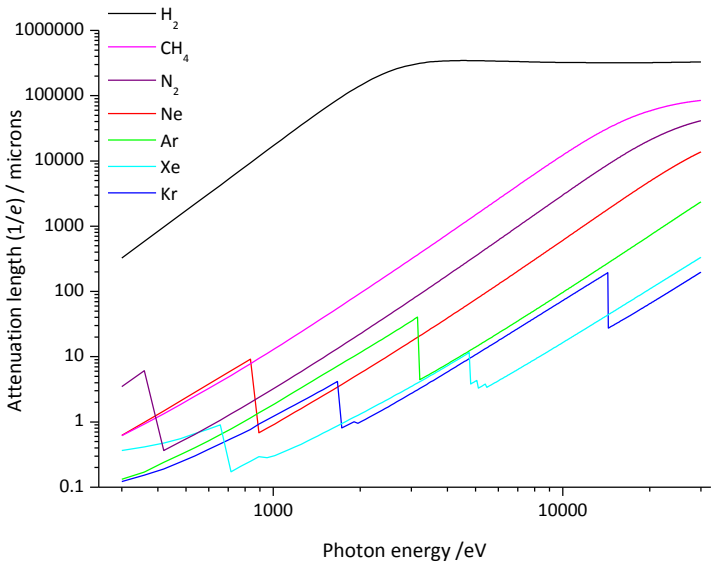

Figure 26. Plot of attenuation lengths (1/*e*) vs photon energy for common matrix gases.

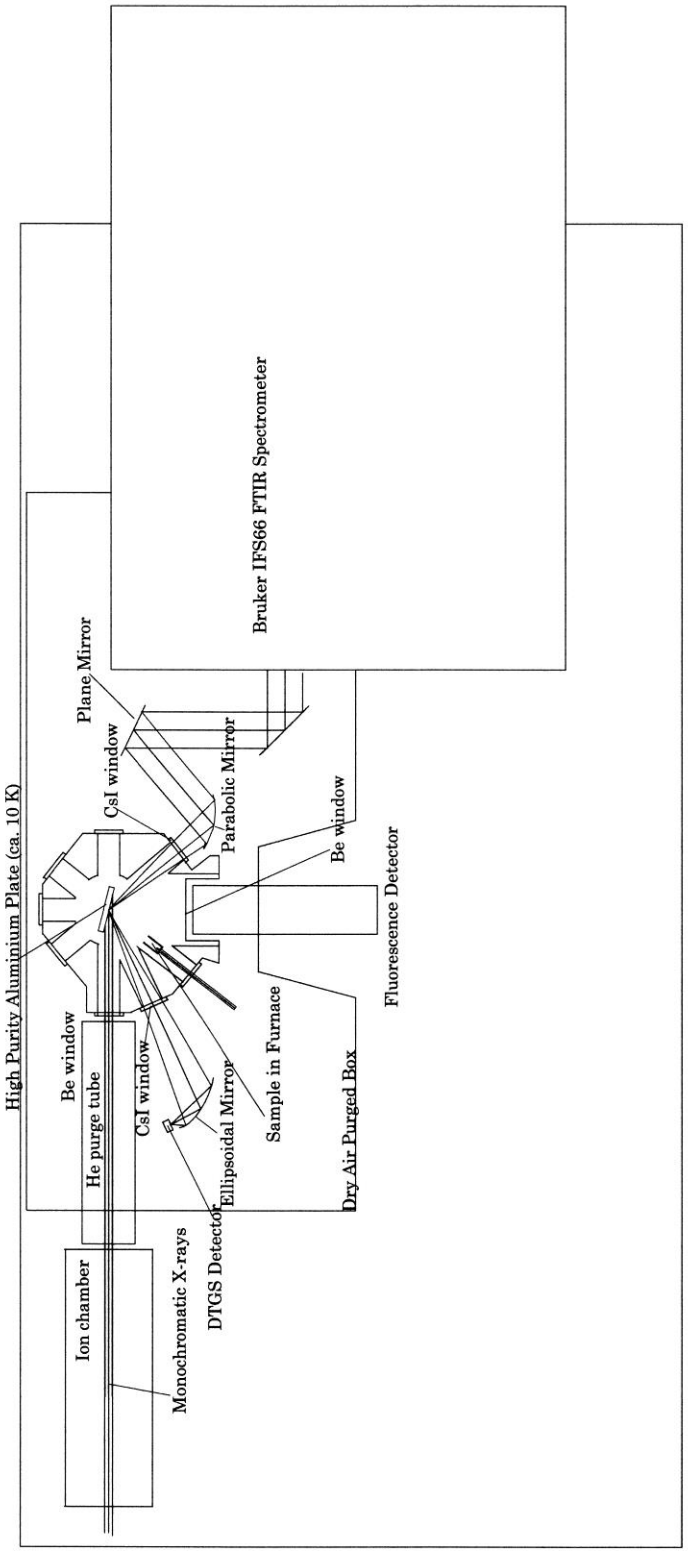

Figure 27. Schematic diagram of combined FTIR-EXAFS facility (after [103]).

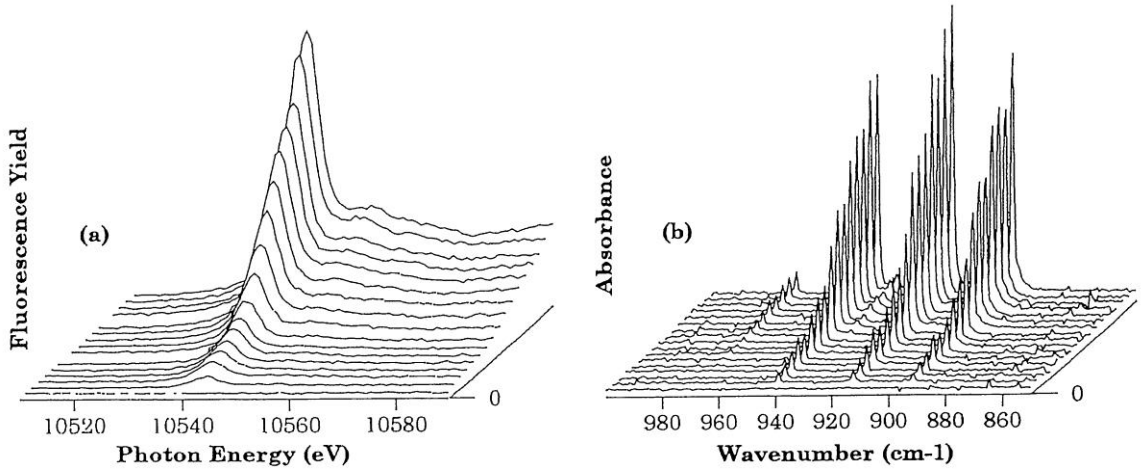

Figure 28. Simultaneous Re L_3-edge XANES (a) and FTIR (b) collected during deposition of molecular $RbReO_4$ into a nitrogen matrix at *ca*. 10 K. (reproduced with permission of the International Union of Crystallography from O.M. Wilkin, N.A. Young, J. Synch. Rad., 6 (1999) 204, [103].)

(I am the author of the original so prior permission is not required, but please note the following condition of copyright permission
"In electronic form, this acknowledgement must be visible at the same time as the reused materials, and must be hyperlinked to **Crystallography Journals Online** (http://journals.iucr.org/).")

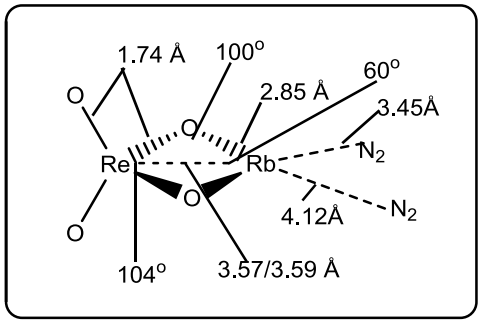

Figure 29. Summary of structural data from Re L_3-edge and Rb K-edge EXAFS for $RbReO_4$ in a N_2 matrix (redrawn from O.M. Wilkin, N.A. Young, J. Synch. Rad., 6 (1999) 204, [103])

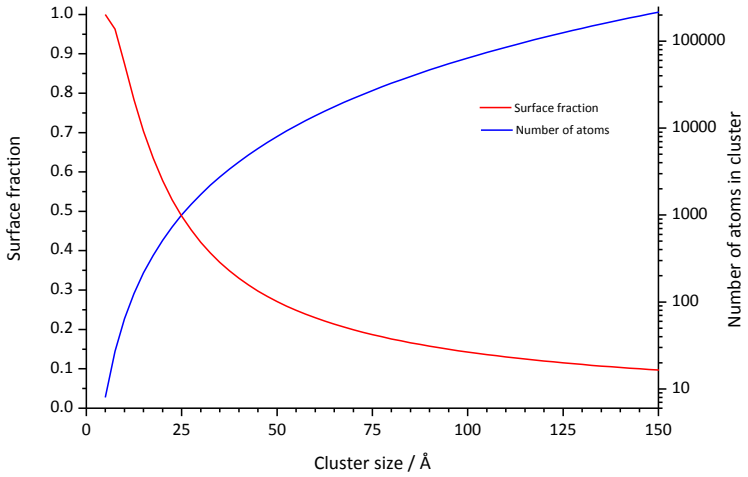

Figure 30. Illustration of the relationship between surface fraction, cluster size and the number of atoms in a prototypical cubic cluster with atoms of 2.5 Å diameter (based on E. Roduner, Chem. Soc. Rev., 35 (2006) 583, [112]).

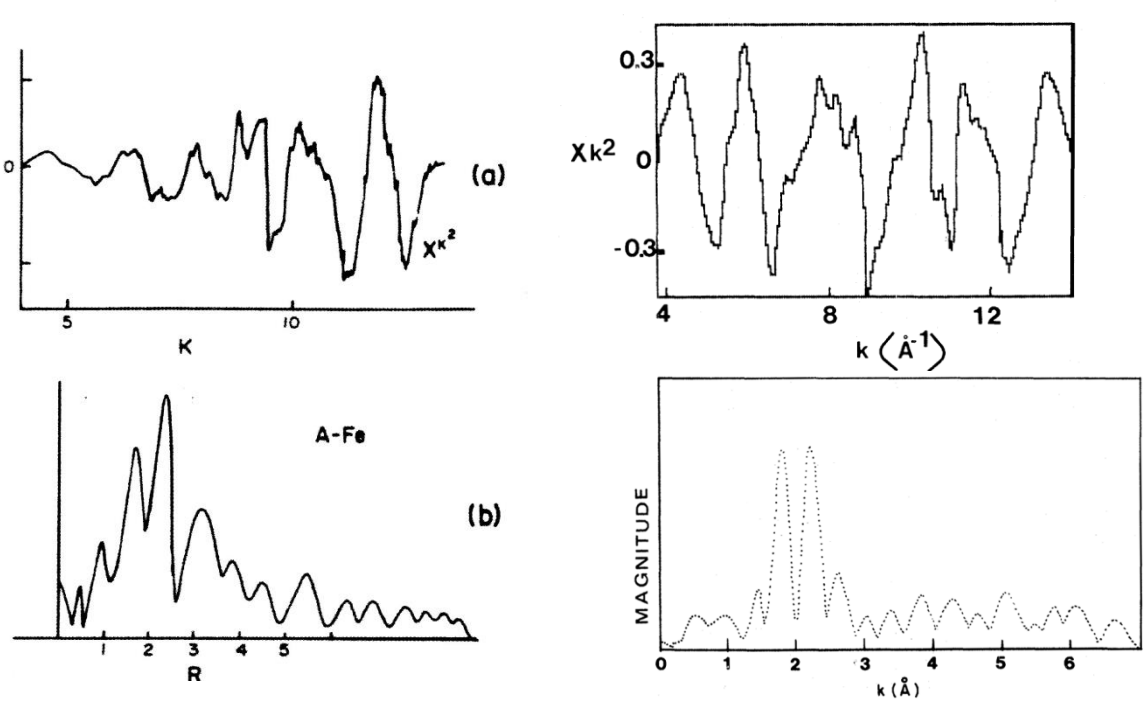

Figure 31. Fe K-edge $k^2\chi(k)$ EXAFS (a) and FT (b) for 0.1 at% Fe in solid Ar (left) [117]. 0.4 at% Fe in solid neon (right) [118] (reproduced with permission of Elsevier from P.A. Montano, Shenoy, G. K., Solid State Commun., 35 (1980) 53, [117] and H. Purdum, P.A. Montano, G.K. Shenoy, T. Morrison, Phys. Rev. B, 25 (1982) 4412, [118],).

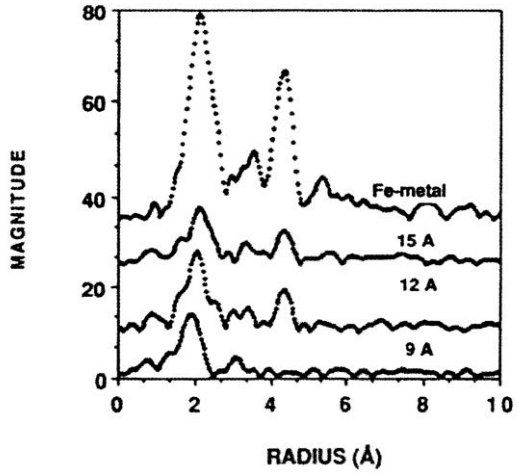

Figure 32. Magnitude of the Fourier transforms of $k^2\chi(k)$ for Fe clusters isolated in solid Ar at 4.2 K (reproduced with permission of IOP Publishing from P.A. Montano, Y. Cao, J. Phys. Conds. Mat., 5 (1993) A209, [125]).

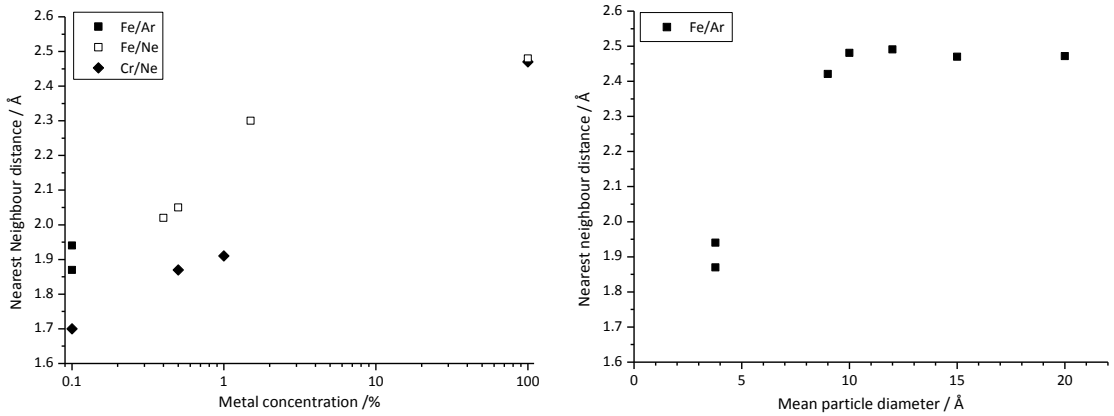

Figure 33. Nearest neighbour distances versus metal concentration (left) ([118, 120, 121, 123, 124]) and mean particle diameter (right) ([118, 120, 121, 123, 124]) for matrix isolated metal molecules and clusters. (Data redrawn from H. Purdum, P.A. Montano, G.K. Shenoy, T. Morrison, Phys. Rev. B, 25 (1982) 4412, [118]; P.A. Montano, G.K. Shenoy, T.I. Morrison, W. Schulze, Springer Proc. Phys., 2 (1984) 231, [120]; P.A. Montano, H. Purdum, G.K. Shenoy, T.I. Morrison, W. Schulze, Surf. Sci., 156 (1985) 228, [121]; P.A. Montano, J. Zhao, M. Ramanathan, G.K. Shenoy, W. Schulze, Z. Phys. D, 12 (1989) 103, [123]; J. Zhao, M. Ramanathan, P.A. Montano, G.K. Shenoy, W. Schulze, Mater. Res. Soc. Symp. Proc., 143 (1989) 151, [124]

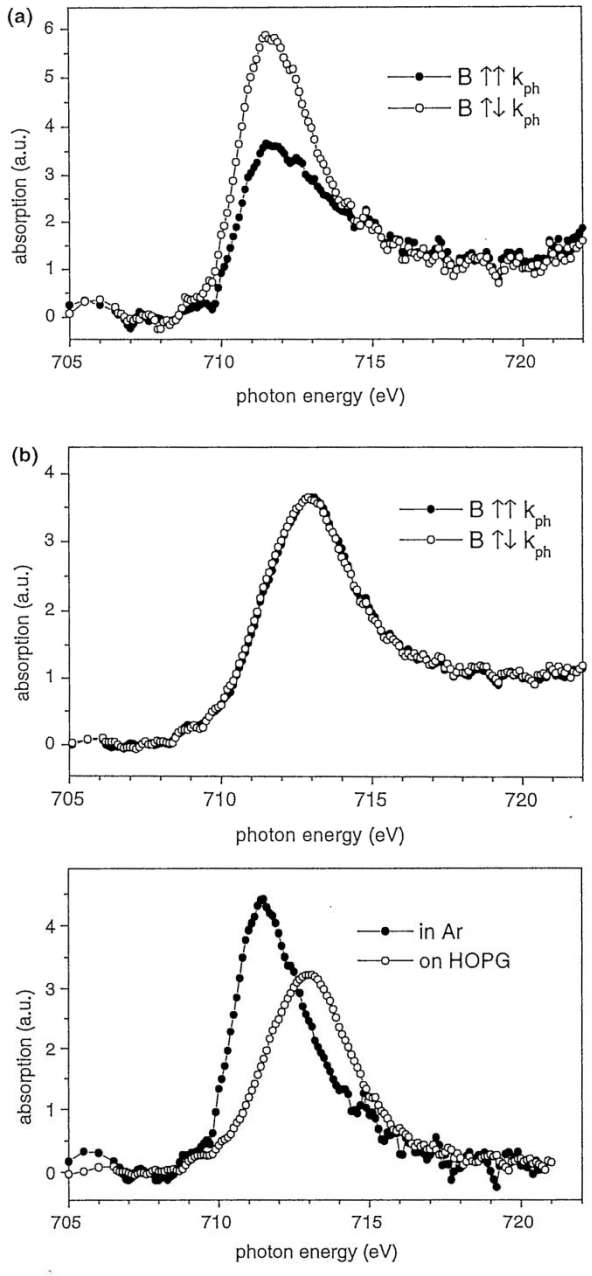

Figure 34. (a) Fe L_3-edge MXCD spectra from Ar matrix isolated Fe clusters (the applied field being oriented parallel (⇉) and anti-parallel (⇄) with respect to the light propagation direction). (b) Same spectra as before, but after removal of the Ar layer. Bottom spectrum is the non-magnetic data (reproduced with permission of Elsevier from K. Fauth, S. Gold, M. Hessler, N. Schneider, G. Schütz, Chem. Phys. Lett., 392 (2004) 498, [68]).

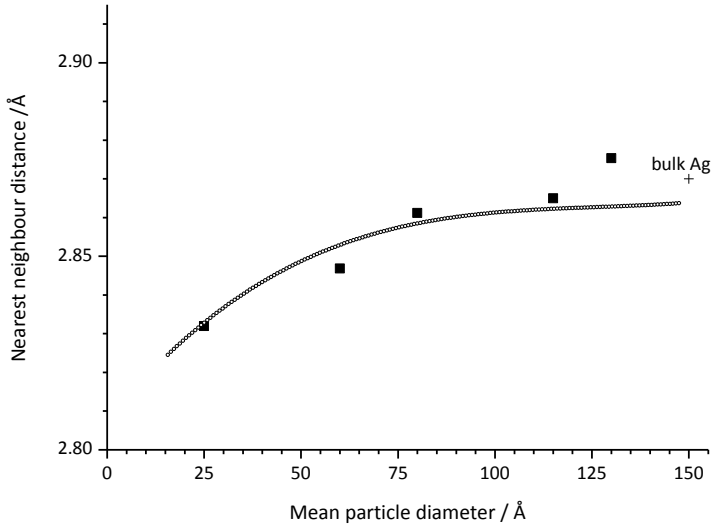

Figure 35. Plot of the nearest neighbour distances *vs*. mean particle size for Ag clusters in solid argon. The line is the fit of the cluster contraction with a surface stress of 2286 dyne cm^{-1} (data redrawn from P.A. Montano, W. Schulze, B. Tesche, G.K. Shenoy, T.I. Morrison, Phys. Rev. B, 30 (1984) 672, [138]).

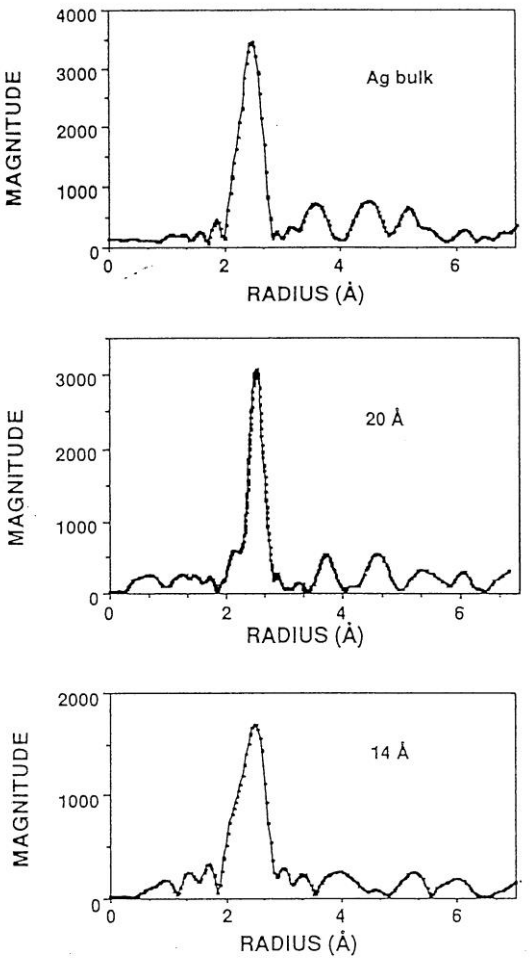

Figure 36. Magnitude of the Fourier transform of $k^3\chi(k)$ for silver metal at 78 K (top), 20 Å clusters (middle) and 14 Å clusters (bottom) in solid Ar at 4.2 K (reproduced with permission by Elsevier from P.A. Montano, J. Zhao, M. Ramanathan, G.K. Shenoy, W. Schulze, J. Urban, Chem. Phys. Lett., 164 (1989) 126, [111])

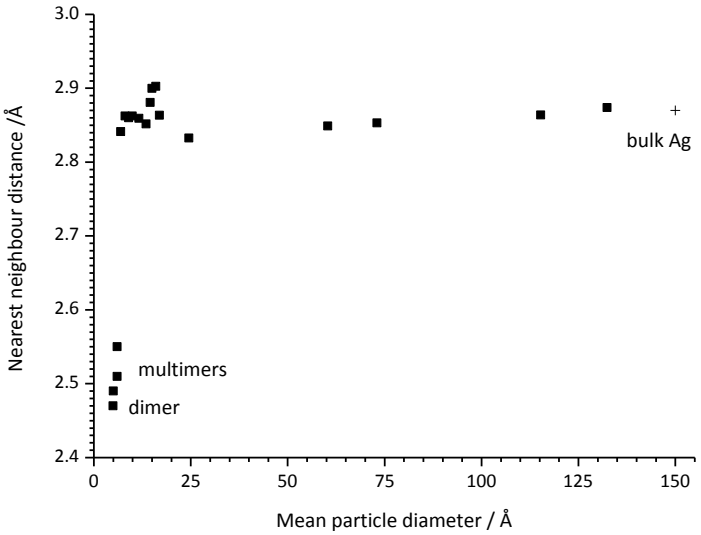

Figure 37. Nearest neighbour distances *vs*. cluster diameter for Ag clusters in solid argon. The data below 25 Å are redrawn from P.A. Montano, J. Zhao, M. Ramanathan, G.K. Shenoy, W. Schulze, J. Urban, Chem. Phys. Lett., 164 (1989) 126, [111]; those above 25 Å are redrawn from P.A. Montano, W. Schulze, B. Tesche, G.K. Shenoy, T.I. Morrison, Phys. Rev. B, 30 (1984) 672, [138].

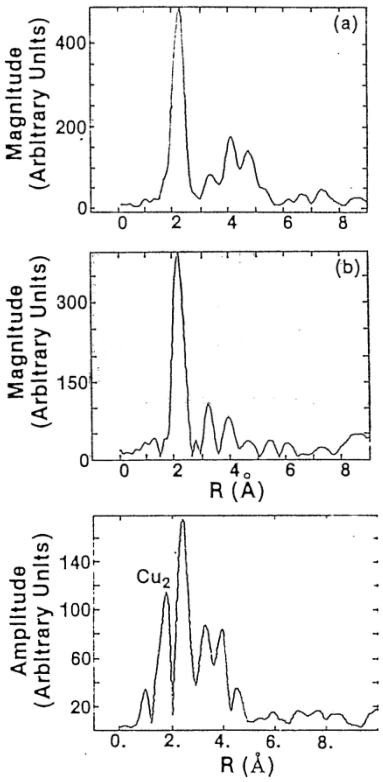

Figure 38. Magnitude of the FT of $k^3\chi(k)$ of Cu metal (top), 10 Å mean diameter Cu clusters in solid argon (middle) and 6-7 Å mean diamter Cu clusters in solid argon (bottom) (reproduced with permission from P.A. Montano, G.K. Shenoy, E.E. Alp, W. Schulze, J. Urban, Phys. Rev. Lett., 56 (1986) 2076, [126]).

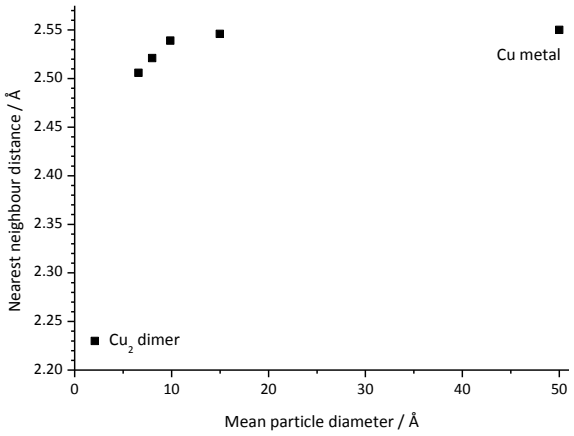

Figure 39. Summary of variation in Cu-Cu nearest neighbour distance as a function of particle size (data redrawn from P.A. Montano, G.K. Shenoy, E.E. Alp, W. Schulze, J. Urban, Phys. Rev. Lett., 56 (1986) 2076, [126]).

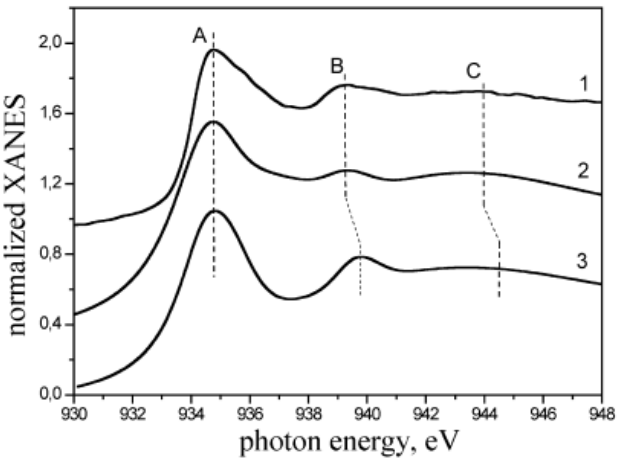

Figure 40. Cu L_3 XANES spectra of: (1) experiment of Cu_{13} cluster in an argon matrix; (2) theoretical curve for a Cu_{13} cluster in an argon matrix with icosahedral core-shell $Cu_{13}Ar_{42}$ cluster (3) theoretical curve for a Cu_{13} cluster in an argon matrix for a cuboctahedral core-shell $Cu_{13}Ar_{42}$ cluster (reproduced with permission from V.L. Mazalova, A.V. Soldatov, S. Adam, A. Yakovlev, T. Möller, R.L. Johnston, J. Phys. Chem. C, 113 (2009) 9086, [69], copyright (2009) American Chemical Society).

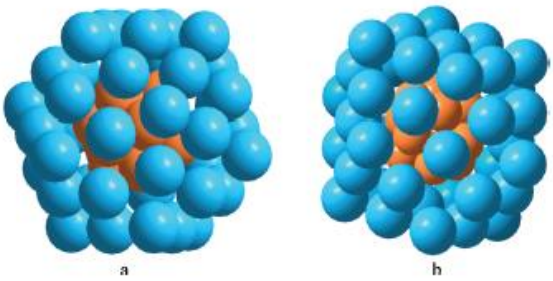

Figure 41. Pictorial view of (a) the icosahedral core-shell $Cu_{13}Ar_{42}$cluster and (b) the cuboctahedral core-shell $Cu_{13}Ar_{42}$ cluster (Cu_{13} forms the core, which is surrounded by 42 Ar atoms) (reproduced with permission from V.L. Mazalova, A.V. Soldatov, S. Adam, A. Yakovlev, T. Möller, R.L. Johnston, J. Phys. Chem. C, 113 (2009) 9086, [69] copyright (2009) American Chemical Society).

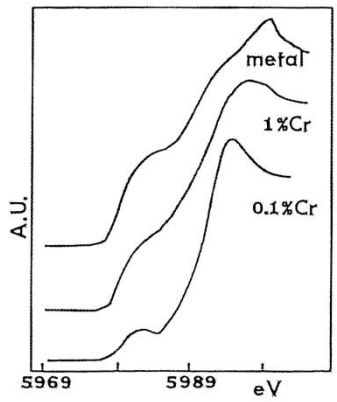

Figure 42. Cr K-edge XANES for metallic Cr (top), 1 at% Cr in solid Ne (middle) and 0.1 at% Cr in solid Ne (bottom) (reproduced with permission of Elsevier from P.A. Montano, H. Purdum, G.K. Shenoy, T.I. Morrison, W. Schulze, Surf. Sci., 156 (1985) 228, [121]).

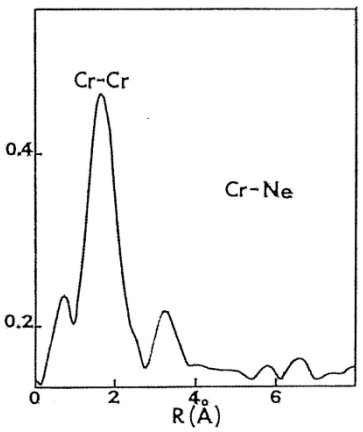

Figure 43. FT of Cr K-edge $k^3\chi(k)$ EXAFS of 1at% Cr in solid neon (reproduced with permission of Elsevier from P.A. Montano, H. Purdum, G.K. Shenoy, T.I. Morrison, W. Schulze, Surf. Sci., 156 (1985) 228, [121]).

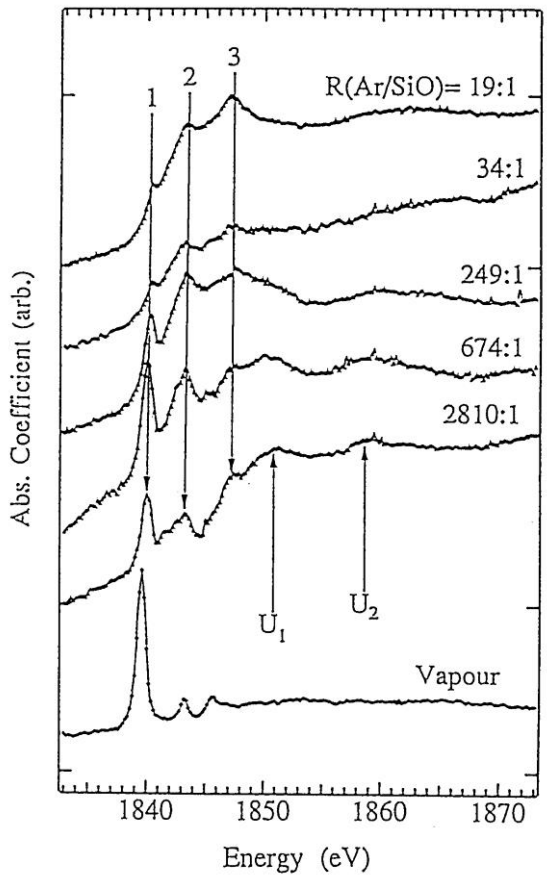

Figure 44. Si K-edge XANES spectra of SiO clusters in solid argon at different concentrations (reproduced with permission of Springer Science and Business Media from A.M. Flank, R.C. Karnatak, C. Blancard, J.M. Esteva, P. Lagarde, J.P. Connerade, Z. Phys. D, 21 (1991) 357, [148]).

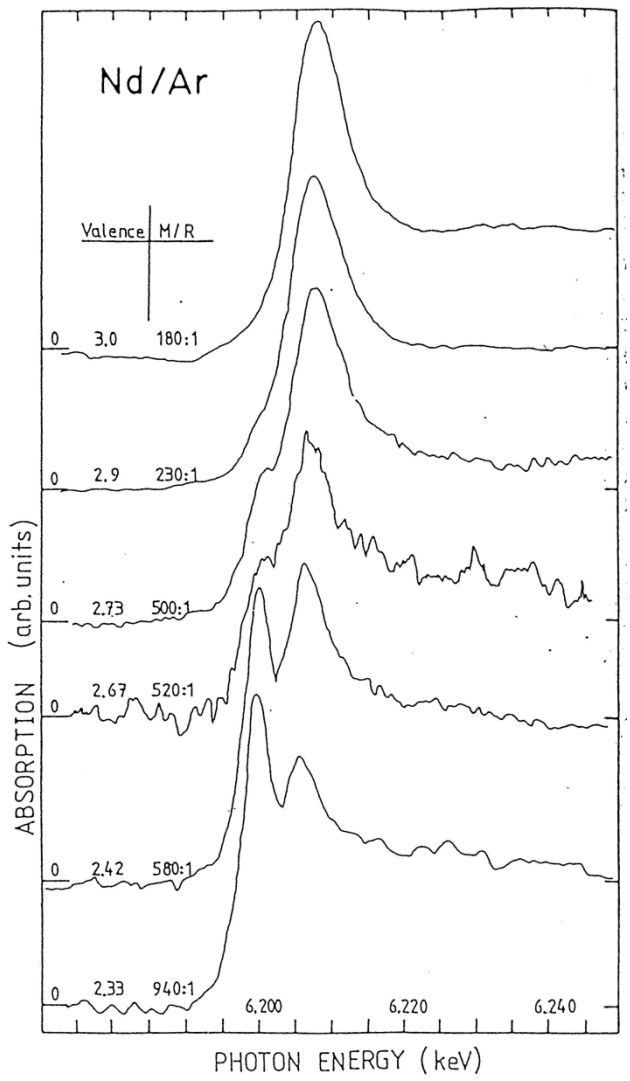

Figure 45. Nd L_3 absorption edge spectra of Nd clusters isolated in solid Ar, the valency and the Ar:Nd ratio are indicated (reproduced with permission from M. Lübcke, B. Sonntag, W. Niemann, P. Rabe, Phys. Rev. B, 34 (1986) 5184, [155]).

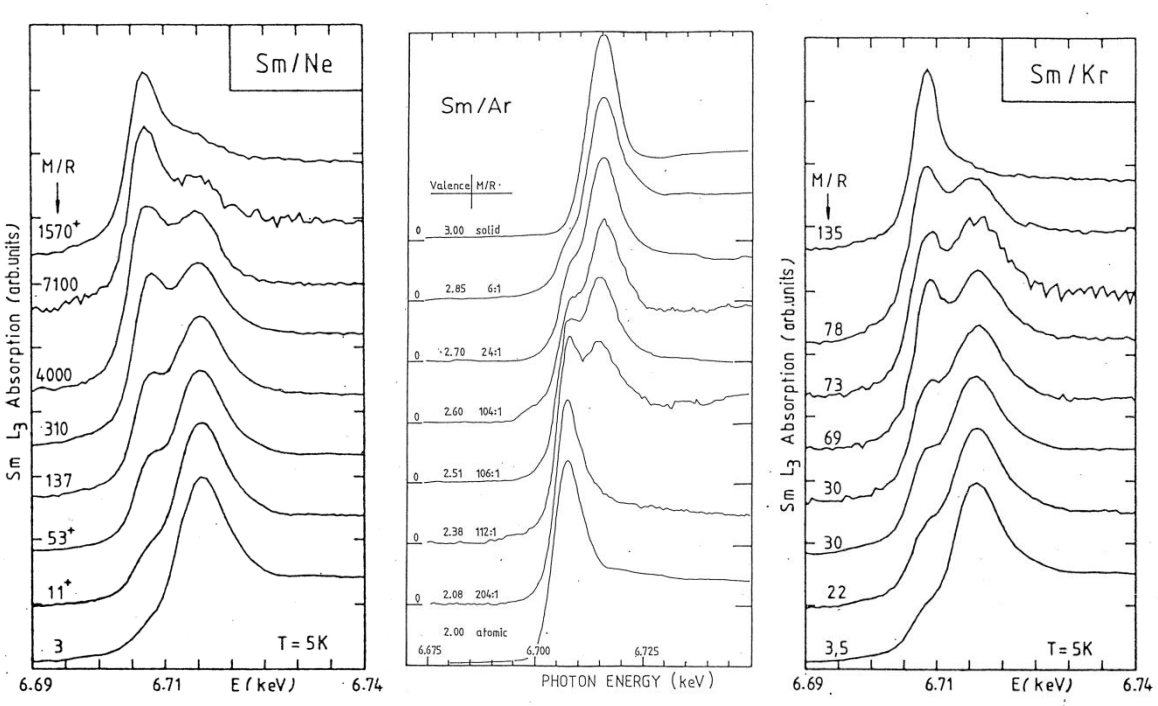

Figure 46. Sm L_3 absorption edge spectra of Sm clusters isolated in solid Ne [158] solid Ar [155] and solid Kr [158]. Note the cluster concentration (M/R) is reversed for the Ar data compared to the Ne and Kr data, as is the valency (reproduced with permission from M. Lübcke, B. Sonntag, W. Niemann, P. Rabe, Phys. Rev. B, 34 (1986) 5184, [155] and W. Niemann, W. Malzfeldt, P. Rabe, R. Haensel, M. Lübcke, Phys. Rev. B, 35 (1987) 1099, [158])

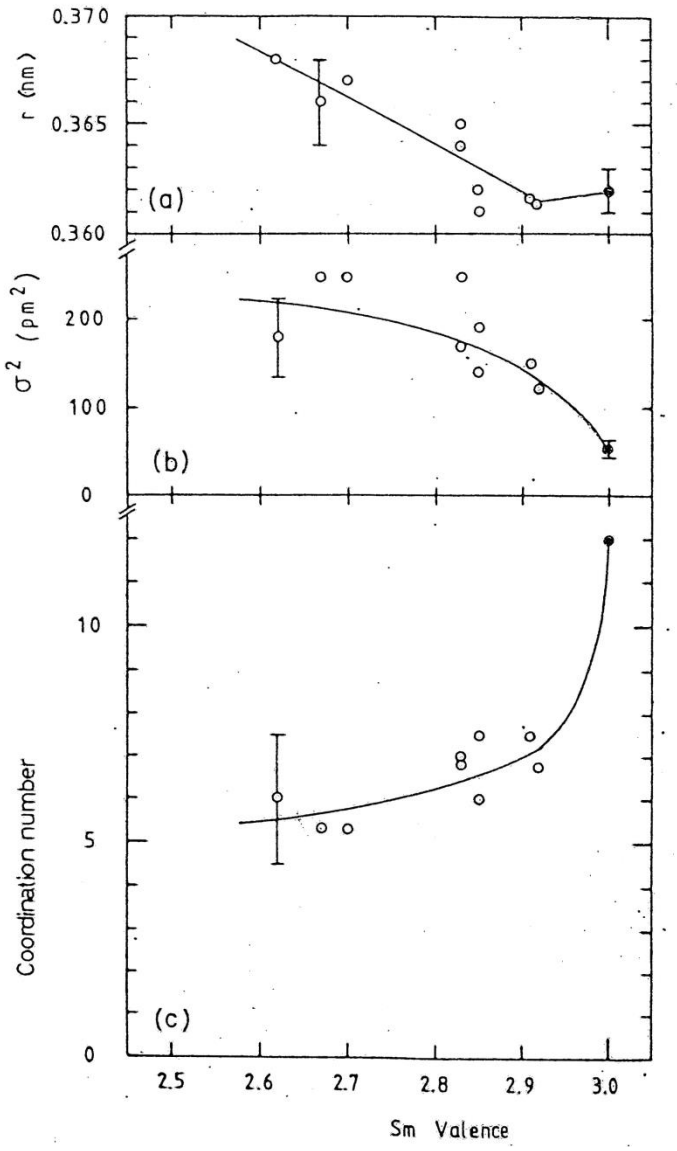

Figure 47. EXAFS fit results for Sm clusters in Ne, Ar and Kr matrices. The nearest neighbour distance *r*, mean square displacement σ^2 and coordination number *N* are plotted against the mean Sm valence. Values for solid Sm are given by ⊡ (reproduced with permission from W. Niemann, W. Malzfeldt, P. Rabe, R. Haensel, M. Lübcke, Phys. Rev. B, 35 (1987) 1099, [158]).

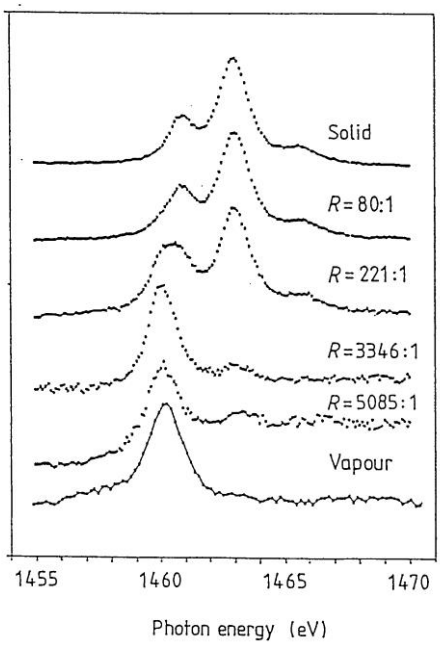

Figure 48. Tm M_5 spectra of Tm clusters in solid argon (reproduced with permission of IOP Publishing from C. Blancard, J.M. Esteva, R.C. Karnatak, J.P. Connerade, U. Kuetgens, J. Hormes, J. Phys. B At. Mol. Opt. Phys., 22 (1989) L575, [159] © IOP Publishing. All rights reserved).

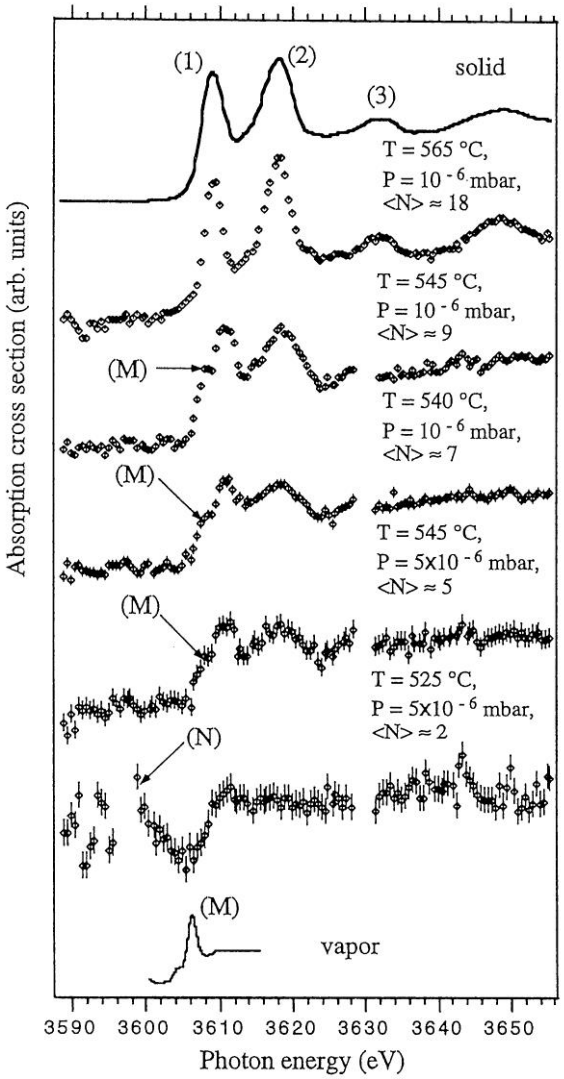

Figure 49. Potassium K-edge spectra of solid KF, KF clusters in solid Ar, and KF molecular vapour. For the cluster spectra the expansion source temperature and estimated cluster size <N> are given. (Reproduced with permission of Elsevier from C.M. Teodorescu, M. Womes, A. El Afif, R.C. Karnatak, J.M. Esteva, A.M. Flank, P. Lagarde, J. Electron Spectrosc. Relat. Phenom., 103 (1999) 205, [164])

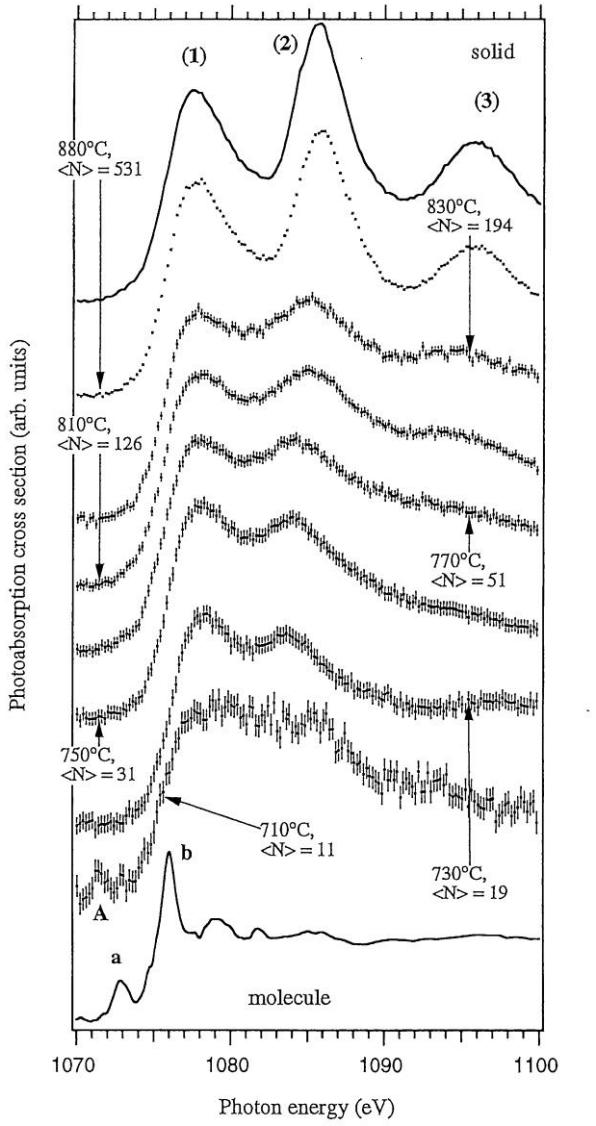

Figure 50. Na K-edge spectra of molecular NaF in the gas phase, NaF clusters embedded in solid Kr and solid NaF. For the cluster spectra the expansion source temperature and estimated cluster size <N> are given. (Reproduced with permission of Elsevier from C.M. Teodorescu, J.M. Esteva, M. Womes, A. El Afif, R.C. Karnatak, A.M. Flank, P. Lagarde, J. Electron Spectrosc. Relat. Phenom., 106 (2000) 233, [165]).

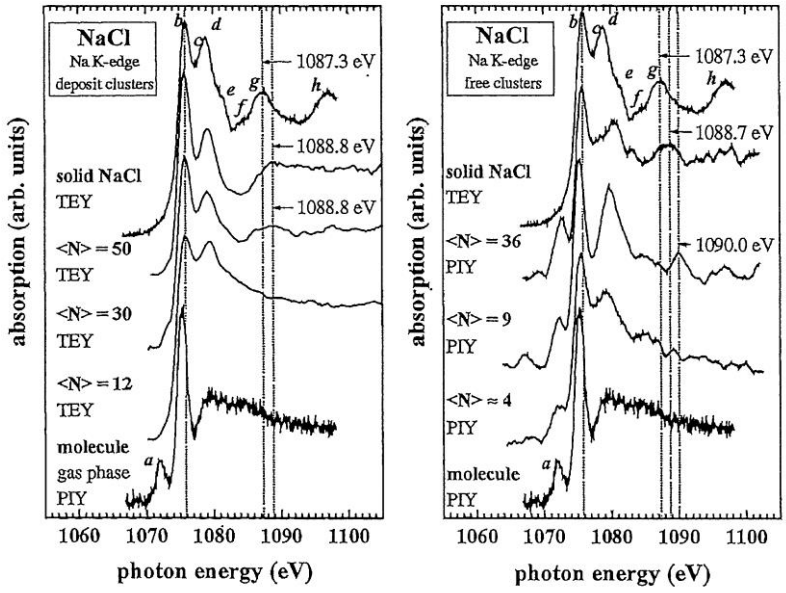

Figure 51. Na K-edge absorption spectra of free and deposited NaCl clusters. <N> is the number of molecules per cluster. (Reproduced with permission from M. Riedler, A.R.B. de Castro, A. Kolmakov, J.O. Löfken, C. Nowak, A.V. Soldatov, A. Wark, G. Yalovega, T. Möller, J. Chem. Phys., 115 (2001) 1319, [166, 167], copyright (2001), AIP Publishing LLC. Reproduced with permission from M. Riedler, A.R.B. de Castro, A. Kolmakov, J.O. Löfken, C. Nowak, A.V. Soldatov, A. Wark, G. Yalovega, T. Möller, Phys. Rev. B, 64 (2001) 245419, [166])

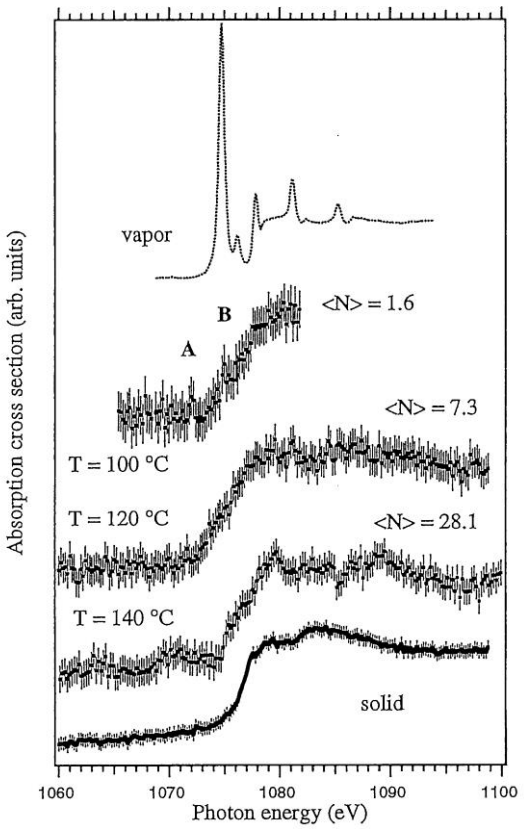

Figure 52. Na K-edge spectra of Na vapour, Na clusters in solid argon and solid Na. For the cluster spectra the expansion source temperature and estimated cluster size <N> are given. (Reproduced with permission of Elsevier from C.M. Teodorescu, J.M. Esteva, M. Womes, A. El Afif, R.C. Karnatak, A.M. Flank, P. Lagarde, J. Electron Spectrosc. Relat. Phenom., 106 (2000) 233, [165]).

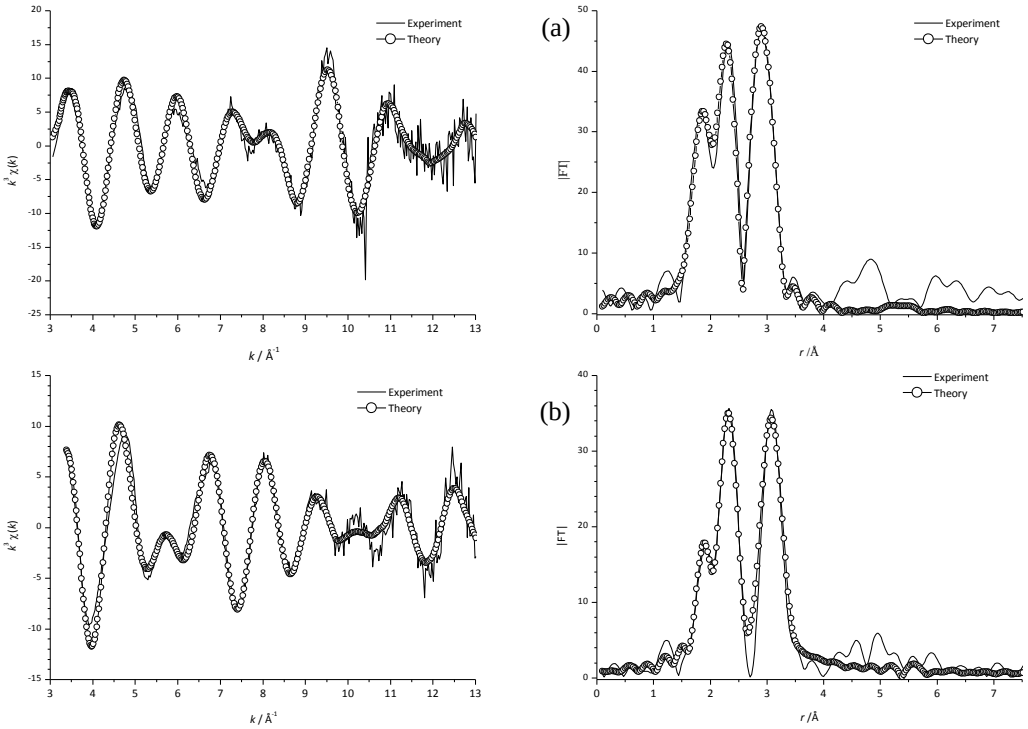

Figure 53. (a) Fe K-edge EXAFS (left) and FT (right) for $FeCl_2$ in solid CO at 10 K. (b) Cr K-edge EXAFS (left) and FT (right) for $CrCl_2$ in solid CO at 10 K. (Data redrawn from I.R. Beattie, P.J. Jones, N.A. Young, J. Am. Chem. Soc., 114 (1992) 6146, [171])

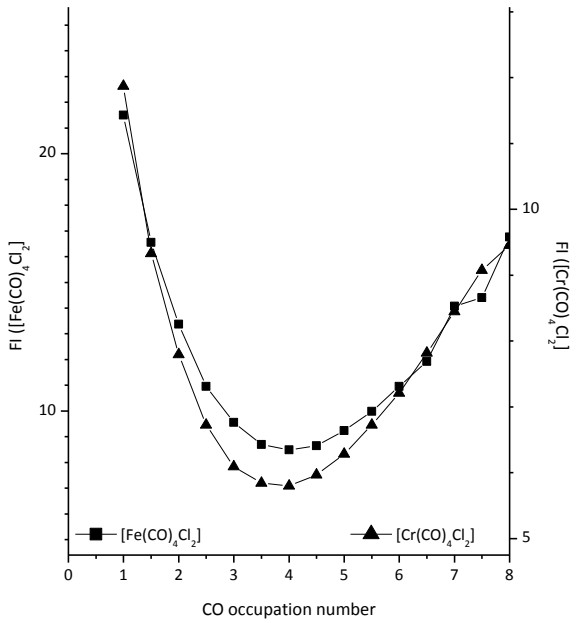

Figure 54. Plot of Fit Index (FI) *vs.* CO occupation number for *trans*-$[Fe(CO)_4Cl_2]$ and *trans*-$[Cr(CO)_4Cl_2]$ (data redrawn from I.R. Beattie, P.J. Jones, N.A. Young, J. Am. Chem. Soc., 114 (1992) 6146, [171]).

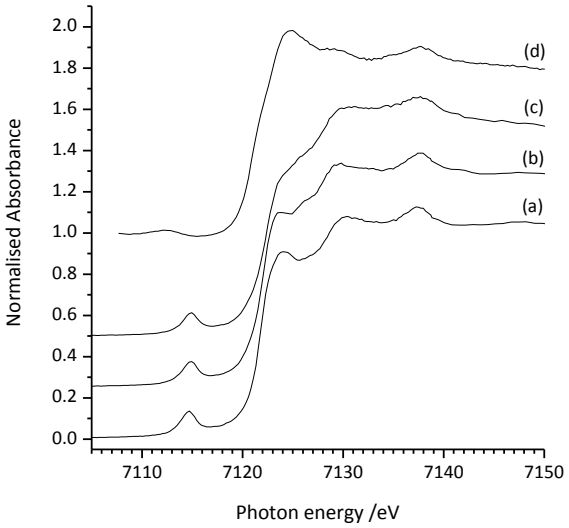

Figure 55. Fe K-edge XANES spectra of Fe_2Cl_6 vapour isolated in (a) solid N_2, (b) solid Ar, (c) solid Ne, (d) residual $FeCl_3$ solid after boiloff of matrix at end of experiment (data redrawn from N.A. Young, Jpn. J. Appl. Phys., 32 (1993) 776, [172]).

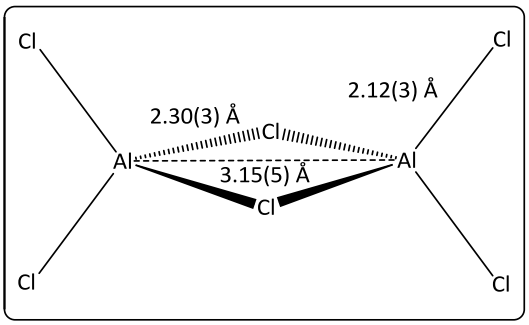

Figure 56. Summary of Fe K-edge EXAFS data for Fe_2Cl_6 isolated in solid N_2 (data from N.A. Young, Jpn. J. Appl. Phys., 32 (1993) 776, [172]).

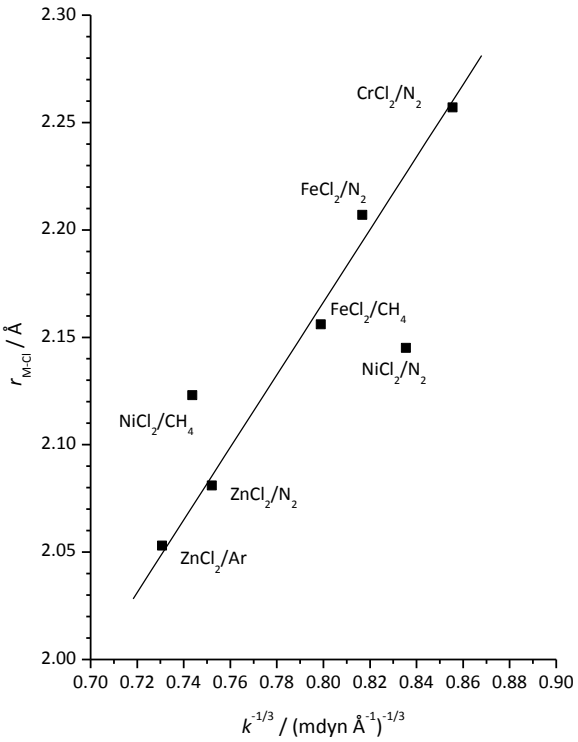

Figure 57. Badger's rule plot of EXAFS derived M-Cl bond length *vs.* $k^{-1/3}$ for first row transition metal dichlorides assuming linearity (data redrawn from I.R. Beattie, M.D. Spicer, N.A. Young, J. Chem. Phys., 100 (1994) 8700, [175]).

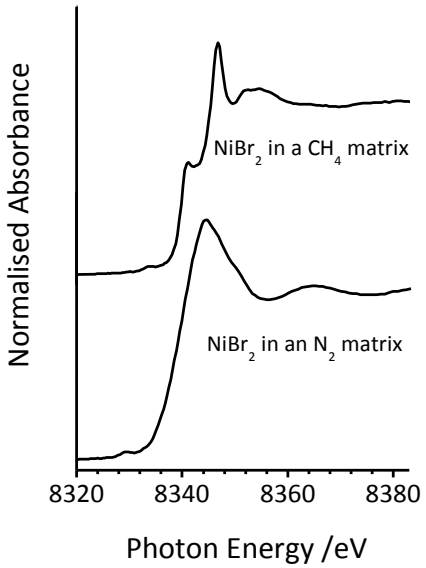

Figure 58. Ni K-edge XANES spectra of $NiBr_2$ trapped in solid methane and solid nitrogen at 10 K (data redrawn from N.A. Young, J. Chem. Soc., Dalton Trans., (1996) 249, [182]).

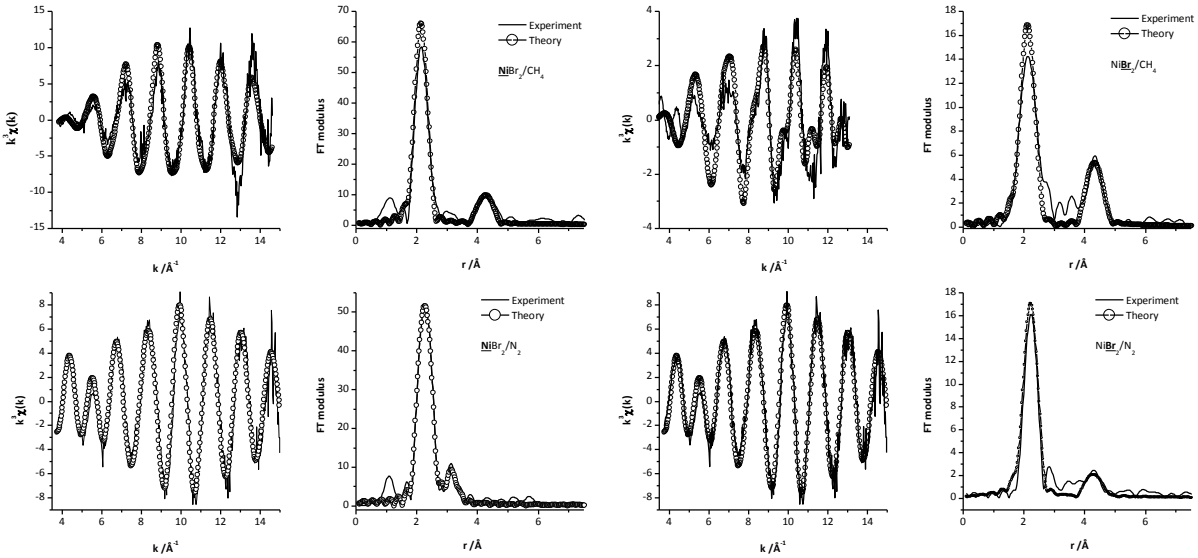

Figure 59. Ni K-edge EXAFS and FTs (left) and Br K-edge EXAFS and FTs (right) for $NiBr_2$ isolated in CH_4 matrices (top) and N_2 matrices (bottom) (data taken from N.A. Young, J. Chem. Soc., Dalton Trans., (1996) 249, [182] and re-analysed).

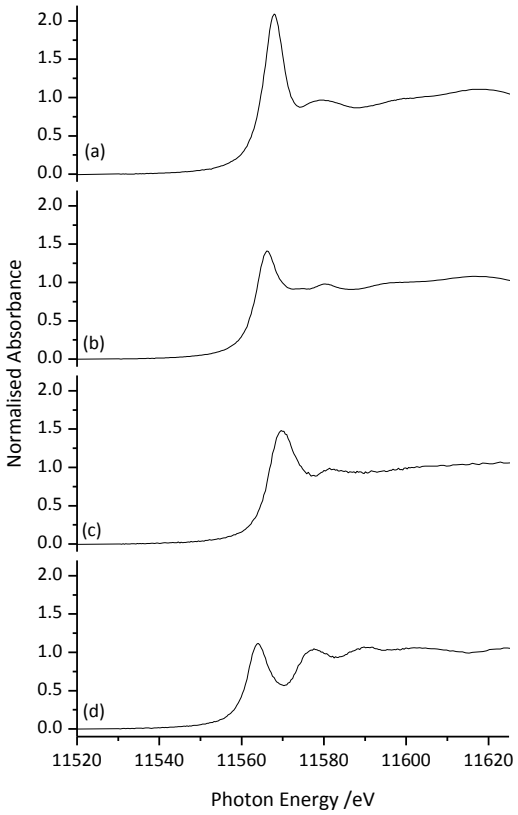

Figure 60. Pt L_3-edge XANES spectra for (a) K_2PtCl_6 diluted in BN at 298 K, (b) K_2PtCl_4 diluted in BN at 298 K, (c) matrix isolated products from a Pt hollow cathode sputtered with 5% Cl_2/Ar and (d) neat Ar (data redrawn from A.J. Bridgeman, G. Cavigliasso, N. Harris, N.A. Young, Chem. Phys. Lett., 351 (2002) 319, [194]).

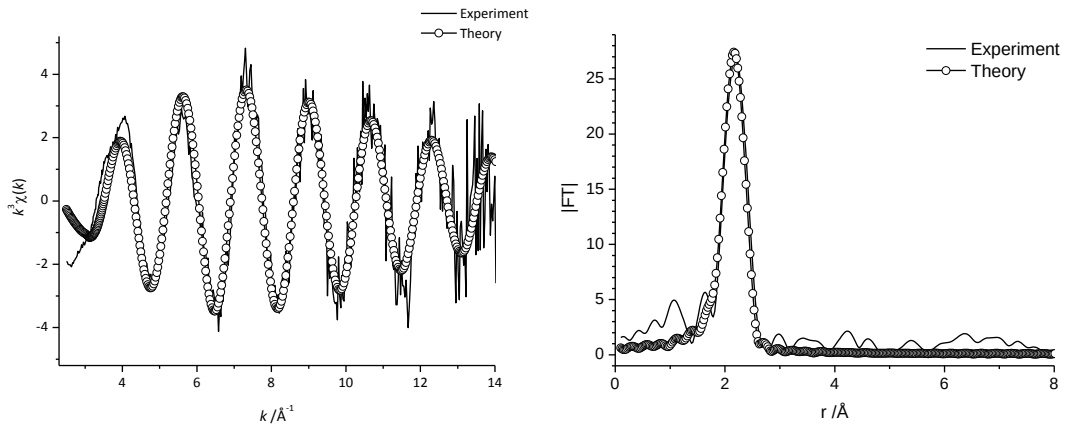

Figure 61. Au L_3 EXAFS (left) and FT (right) of matrix isolated products of gold atoms sputtered with 5% Cl_2/Ar (data redrawn from I.J. Blackmore, A.J. Bridgeman, N. Harris, M.A. Holdaway, J.F. Rooms, E.L. Thompson, N.A. Young, Angew. Chem. Int. Ed., 44 (2005) 6746, [23]).

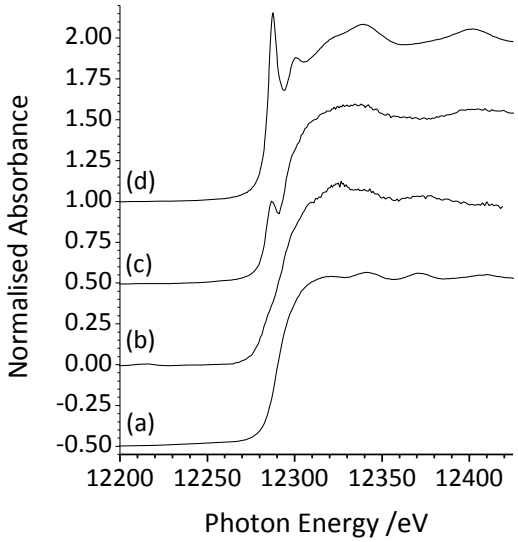

Figure 62. Hg L_3-edge XANES spectra of Hg atoms isolated in (a) 100% Ar matrix, (b) in 10% F_2/Ar matrix during deposition, (c) after broad band Hg photolysis, (d) Au L_3-edge XANES spectrum of $HAuCl_4$ at 298 K (energy scale shifted by 364 eV). (Data redrawn from J.F. Rooms, A.V. Wilson, I. Harvey, A.J. Bridgeman, N.A. Young, Phys. Chem. Chem. Phys., 10 (2008) 4594, [204]).

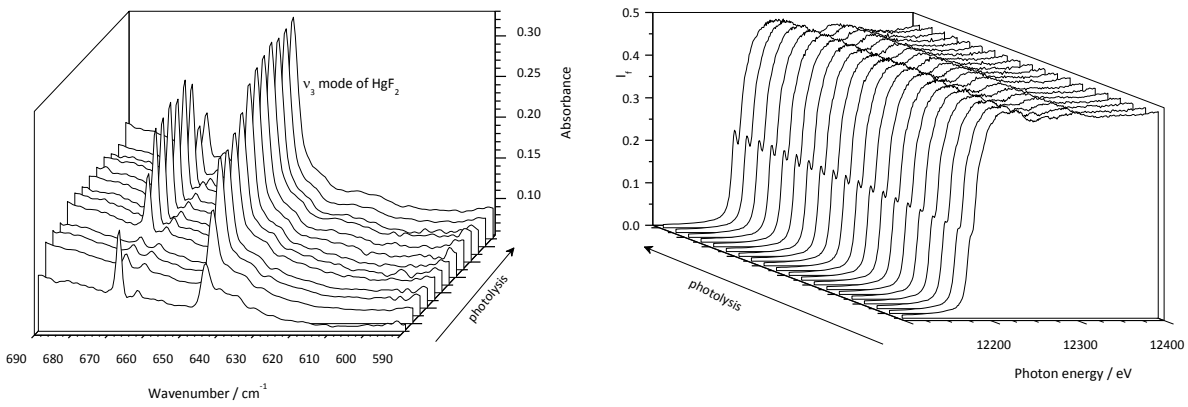

Figure 63. Simultaneous FTIR (left) and Hg L_3-edge XANES (right) spectra during photolysis of Hg atoms in a 10% F_2/Ar matrix at 14 K (data taken from J.F. Rooms, A.V. Wilson, I. Harvey, A.J. Bridgeman, N.A. Young, Phys. Chem. Chem. Phys., 10 (2008) 4594, [204]).

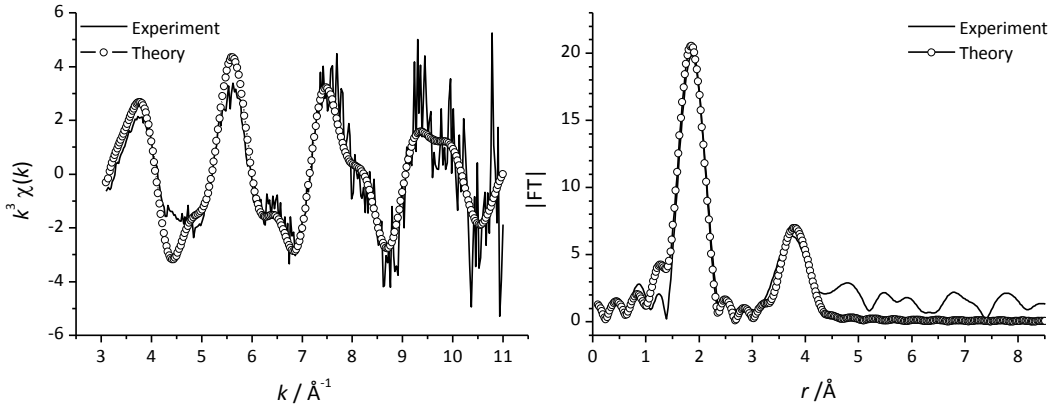

Figure 64. Hg L_3-edge EXAFS (left) and FT (right) of HgF_2 formed from Hg atoms in 10% F_2/Ar after broad band photolysis (data redrawn from J.F. Rooms, A.V. Wilson, I. Harvey, A.J. Bridgeman, N.A. Young, Phys. Chem. Chem. Phys., 10 (2008) 4594, [204]).

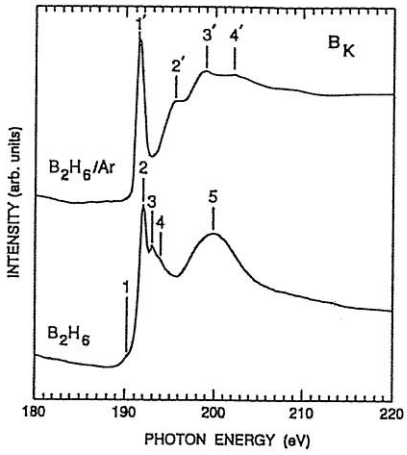

Figure 65. Boron K-edge spectra for diborane isolated in argon matrices at 15 K (top) and diborane condensed on graphite(bottom). (Reproduced with permission of Elsevier from M.W. Ruckman, M.F. Murray, J.K. Mowlem, J.F. Moore, D.R. Strongin, Chem. Phys. Lett., 198 (1992) 449, [209])

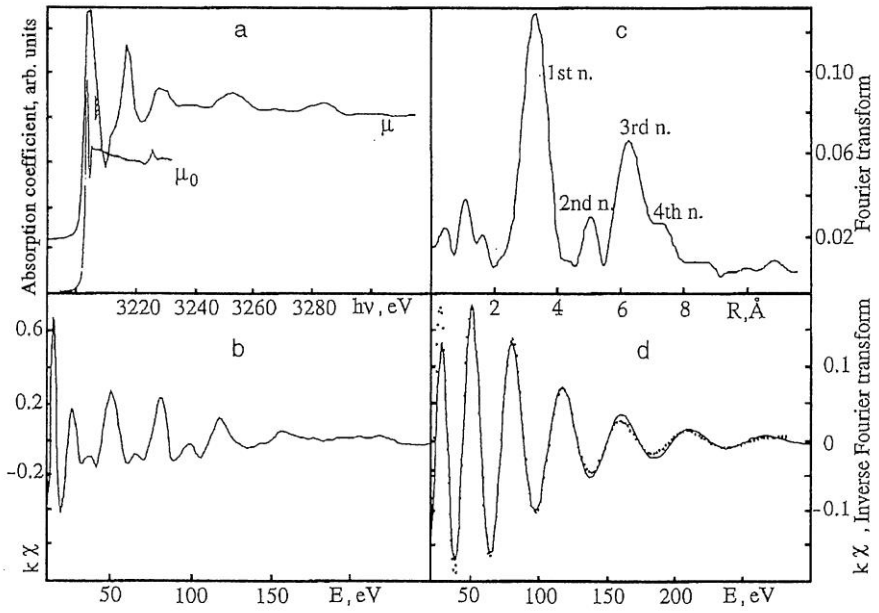

Figure 66. X-ray absorption data at the K-edge of solid argon. (a) Solid argon, (b) $k\chi(k)$ EXAFS, (c) FT of EXAFS, (d) back-transform of 1st shell (dots correspond to experiment, and continuous line is theoretical data. (Reproduced with permission from P. Roubin, S. Varin, C. Crépin, B. Gauthier-Roy, A.M. Flank, P. Lagarde, F. Ténégal, Low Temp. Phys., 26 (2000) 691 [231], copyright 2000, AIP Publishing LLC).

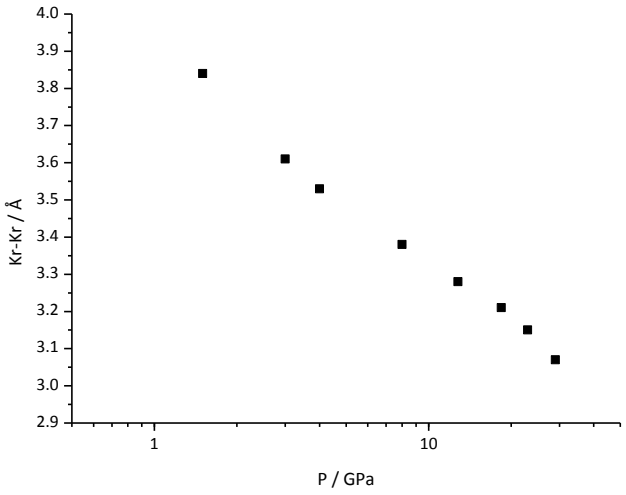

Figure 67. Plot of Kr-Kr nearest neighbour distances from Kr K-edge EXAFS data *vs.* pressure (data redrawn from A. Di Cicco, A. Filipponi, J.P. Itié, A. Polian, Phys. Rev. B, 54 (1996) 9086, [246]).

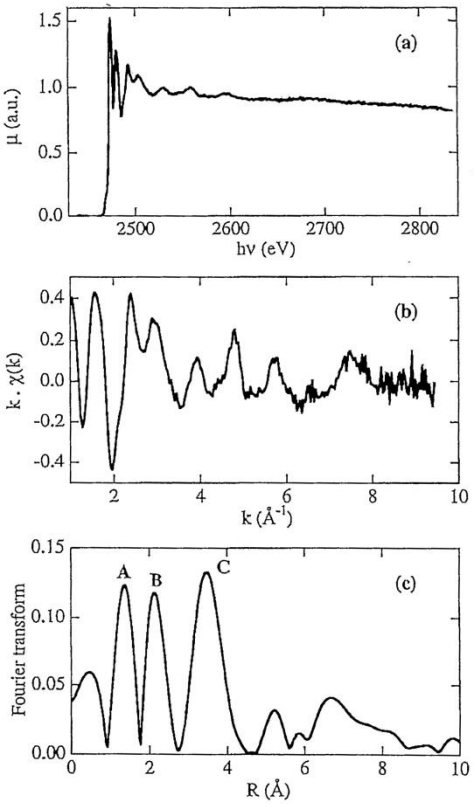

Figure 68. (a) S K-edge spectrum of OCS in an argon matrix, (b) EXAFS spectrum, (c) FT (reproduced with permission from P. Roubin, S. Varin, C. Crépin, B. Gauthier-Roy, A.M. Flank, R. Delaunay, M. Pompa, B. Tremblay, J. Chem. Phys., 109 (1998) 7945 [269], copyright 1998, AIP Publishing LLC).

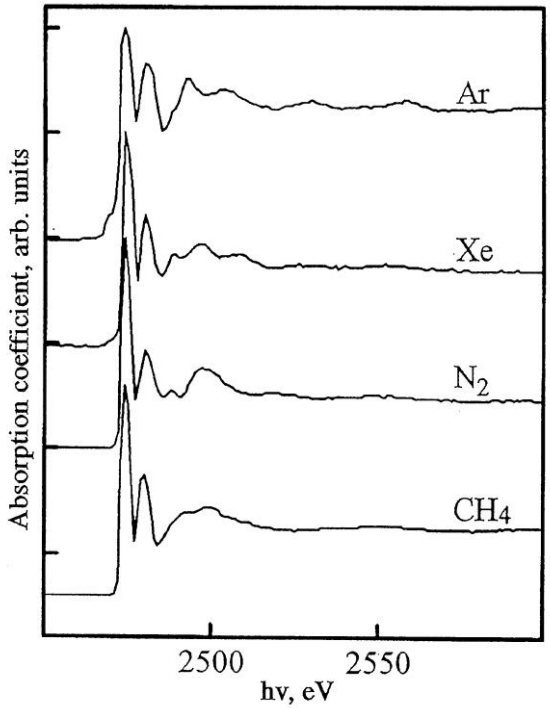

Figure 69. Sulfur K-edge X-ray absorption spectra for OCS isolated in Ar, Xe, N_2 and CH_4 matrices. (Reproduced with permission from P. Roubin, S. Varin, C. Crépin, B. Gauthier-Roy, A.M. Flank, P. Lagarde, F. Ténégal, Low Temp. Phys., 26 (2000) 691 [231], copyright 2000, AIP Publishing LLC).

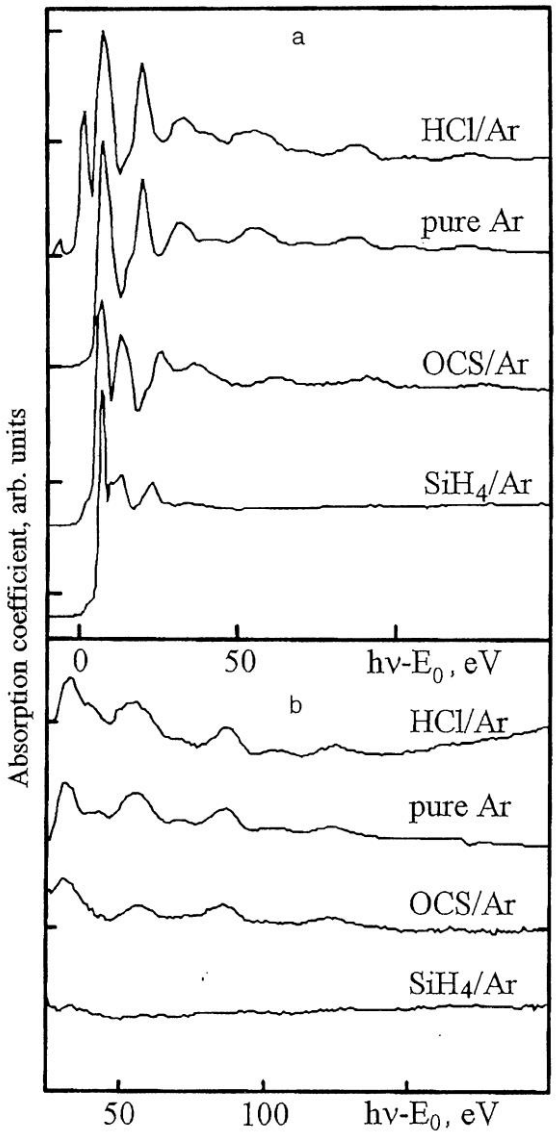

Figure 70. X-ray absorption spectra of HCl/Ar, pure Ar, OCS/Ar and SiH_4/Ar matrices. The absorption edges have been aligned. (Reproduced with permission from P. Roubin, S. Varin, C. Crépin, B. Gauthier-Roy, A.M. Flank, P. Lagarde, F. Ténégal, Low Temp. Phys., 26 (2000) 691 [231], copyright 2000, AIP Publishing LLC).

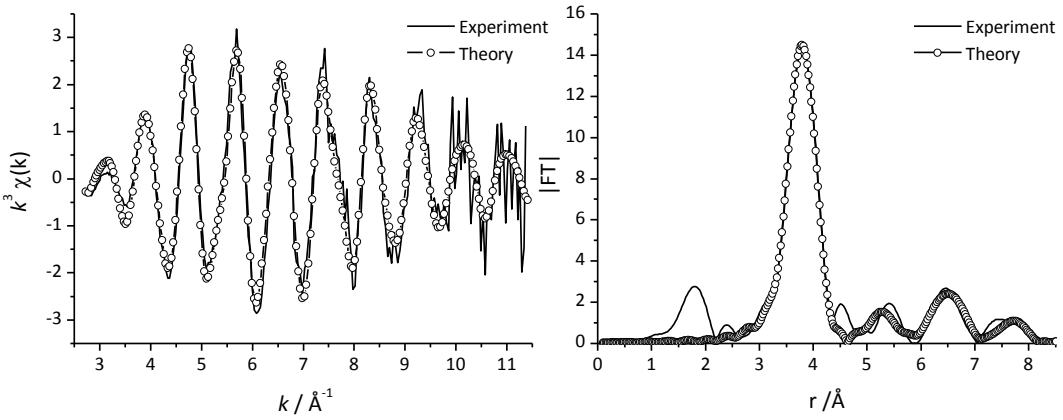

Figure 71. Hg L_3-edge EXAFS (left) and FT (right) of Hg atoms in an Ar matrix at 14 K (data redrawn from J.F. Rooms, A.V. Wilson, I. Harvey, A.J. Bridgeman, N.A. Young, Phys. Chem. Chem. Phys., 10 (2008) 4594, [204]).

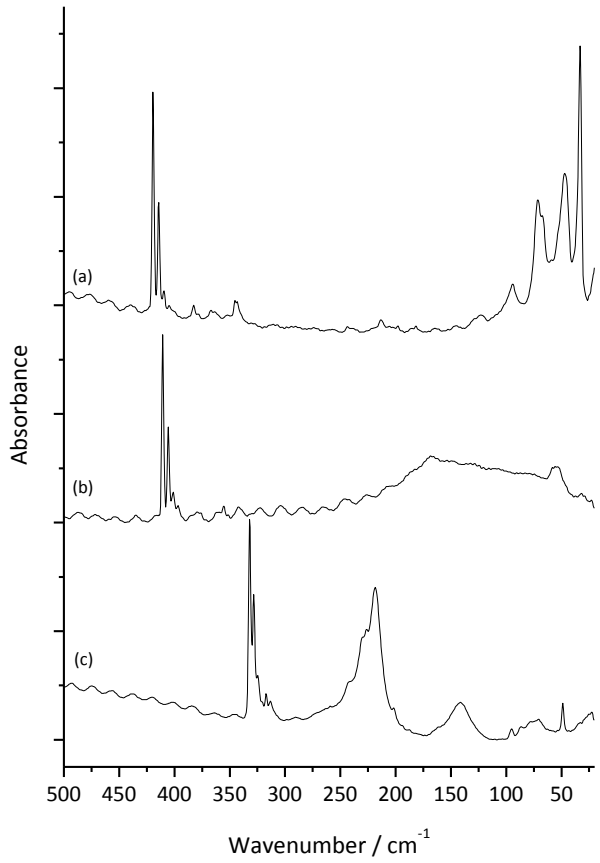

Figure 72. Synchrotron radiation far-IR spectra of $NiBr_2$ isolated in (a) Ar, (b) CH_4 and (c) N_2 matrices at 12 K.

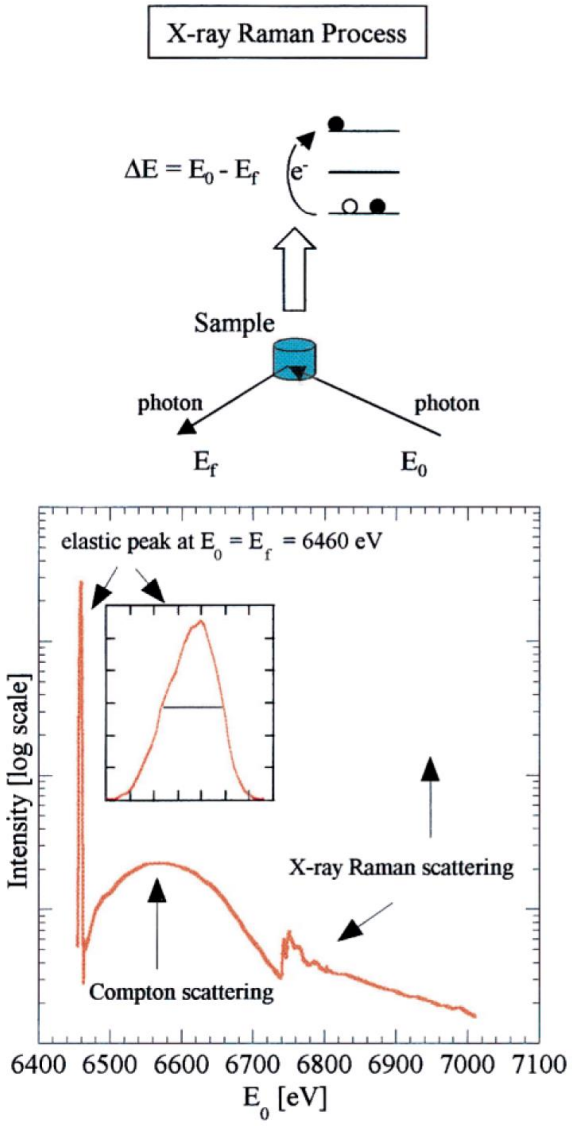

Figure 73. Schematic diagram of processes occurring in X-ray Raman spectroscopy. (Top) An X-ray photon with incident energy E_0 is inelastically scattered with final E_f, providing a fraction of its energy to excite a core electron into an empty bound or continuum state. (Bottom) Rayleigh (elastic), Compton and Raman scattering profiles from graphite (note log scale). (Reproduced with permission of Elsevier from U. Bergmann, P. Glatzel, S.P. Cramer, Microchem. J., 71 (2002) 221, [354].)

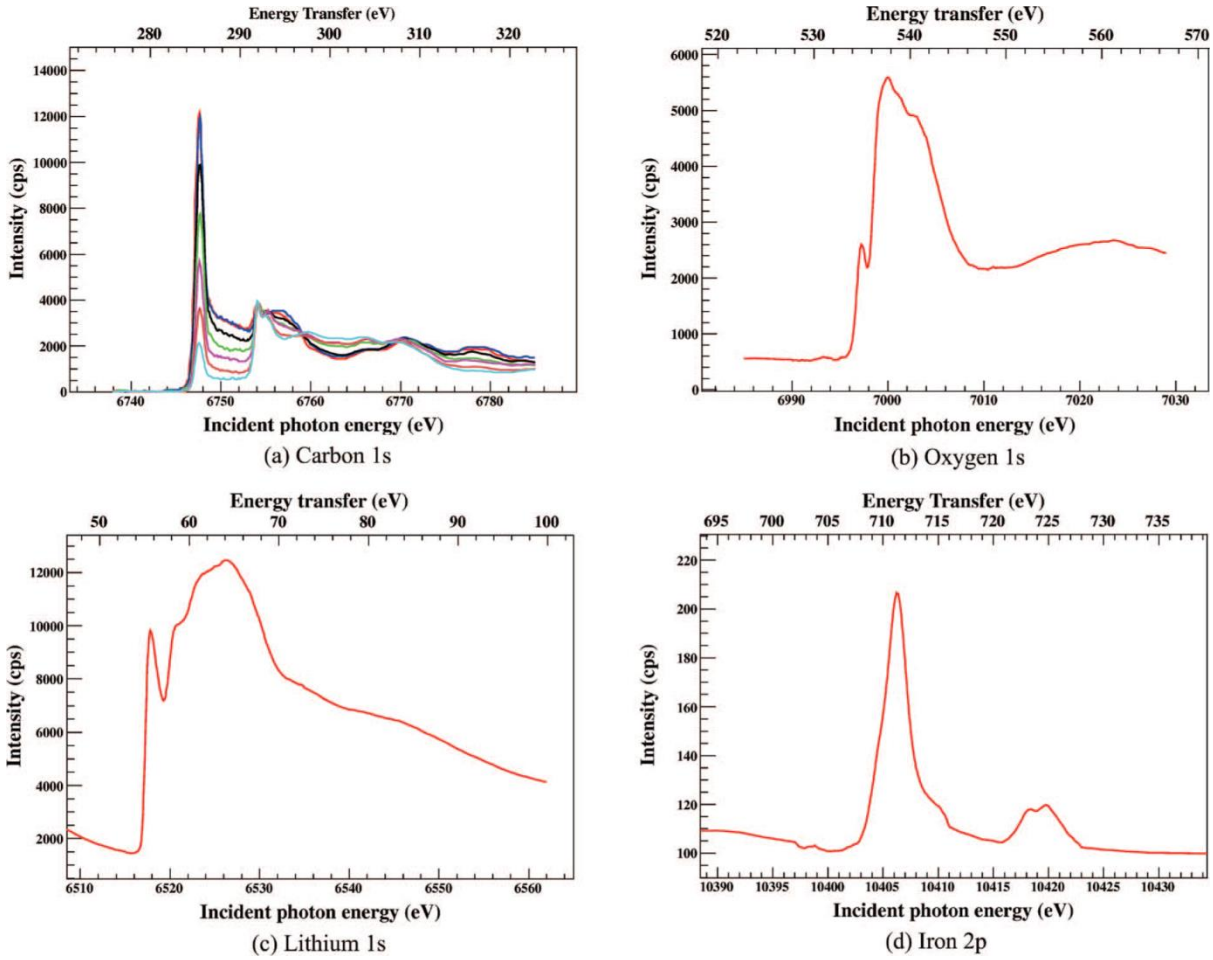

Figure 74. (a) Angular dependent carbon 1s X-ray Raman spectra from HPOG (Compton background contribution has been subtracted for ease of presentation). (Si(440) reflection). (b) X-ray Raman scattering of oxygen 1s electrons as measured on liquid water (Si(440) reflection). (c) Li metal 1s XRS raw spectrum (Si(440) reflection). (d) Fe-$L_{2,3}$ XRS from a $LiFePO_4$ battery cathode (Si(660) reflection). For all measurements the Si(311) monochromator was used for the incident energy . (Reproduced with permission from D. Sokaras, D. Nordlund, T.C. Weng, R.A. Mori, P. Velikov, D. Wenger, A. Garachtchenko, M. George, V. Borzenets, B. Johnson, Q. Qian, T. Rabedeau, U. Bergmann, Rev. Sci. Instrum., 83 (2012) 043112, [357], copyright 2012, AIP Publishing LLC.)

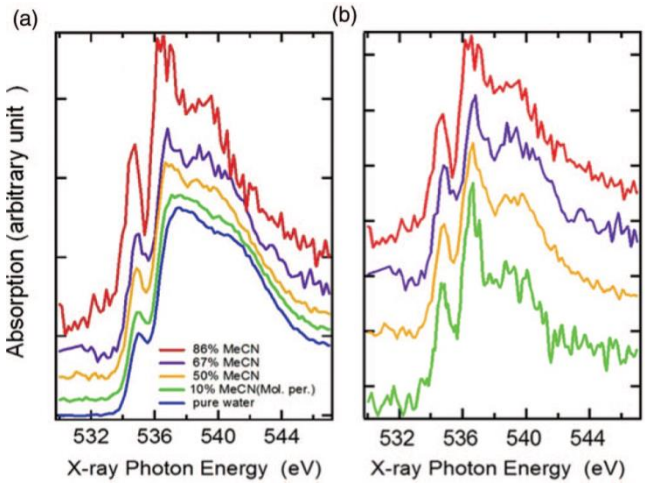

Figure 75. X-ray Raman scattering spectra of (a) aqueous MeCN solutions with concentration of MeCN increasing from bottom to top and (b) water interacting with MeCN obtained by subtracting the estimated pure water-like contribution to each spectrum. (Reproduced with permission from N. Huang, D. Nordlund, C. Huang, U. Bergmann, T.M. Weiss, L.G.M. Pettersson, A. Nilsson, J. Chem. Phys., 135 (2011) 164509, [374], copyright 2012, AIP Publishing LLC.).

14. **References**

[1] E. Whittle, D.A. Dows, G.C. Pimentel, J. Chem. Phys., 22 (1954) 1943.
[2] A.J. Downs, S.C. Peake, Matrix Isolation, in: Molecular Spectroscopy, The Chemical Society, London, 1973, pp. 523.
[3] B.M. Chadwick, Matrix isolation, in: Molecular Spectroscopy, The Chemical Society, London, 1975, pp. 281.
[4] B.M. Chadwick, Matrix Isolation, in: Molecular Spectroscopy, The Chemical Society, London, 1979, pp. 72.
[5] D.W. Ball, Z.H. Kafafi, L. Fredin, R.H. Hauge, J.L. Margrave, A Bibliography of Matrix Isolation Spectroscopy: 1954 - 1985, Rice University Press, Houston, 1988.
[6] D.W. Ochsner, D.W. Ball, Z.A. Kafafi, A Bibliography of Matrix Isolation Spectroscopy:1985-1997, Naval Research Laboratory, Washington, DC, 1998.
[7] M.J. Almond, A.J. Downs, in: R.J.H. Clark, R.E. Hester (Eds.) Advances in Spectroscopy: Spectroscopy of matrix isolated species, John Wiley, Chichester, 1989.
[8] M.J. Almond, R.H. Orrin, Annu. Rep. Prog. Chem., Sect. C, Phys. Chem., 88 (1991) 3.
[9] M.J. Almond, Annu. Rep. Prog. Chem., Sect. C, Phys. Chem., 93 (1997) 3.
[10] M.J. Almond, K.S. Wiltshire, Annu. Rep. Prog. Chem., Sect. C, Phys. Chem., 97 (2001) 3.
[11] M.J. Almond, N. Goldberg, Annu. Rep. Prog. Chem., Sect. C, Phys. Chem., 103 (2007) 79.
[12] H.E. Hallam, Vibrational Spectroscopy of Trapped Species, John Wiley & Sons, London, 1973.
[13] S. Craddock, A.J. Hinchcliffe, Matrix Isolation, Cambridge University Press, Cambridge, 1975.
[14] M. Moskovits, G.A. Ozin, Cryochemistry, Wiley-Interscience, New York, 1976.
[15] M. Moskovits, L. Andrews, Chemistry and Physics of Matrix Isolated Species, Elsevier, Amsterdam, 1989.
[16] I.R. Dunkin, Matrix-Isolation Techniques: A Practical Approach, Oxford University Press, Oxford, 1998.
[17] L. Khriachtchev, Physics and Chemistry at Low Temperatures, Pan Stanford Publishing, Singapore, 2011.
[18] F. Stienkemeier, A.F. Vilesov, J. Chem. Phys., 115 (2001) 10119.
[19] J.P. Toennies, A.F. Vilesov, Angew. Chem. Int. Ed., 43 (2004) 2622.
[20] S. Kuma, M.N. Slipchenko, K.E. Kuyanov, T. Momose, A.F. Vilesov, J. Phys. Chem. A, 110 (2006) 10046.
[21] S. Kuma, M.N. Slipchenko, T. Momose, A.F. Vilesov, Chem. Phys. Lett., 439 (2007) 265.
[22] K. Kuyanov-Prozument, D. Skvortsov, M.N. Slipchenko, B.G. Sartakov, A. Vilesov, Matrix isolation spectroscopy in helium droplets, in: L. Khriachtchev (Ed.) Chemistry and Physics at Low Temperatures, Pan Stanford Publishing, Singapore, 2011, pp. 203.
[23] I.J. Blackmore, A.J. Bridgeman, N. Harris, M.A. Holdaway, J.F. Rooms, E.L. Thompson, N.A. Young, Angew. Chem. Int. Ed., 44 (2005) 6746.
[24] K.W. Zilm, R.T. Conlin, D.M. Grant, J. Michl, J. Am. Chem. Soc., 100 (1978) 8038.
[25] J.E. Kohl, M.G. Semack, D. White, J. Chem. Phys., 69 (1978) 5378.
[26] M.S. Conradi, K. Luszczynski, R.E. Norberg, Phys. Rev. B, 20 (1979) 2594.
[27] C.S. Yannoni, H.P. Reisenauer, G. Maier, J. Am. Chem. Soc., 105 (1983) 6181.

[28] K.W. Zilm, R.A. Merrill, M.M. Greenberg, J.A. Berson, J. Am. Chem. Soc., 109 (1987) 1567.
[29] J.E. Espidel, R.K. Harris, Magn. Reson. Chem., 28 (1990) S15.
[30] J.A. Hamida, N.S. Sullivan, M.D. Evans, Phys. Rev. Lett., 73 (1994) 2720.
[31] J.A. Hamida, E.B. Genio, N.S. Sullivan, Czech J. Phys., 46 (1996) 513.
[32] J.A. Hamida, E.B. Genio, N.S. Sullivan, J. Low Temp. Phys., 103 (1996) 49.
[33] J.A. Hamida, S. Pilla, N.S. Sullivan, J. Low Temp. Phys., 111 (1998) 365.
[34] K.W. Zilm, A.J. Beeler, D.M. Grant, J. Michl, T.C. Chou, E.L. Allred, J. Am. Chem. Soc., 103 (1981) 2119.
[35] K.W. Zilm, D.M. Grant, J. Am. Chem. Soc., 103 (1981) 2913.
[36] A.M. Orendt, J.C. Facelli, J.G. Radziszewski, W.J. Horton, D.M. Grant, J. Michl, J. Am. Chem. Soc., 118 (1996) 846.
[37] D.G. Henshaw, Phys. Rev., 111 (1958) 1470.
[38] C.S. Barrett, L. Meyer, J. Chem. Phys., 41 (1964) 1078.
[39] G.K. Horton, Am. J. Phys., 36 (1968) 93.
[40] J. Hingsammer, E. Lüscher, Helv. Phys. Acta, 41 (1968) 914.
[41] G.W. Stinton, I. Loa, L.F. Lundegaard, M.I. McMahon, J. Chem. Phys., 131 (2009) 104511.
[42] W. Langel, H. Kollhoff, E. Knözinger, J. Phys. E Sci. Instrum., 19 (1986) 86.
[43] W. Langel, H. Kollhoff, E. Knözinger, M. Prager, Ber. Bunsenges. Phys. Chem., 91 (1987) 1257.
[44] E. Knözinger, W. Schuller, W. Langel, Farad. Discus. Chem. Soc., 86 (1988) 285.
[45] W. Langel, W. Schuller, E. Knözinger, H.W. Fleger, H.J. Lauter, J. Chem. Phys., 89 (1988) 1741.
[46] H.J. Deiseroth, S. Popp, H. Kollhoff, W. Langel, E. Knözinger, J. Mol. Struct., 174 (1988) 89.
[47] W. Langel, M. Prager, H.W. Fleger, E. Knözinger, H.J. Lauter, H. Blank, C.J. Carlile, J. Chem. Phys., 98 (1993) 4838.
[48] A. Becker, W. Langel, S. Maass, E. Knoezinger, J. Phys. Chem., 97 (1993) 5525.
[49] W. Langel, A. Becker, H.W. Fleger, E. Knözinger, J. Mol. Struct., 297 (1993) 407.
[50] W. Langel, H.W. Fleger, E. Knözinger, Ber. Bunsenges. Phys. Chem., 98 (1994) 81.
[51] W. Langel, H.W. Fleger, E. Knözinger, W. Schuller, Ber. Bunsenges. Phys. Chem., 99 (1995) 940.
[52] E. Knözinger, E. Babka, D. Hallamasek, J. Phys. Chem. A, 105 (2001) 8176.
[53] J.Z. Larese, Q.M. Zhang, L. Passell, J.M. Hastings, J.R. Dennison, H. Taub, Phys. Rev. B, 40 (1989) 4271.
[54] W. Langel, Spectrochim. Acta A, 48 (1992) 405.
[55] J. Farges, M.F. de Feraudy, B. Raoult, G. Torchet, J. Chem. Phys., 78 (1983) 5067.
[56] J. Farges, M.F. de Feraudy, B. Raoult, G. Torchet, J. Chem. Phys., 84 (1986) 3491.
[57] S. DeBeer George, T. Petrenko, F. Neese, J. Phys. Chem. A, 112 (2008) 12936.
[58] N. Lee, T. Petrenko, U. Bergmann, F. Neese, S. DeBeer, J. Am. Chem. Soc., 132 (2010) 9715.
[59] P. Chandrasekaran, S.C.E. Stieber, T.J. Collins, L. Que, F. Neese, S. DeBeer, Dalton Trans., 40 (2011) 11070.
[60] M.A. Beckwith, M. Roemelt, M.N. Collomb, C. DuBoc, T.C. Weng, U. Bergmann, P. Glatzel, F. Neese, S. DeBeer, Inorg. Chem., 50 (2011) 8397.
[61] M. Roemelt, M.A. Beckwith, C. Duboc, M.N. Collomb, F. Neese, S. DeBeer, Inorg. Chem., 51 (2012) 680.
[62] C.C. Scarborough, S. Sproules, C.J. Doonan, K.S. Hagen, T. Weyhermuller, K. Wieghardt, Inorg. Chem., 51 (2012) 6969.

[63] C.C. Scarborough, K.M. Lancaster, S. DeBeer, T. Weyhermueller, S. Sproules, K. Wieghardt, Inorg. Chem., 51 (2012) 3718.
[64] TD-DFT XANES calculations were carried out with ORCA using the BP86 exchange-correlation functional and ZORA relativistic corrections, with the modified Ahlrichs Def2 TZVP(-f) basis set.
[65] A.D.J. Barnes, T. Baikie, V. Hardy, M.B. Lepetit, A. Maignan, N.A. Young, M.G. Francesconi, J. Mater. Chem., 16 (2006) 3489.
[66] G.J. Colpas, M.J. Maroney, C. Bagyinka, M. Kumar, W.S. Willis, S.L. Suib, N. Baidya, P.K. Mascharak, Inorg. Chem., 30 (1991) 920.
[67] D. Collison, C.D. Garner, C.M. McGrath, J.F.W. Mosselmans, M.D. Roper, J.M.W. Seddon, E. Sinn, N.A. Young, J. Synchrotron Rad., 6 (1999) 585.
[68] K. Fauth, S. Gold, M. Hessler, N. Schneider, G. Schütz, Chem. Phys. Lett., 392 (2004) 498.
[69] V.L. Mazalova, A.V. Soldatov, S. Adam, A. Yakovlev, T. Möller, R.L. Johnston, J. Phys. Chem. C, 113 (2009) 9086.
[70] I. Josefsson, K. Kunnus, S. Schreck, A. Föhlisch, F. de Groot, P. Wernet, M. Odelius, J. Phys. Chem. Lett., 3 (2012) 3565.
[71] D. Maganas, M. Roemelt, T. Weyhermüller, R. Blume, M. Hävecker, A. Knop-Gericke, S. DeBeer, R. Schlögl, F. Neese, Phys. Chem. Chem. Phys., 16 (2014) 264.
[72] B. Hedman, K.O. Hodgson, E.I. Solomon, J. Am. Chem. Soc., 112 (1990) 1643.
[73] T.A. Smith, J.G. Dewitt, B. Hedman, K.O. Hodgson, J. Am. Chem. Soc., 116 (1994) 3836.
[74] S.E. Shadle, B. Hedman, K.O. Hodgson, E.I. Solomon, J. Am. Chem. Soc., 117 (1995) 2259.
[75] A. Rompel, J.C. Andrews, R.M. Cinco, M.W. Wemple, G. Christou, N.A. Law, V.L. Pecoraro, K. Sauer, V.K. Yachandra, M.P. Klein, J. Am. Chem. Soc., 119 (1997) 4465.
[76] K.R. Williams, B. Hedman, K.O. Hodgson, E.I. Solomon, Inorg. Chim. Acta, 263 (1997) 315.
[77] T. Glaser, K. Rose, S.E. Shadle, B. Hedman, K.O. Hodgson, E.I. Solomon, J. Am. Chem. Soc., 123 (2001) 442.
[78] E.I. Solomon, B. Hedman, K.O. Hodgson, A. Dey, R.K. Szilagyi, Coord. Chem. Rev., 249 (2005) 97.
[79] S.A. Kozimor, P. Yang, E.R. Batista, K.S. Boland, C.J. Burns, D.L. Clark, S.D. Conradson, R.L. Martin, M.P. Wilkerson, L.E. Wolfsberg, J. Am. Chem. Soc., 131 (2009) 12125.
[80] M.S. Queen, B.D. Towey, K.A. Murray, B.S. Veldkamp, H.J. Byker, R.K. Szilagyi, Coord. Chem. Rev., 257 (2013) 564.
[81] I.R. Beattie, N. Binsted, W. Levason, J.S. Ogden, M.D. Spicer, N.A. Young, High Temp. Sci., 26 (1989) 71.
[82] A.V. Sapelkin, S.C. Bayliss, High Press. Res., 21 (2002) 315.
[83] A.V. Sapelkin, 2014, Personal Communication.
[84] A.C. Thompson, D. Vaughan, D.T. Attwood, E.M. Gullikson, M.R. Howells, J.B. Kortright, A.L. Robinson, J.H. Underwood, K.J. Kim, J. Kirz, I. Lindau, P. Pianetta, H. Winick, G.P. Williams, J.H. Scofield, Center for X-ray Optics and Advanced Light Source X-ray Data Booklet, 2nd ed., Lawrence Berkeley National Laboratory, University of California, Berkeley, California, USA, 2001.
[85] M.D. Spicer, N.A. Young, J. Chem. Soc., Dalton Trans., (1991) 3133.
[86] C.J. Marsden, L. Hedberg, K. Hedberg, Inorg. Chem., 21 (1982) 1115.
[87] B. Beagley, D.W.J. Cruickshank, P.M. Pinder, A.G. Robiette, G.M. Sheldrick, Acta. Crystallogr. B, 25 (1969) 737.

[88] B. Beagley, D.G. Schmidling, J. Mol. Struct., 22 (1974) 466.
[89] D. Braga, F. Grepioni, A.G. Orpen, Organometallics, 12 (1993) 1481.
[90] A. van der Gaauw, O.M. Wilkin, N.A. Young, J. Chem. Soc., Dalton Trans., (1999) 2405.
[91] N. Binsted, A. van der Gaauw, O.M. Wilkin, N.A. Young, J. Synch. Rad., 6 (1999) 239.
[92] N. Binsted, M.J. Pack, M.T. Weller, J. Evans, J. Am. Chem. Soc., 118 (1996) 10200.
[93] C.M. McGrath, C.J. O'Connor, C. Sangregorio, J.M.W. Seddon, E. Sinn, F.E. Sowrey, N.A. Young, Inorg. Chem. Comm., 2 (1999) 536.
[94] G. Smolentsev, A.V. Soldatov, M.C. Feiters, Phys. Rev. B, 75 (2007) 144106.
[95] G. Smolentsev, A.V. Soldatov, L.X. Chen, J. Phys. Chem. A, 112 (2008) 5363.
[96] K.C. Cheung, R.W. Strange, S.S. Hasnain, Acta Cryst. D, 56 (2000) 697.
[97] J.J. Rehr, J.J. Kas, F.D. Vila, M.P. Prange, K. Jorissen, Phys. Chem. Chem. Phys., 12 (2010) 5503.
[98] B. Ravel, M. Newville, J. Synchrotron Rad., 12 (2005) 537.
[99] N. Binsted, 1998, EXCURV98, CCLRC Daresbury Laboratory Computer Program
[100] T.E. Westre, A. Di Cicco, A. Filipponi, C.R. Natoli, B. Hedman, E.I. Solomon, K.O. Hodgson, J. Am. Chem. Soc., 117 (1995) 1566.
[101] O. Bunau, Y. Joly, J. Phys. Conds. Mat., 21 (2009) 345501.
[102] N.A. Young, M.D. Spicer, J. Mol. Struct., 222 (1990) 77.
[103] O.M. Wilkin, N.A. Young, J. Synch. Rad., 6 (1999) 204.
[104] L. Bencivenni, L. Dalessio, S.N. Cesaro, M. Maltese, M. Spoliti, High Temp. Sci., 11 (1979) 171.
[105] S.A. Arthers, I.R. Beattie, R.A. Gomme, P.J. Jones, J.S. Ogden, J. Chem. Soc., Dalton Trans., (1983) 1461.
[106] L. Bencivenni, H.M. Nagarathna, K.A. Gingerich, Chem. Phys. Lett., 99 (1983) 258.
[107] L. Bencivenni, H.M. Nagarathna, D.W. Wilhite, K.A. Gingerich, Inorg. Chem., 23 (1984) 1279.
[108] V.P. Spiridonov, A.N. Khodchenkov, P.A. Akishin, Vestn. Mosk. Univ., Ser. 2: Khim., 20 (1965) 34.
[109] K.P. Petrov, V.V. Ugarov, N.G. Rambidi, Zh. Strukt. Khim., 21 (1980) 189.
[110] N.M. Roddatis, S.M. Tolmachev, V.V. Ugarov, N.G. Rambidi, Zh. Strukt. Khim., 15 (1974) 693.
[111] P.A. Montano, J. Zhao, M. Ramanathan, G.K. Shenoy, W. Schulze, J. Urban, Chem. Phys. Lett., 164 (1989) 126.
[112] E. Roduner, Chem. Soc. Rev., 35 (2006) 583.
[113] S. Peters, S. Peredkov, B. Balkaya, N. Ferretti, A. Savci, A. Vollmer, M. Neeb, W. Eberhardt, Rev. Sci. Instrum., 80 (2009) 125106.
[114] R.C. Baetzold, J.F. Hamilton, Prog. Solid State Chem., 15 (1983) 1.
[115] G.A. Ozin, S.A. Mitchell, Angew. Chem. Int Ed. Engl., 22 (1983) 674.
[116] P.A. Montano, G.K. Shenoy, S. Ruby, Bull. Amer. Phys. Soc., 24 (1979) 505.
[117] P.A. Montano, Shenoy, G. K., Solid State Commun., 35 (1980) 53.
[118] H. Purdum, P.A. Montano, G.K. Shenoy, T. Morrison, Phys. Rev. B, 25 (1982) 4412.
[119] G. Apai, J.F. Hamilton, J. Stohr, A. Thompson, Phys. Rev. Lett., 43 (1979) 165.
[120] P.A. Montano, G.K. Shenoy, T.I. Morrison, W. Schulze, Springer Proc. Phys., 2 (1984) 231.
[121] P.A. Montano, H. Purdum, G.K. Shenoy, T.I. Morrison, W. Schulze, Surf. Sci., 156 (1985) 228.
[122] P.A. Montano, J. Zhao, M. Ramanathan, G.K. Shenoy, W. Schulze, Physica B, 158 (1989) 242.

[123] P.A. Montano, J. Zhao, M. Ramanathan, G.K. Shenoy, W. Schulze, Z. Phys. D, 12 (1989) 103.
[124] J. Zhao, M. Ramanathan, P.A. Montano, G.K. Shenoy, W. Schulze, Mater. Res. Soc. Symp. Proc., 143 (1989) 151.
[125] P.A. Montano, Y. Cao, J. Phys. Conds. Mat., 5 (1993) A209.
[126] P.A. Montano, G.K. Shenoy, E.E. Alp, W. Schulze, J. Urban, Phys. Rev. Lett., 56 (1986) 2076.
[127] J. Zhao, P.A. Montano, Phys. Rev. B, 40 (1989) 3401.
[128] J.L. Jules, J.R. Lombardi, J. Phys. Chem. A, 107 (2003) 1268.
[129] O. Hübner, J. Sauer, Chem. Phys. Lett., 358 (2002) 442.
[130] C.W. Bauschlicher, A. Ricca, Mol. Phys., 101 (2003) 93.
[131] C. Angeli, R. Cimiraglia, Mol. Phys., 109 (2011) 1503.
[132] Q. Sun, Z. Li, A. Du, J. Chen, Z. Zhu, S.C. Smith, Fuel, 96 (2012) 291.
[133] G.L. Gutsev, C.A. Weatherford, P. Jena, E. Johnson, B.R. Ramachandran, J. Phys. Chem. A, 116 (2012) 10218.
[134] P.G. Alvarado-Leyva, F. Aguilera-Granja, L.C. Balbás, A. Vega, Phys. Chem. Chem. Phys., 15 (2013) 14458.
[135] M. Casula, M. Marchi, S. Azadi, S. Sorella, Chem. Phys. Lett., 477 (2009) 255.
[136] M. Samah, B. Moula, Rev. Mex. Fis., 57 (2011) 166.
[137] K. Cervantes-Salguero, J.M. Seminario, J. Mol. Model., 18 (2012) 4043.
[138] P.A. Montano, W. Schulze, B. Tesche, G.K. Shenoy, T.I. Morrison, Phys. Rev. B, 30 (1984) 672.
[139] H.J. Wasserman, J.S. Vermaak, Surf. Sci., 22 (1970) 164.
[140] B. Simard, P.A. Hackett, A.M. James, P.R.R. Langridge-Smith, Chem. Phys. Lett., 186 (1991) 415.
[141] K. Heinemann, H. Poppa, Surf. Sci., 156(1) (1985) 265.
[142] J.S. Ogden, N.E. Bogdanchikova, J.M. Corker, V.P. Petranovskii, Eur. Phys. J. D, 9 (1999) 605.
[143] N. Ashlund, R.F. Barrow, W.G. Richards, D.N. Travis, Ark. Fys., 30 (1965) 171.
[144] R.S. Ram, C.N. Jarman, P.F. Bernath, J. Mol. Spectrosc., 156 (1992) 468.
[145] M.A. Marcus, V.E. Lamberti, M.F. Andrews, Physica B, 158 (1989) 34.
[146] D.L. Michalopoulos, M.E. Geusic, S.G. Hansen, D.E. Powers, R.E. Smalley, J. Phys. Chem., 86 (1982) 3914.
[147] V.E. Bondybey, J.H. English, Chem. Phys. Lett., 94 (1983) 443.
[148] A.M. Flank, R.C. Karnatak, C. Blancard, J.M. Esteva, P. Lagarde, J.P. Connerade, Z. Phys. D, 21 (1991) 357.
[149] E. Bouisset, J.M. Esteva, R.C. Karnatak, J.P. Connerade, A.M. Flank, P. Lagarde, J. Phys. B: At., Mol. Opt. Phys., 24 (1991) 1609.
[150] J.S. Anderson, J.S. Ogden, M.J. Ricks, J. Chem. Soc., Chem. Commun., (1968) 1585.
[151] J.S. Anderson, J.S. Ogden, J. Chem. Phys., 51 (1969) 4189.
[152] L.C. Snyder, K. Raghavachari, J. Chem. Phys., 80 (1984) 5076.
[153] A. Barranco, F. Yubero, J.P. Espinos, P. Groening, A.R. Gonzalez-Elipe, J. Appl. Phys., 97 (2005) 113714.
[154] G. Materlik, B. Sonntag, M. Tausch, Phys. Rev. Lett., 51 (1983) 1300.
[155] M. Lübcke, B. Sonntag, W. Niemann, P. Rabe, Phys. Rev. B, 34 (1986) 5184.
[156] W. Niemann, M. Lübcke, W. Malzfeldt, P. Rabe, R. Haensel, J. Magn. Magn. Mater., 47-8 (1985) 462.
[157] W. Niemann, W. Malzfeldt, P. Rabe, M. Lübcke, J. Physiq., C8 (1986) 931.
[158] W. Niemann, W. Malzfeldt, P. Rabe, R. Haensel, M. Lübcke, Phys. Rev. B, 35 (1987) 1099.

[159] C. Blancard, J.M. Esteva, R.C. Karnatak, J.P. Connerade, U. Kuetgens, J. Hormes, J. Phys. B At. Mol. Opt. Phys., 22 (1989) L575.
[160] J.P. Connerade, R.C. Karnatak, Comments At. Mol. Phys., 24 (1990) 1.
[161] C. Bréchignac, J.P. Connerade, J. Phys. B At. Mol. Opt. Phys., 27 (1994) 3795.
[162] A. Elafif, R.C. Karnatak, J.M. Esteva, C.M. Teodorescu, M. Womes, E. Bouisset, Physica B, 208 & 209 (1995) 115.
[163] C.M. Teodorescu, A. El Afif, J.M. Esteva, R.C. Karnatak, Phys. Rev. B, 63 (2001) 233106.
[164] C.M. Teodorescu, M. Womes, A. El Afif, R.C. Karnatak, J.M. Esteva, A.M. Flank, P. Lagarde, J. Electron Spectrosc. Relat. Phenom., 103 (1999) 205.
[165] C.M. Teodorescu, J.M. Esteva, M. Womes, A. El Afif, R.C. Karnatak, A.M. Flank, P. Lagarde, J. Electron Spectrosc. Relat. Phenom., 106 (2000) 233.
[166] M. Riedler, A.R.B. de Castro, A. Kolmakov, J.O. Löfken, C. Nowak, A.V. Soldatov, A. Wark, G. Yalovega, T. Möller, Phys. Rev. B, 64 (2001) 245419.
[167] M. Riedler, A.R.B. de Castro, A. Kolmakov, J.O. Löfken, C. Nowak, A.V. Soldatov, A. Wark, G. Yalovega, T. Möller, J. Chem. Phys., 115 (2001) 1319.
[168] M.H. Tuilier, D. Laporte, J.M. Esteva, Phys. Rev. A, 26 (1982) 372.
[169] S.G. Urquhart, R. Gillies, J. Chem. Phys., 124 (2006) 234704.
[170] E.W. Robertson, O.M. Wilkin, N.A. Young, Polyhedron, 19 (2000) 1493.
[171] I.R. Beattie, P.J. Jones, N.A. Young, J. Am. Chem. Soc., 114 (1992) 6146.
[172] N.A. Young, Jpn. J. Appl. Phys., 32 (1993) 776.
[173] T.E. Westre, P. Kennepohl, J.G. De Witt, B. Hedman, K.O. Hodgson, E.I. Solomon, J. Am. Chem. Soc., 119 (1997) 6297.
[174] M. Hargittai, J. Tremmel, I. Hargittai, J. Chem. Soc., Dalton Trans., (1980) 87.
[175] I.R. Beattie, M.D. Spicer, N.A. Young, J. Chem. Phys., 100 (1994) 8700.
[176] I.R. Beattie, P.J. Jones, N.A. Young, Mol. Phys., 72 (1991) 1309.
[177] I.R. Beattie, P.J. Jones, N.A. Young, Chem. Phys. Lett., 177 (1991) 579.
[178] M. Hargittai, N.Y. Subbotina, M. Kolonits, A.G. Gershikov, J. Chem. Phys., 94 (1991) 7278.
[179] B. Vest, Z. Varga, M. Hargittai, A. Hermann, P. Schwerdtfeger, Chem. Eur. J., 14 (2008) 5130.
[180] J.S. Ogden, R.S. Wyatt, J. Chem. Soc., Dalton Trans., (1987) 859.
[181] P.D. Gregory, J.S. Ogden, J. Chem. Soc., Dalton Trans., (1995) 1423.
[182] N.A. Young, J. Chem. Soc., Dalton Trans., (1996) 249.
[183] A.J. Bridgeman, O.M. Wilkin, N.A. Young, Inorg. Chem. Comm., 3 (2000) 681.
[184] C.A. Thompson, L. Andrews, R.D. Davy, J. Phys. Chem., 99 (1995) 7913.
[185] W.E. Klotzbücher, G.A. Ozin, J. Am. Chem. Soc., 95 (1973) 3790.
[186] G.A. Ozin, W.E. Klotzbücher, J. Am. Chem. Soc., 97 (1975) 3965.
[187] L.S. Kau, D.J. Spira-Solomon, J.E. Penner-Hahn, K.O. Hodgson, E.I. Solomon, J. Am. Chem. Soc., 109 (1987) 6433.
[188] E.I. Solomon, R.K. Szilagyi, S. DeBeer-George, L. Basumallick, Chem. Rev., 104 (2004) 419.
[189] J.L. Fulton, M.M. Hoffmann, J.G. Darab, Chem. Phys. Lett., 330 (2000) 300.
[190] J.L. Fulton, M.M. Hoffmann, J.G. Darab, B.J. Palmer, E.A. Stern, J. Phys. Chem. A, 104 (2000) 11651.
[191] P.W. Jolly, K. Jonas, C. Kruger, Y.H. Tsang, J. Organomet. Chem., 33 (1971) 109.
[192] K. Jonas, D.J. Brauer, C. Kruger, P.J. Roberts, Y.H. Tsang, J. Am. Chem. Soc., 98 (1976) 74.
[193] J.A. Venables, C.A. English, Acta Crystallogr. B, 30 (1974) 929.

[194] A.J. Bridgeman, G. Cavigliasso, N. Harris, N.A. Young, Chem. Phys. Lett., 351 (2002) 319.
[195] M. Kaupp, H.G. von Schnering, Angew. Chem. Int. Ed. Engl., 32 (1993) 861.
[196] M. Kaupp, M. Dolg, H. Stoll, H.G. von Schnering, Inorg. Chem., 33 (1994) 2122.
[197] W. Liu, R. Franke, M. Dolg, Chem. Phys. Lett., 302 (1999) 231.
[198] P. Pyykkö, M. Straka, M. Patzschke, Chem. Comm., (2002) 1728.
[199] S. Riedel, M. Straka, M. Kaupp, Phys. Chem. Chem. Phys., 6 (2004) 1122.
[200] S. Riedel, M. Straka, M. Kaupp, Chem. Eur. J., 11 (2005) 2743.
[201] S. Riedel, M. Kaupp, P. Pyykkö, Inorg. Chem., 47 (2008) 3379.
[202] R.L. Deming, A.L. Allred, A.R. Dahl, A.W. Herlinger, M.O. Kestner, J. Am. Chem. Soc., 98 (1976) 4132.
[203] X. Wang, L. Andrews, S. Riedel, M. Kaupp, Angew. Chem. Int. Ed., 46 (2007) 8371.
[204] J.F. Rooms, A.V. Wilson, I. Harvey, A.J. Bridgeman, N.A. Young, Phys. Chem. Chem. Phys., 10 (2008) 4594.
[205] W.J. Jackson, A. Moen, B.K. Nicholson, D.G. Nicholson, K.A. Porter, J. Chem. Soc., Dalton Trans., (2000) 491.
[206] F.E. Huggins, N. Yap, G.P. Huffman, C.L. Senior, Fuel Proc. Technol., 82 (2003) 167.
[207] M. Kaupp, H.G. von Schnering, Inorg. Chem., 33 (1994) 4179.
[208] M. Kaupp, H.G. von Schnering, Inorg. Chem., 33 (1994) 4718.
[209] M.W. Ruckman, M.F. Murray, J.K. Mowlem, J.F. Moore, D.R. Strongin, Chem. Phys. Lett., 198 (1992) 449.
[210] T.M. Zimkina, A.S. Vinogradov, Izv. Akad. Nauk SSSR Ser. Fiz., 36 (1972) 248.
[211] T.M. Zimkina, A.S. Vinogradov, Bull. Acad. Sci. USSR Phys. Ser., 36 (1972) 229.
[212] W. Levason, J.S. Ogden, A.K. Saad, N.A. Young, A.K. Brisdon, P.J. Holliman, J.H. Holloway, E.G. Hope, J. Fluorine Chem., 53 (1991) 43.
[213] A.K. Brisdon, J.H. Holloway, E.G. Hope, W. Levason, J.S. Ogden, A.K. Saad, J. Chem. Soc., Dalton Trans., (1992) 139.
[214] A.K. Brisdon, J.H. Holloway, E.G. Hope, W. Levason, J.S. Ogden, A.K. Saad, J. Chem. Soc., Dalton Trans., (1992) 447.
[215] S.A. Brewer, A.K. Brisdon, J.H. Holloway, E.G. Hope, W. Levason, J.S. Ogden, A.K. Saad, J. Fluorine Chem., 60 (1993) 13.
[216] W. Levason, J.S. Ogden, M.D. Spicer, N.A. Young, J. Am. Chem. Soc., 112 (1990) 1019.
[217] T.R. Gilson, W. Levason, J.S. Ogden, M.D. Spicer, N.A. Young, J. Am. Chem. Soc., 114 (1992) 5469.
[218] F.W. Kutzler, D.E. Ellis, T.I. Morrison, G.K. Shenoy, P.J. Viccaro, P.A. Montano, E.H. Appelman, L. Stein, M.J. Pellin, D.M. Gruen, Solid State Commun., 46 (1983) 803.
[219] S.H. Chou, F.W. Kutzler, D.E. Ellis, G.K. Shenoy, T.I. Morrison, P.A. Montano, Phys. Rev. B, 31 (1985) 1069.
[220] A. Hiraya, K. Fukui, P.K. Tseng, T. Murata, M. Watanabe, J. Phys. Soc. Jpn., 60 (1991) 1824.
[221] A.V. Soldatov, T.S. Ivanchenko, I.E. Shtekhin, A. Biankoni, Opt. Spectrosc., 73 (1992) 97.
[222] A.V. Soldatov, T.S. Ivanchenko, I.E. Shtekhin, A. Biankoni, Opt. Spektrosk., 73 (1992) 166.
[223] A.V. Soldatov, T.S. Ivanchenko, I.E. Shtekhin, A. Bianconi, Fiz. Tverd. Tela, 34 (1992) 1961.
[224] A.V. Soldatov, T.S. Ivanchenko, S. Dellalonga, A. Bianconi, Phys. Rev. B, 47 (1993) 16155.
[225] V.A. Yavna, A.N. Khoperskii, A.V. Soldatov, Opt. Spektrosk., 81 (1996) 787.

[226] H. Sambe, X. Qian, D.E. Ramaker, Phys. Rev. B, 53 (1996) 1779.
[227] F. Federmann, O. Björneholm, A. Beutler, T. Möller, Phys. Rev. Lett., 73 (1994) 1549.
[228] S. Kakar, O. Björneholm, J.O. Lofken, F. Federmann, A.V. Soldatov, T. Möller, Z. Phys. D, 40 (1997) 84.
[229] S. Coriani, O. Christiansen, T. Fransson, P. Norman, Phys. Rev. A, 85 (2012) 022507.
[230] W. Malzfeldt, W. Niemann, P. Rabe, R. Haensel, Springer Proc. Phys., 2 (1984) 445.
[231] P. Roubin, S. Varin, C. Crépin, B. Gauthier-Roy, A.M. Flank, P. Lagarde, F. Ténégal, Low Temp. Phys., 26 (2000) 691.
[232] E. Rühl, C. Heinzel, A.P. Hitchcock, H. Schmelz, C. Reynaud, H. Baumgärtel, W. Drube, R. Frahm, J. Chem. Phys., 98 (1993) 6820.
[233] E. Rühl, C. Heinzel, H. Baumgärtel, W. Drube, A.P. Hitchcock, Jpn. J. Appl. Phys., 32 (1993) 791.
[234] S. Kakar, O. Björneholm, J. Weigelt, A.R.B. de Castro, L. Tröger, R. Frahm, T. Möller, A. Knop, E. Rühl, Phys. Rev. Lett., 78 (1997) 1675.
[235] E. Rühl, H.W. Jochims, C. Schmale, E. Biller, A.P. Hitchcock, H. Baumgärtel, Chem. Phys. Lett., 178 (1991) 558.
[236] E. Rühl, C. Heinzel, A.P. Hitchcock, H. Baumgärtel, J. Chem. Phys., 98 (1993) 2653.
[237] E. Rühl, A.P. Hitchcock, P. Morin, M. Lavollee, J. Chim. Phys. Phys.-Chim. Biol., 92 (1995) 521.
[238] M. Breinig, M.H. Chen, G.E. Ice, F. Parente, B. Crasemann, G.S. Brown, Phys. Rev. A, 22 (1980) 520.
[239] S.J. Schaphorst, A.F. Kodre, J. Ruscheinski, B. Crasemann, T. Åberg, J. Tulkki, M.H. Chen, Y. Azuma, G.S. Brown, Phys. Rev. A, 47 (1993) 1953.
[240] A. Kodre, I. Arcon, J.P. Gomilsek, R. Preseren, R. Frahm, J. Phys. B At. Mol. Opt. Phys., 35 (2002) 3497.
[241] W. Malzfeldt, W. Niemann, P. Rabe, N. Schwentner, Springer Ser. Chem. Phys., 27 (1983) 203.
[242] C.A. Guryan, K.B. Lee, P.W. Stephens, A.I. Goldman, J.Z. Larese, P.A. Heiney, E. Fontes, Phys. Rev. B, 37 (1988) 3461.
[243] Q. Wang, C.X. Li, X.J. Niu, R. Shen, K.Q. Lu, S.Q. Wei, Z. Wu, T. Liu, Y. Xie, T. Hu, Phys. Rev. B, 72 (2005) 092202.
[244] A. Polian, J.M. Besson, M. Grimsditch, W.A. Grosshans, Phys. Rev. B, 39 (1989) 1332.
[245] A. Polian, J.P. Itié, E. Dartyge, A. Fontaine, G. Tourillon, Phys. Rev. B, 39 (1989) 3369.
[246] A. Di Cicco, A. Filipponi, J.P. Itié, A. Polian, Phys. Rev. B, 54 (1996) 9086.
[247] Y. Ito, H. Nakamatsu, T. Mukoyama, K. Omote, S. Yoshikado, M. Takahashi, S. Emura, Phys. Rev. A, 46 (1992) 6083.
[248] T. Yokoyama, T. Ohta, H. Sato, Phys. Rev. B, 55 (1997) 11320.
[249] H.C. Schmelz, M.A. Gaveau, C. Reynaud, C. Heinzel, H. Baumgärtel, E. Rühl, Physica B, 209 (1995) 519.
[250] M. Deutsch, G. Brill, P. Kizler, Phys. Rev. A, 43 (1991) 2591.
[251] M. Deutsch, P. Kizler, Phys. Rev. A, 45 (1992) 2112.
[252] Y. Ito, T. Tochio, K. Mutaguchi, H. OhHashi, N. Shigeoka, Y. Nakata, A.M. Vlaicu, T. Uruga, S. Emura, J.P. Gomilsek, Radiat. Phys. Chem., 61 (2001) 405.
[253] J.P. Gomilsek, A. Kodre, I. Arcon, M. Hribar, Phys. Rev. A, 68 (2003) 042505.
[254] T. Koizumi, T. Hayaishi, T. Matsuo, K. Shima, H. Tawara, T. Tonuma, A. Yagishita, J. Phys. Soc. Jpn., 58 (1989) 13.
[255] I. Arcon, A. Kodre, M. Stuhec, D. Glaviccindro, W. Drube, Phys. Rev. A, 51 (1995) 147.

[256] T. Tochio, Y. Ito, T. Mukoyama, M. Takahashi, S. Emura, J. Phys. IV, 7 (1997) 1263.
[257] Y. Ito, A.M. Vlaicu, T. Tochio, T. Mukoyama, M. Takahashi, S. Emura, Y. Azuma, Phys. Rev. A, 57 (1998) 873.
[258] A. Kodre, J.P. Gomilsek, I. Arcon, G. Aquilanti, Phys. Rev. A, 82 (2010) 022513.
[259] M. Lundwall, W. Pokapanich, H. Bergersen, A. Lindblad, T. Rander, G. Öhrwall, M. Tchaplyguine, S. Barth, U. Hergenhahn, S. Svensson, O. Björneholm, J. Chem. Phys., 126 (2007) 214706.
[260] R.G. Lacerda, L.R. Tessler, M.C. dos Santos, P. Hammer, F. Alvarez, F.C. Marques, J. Non-Cryst. Solids, 299 (2002) 805.
[261] Y. Muramatsu, T. Yamamoto, J.D. Denlinger, R.C.C. Perera, J. Electron Spectrosc. Relat. Phenom., 144 (2005) 799.
[262] M.F. Rosu, L. Niesen, A. vanVeen, J.H. Evans, J. Phys. Conds. Mat., 9 (1997) 149.
[263] G. Faraci, A.R. Pennisi, A. Terrasi, S. Mobilio, Phys. Rev. B, 38 (1988) 13468.
[264] G. Faraci, A.R. Pennisi, J.L. Hazemann, Phys. Rev. B, 56 (1997) 12553.
[265] P. Garcia, P. Martin, G. Carlot, E. Castelier, M. Ripert, C. Sabathier, C. Valot, F. D'Acapito, J.L. Hazemann, O. Proux, V. Nassif, J. Nucl. Mater., 352 (2006) 136.
[266] P. Martin, P. Garcia, G. Carlot, C. Sabathier, C. Valot, V. Nassif, O. Proux, J.L. Hazemann, Nucl. Instrumen. Meth. B, 266 (2008) 2887.
[267] M.H. Oliveira, F.C. Marques, Braz. J. Phys., 36 (2006) 282.
[268] P.A. Montano, J. Linton, V. Thieu, Y. Halpern, J. Synch. Rad., 8 (2001) 972.
[269] P. Roubin, S. Varin, C. Crépin, B. Gauthier-Roy, A.M. Flank, R. Delaunay, M. Pompa, B. Tremblay, J. Chem. Phys., 109 (1998) 7945.
[270] V.I. Lang, J.S. Winn, J. Chem. Phys., 94 (1991) 5270.
[271] J.S. Winn, J. Chem. Phys., 94 (1991) 5275.
[272] D. Hallamasek, E. Babka, E. Knözinger, J. Mol. Struct., 408/409 (1997) 125.
[273] H. Zhu, Y. Guo, Y. Xue, D.Q. Xie, J. Comput. Chem., 27 (2006) 1045.
[274] Schoen, L.J., D.E. Man, C. Knobler, D. White, J. Chem. Phys., 37 (1962) 1146.
[275] M.T. Bowers, W.H. Flygare, J. Chem. Phys., 44 (1966) 1389.
[276] L.F. Keyser, G.W. Robinson, J. Chem. Phys., 44 (1966) 3225.
[277] A.J. Barnes, H.E. Hallam, G.F. Scrimshaw, Farad. Soc. Trans., 65 (1969) 3159.
[278] L.F. Keyser, G.W. Robinson, J. Chem. Phys., 45 (1966) 1694.
[279] M.T. Bowers, J. Chem. Phys., 47 (1967) 3100.
[280] C. Girardet, D. Robert, J. Chem. Phys., 59 (1973) 5020.
[281] R.E. Wilde, T.K.K. Srinivasan, R.W. Harral, S.G. Sankar, J. Chem. Phys., 55 (1971) 5681.
[282] J.P. Connerade, M.A. Baig, C.A. Mayhew, J. Hormes, J. Electron Spectrosc. Relat. Phenom., 73 (1995) 173.
[283] G. Zimmerer, J. Lumin., 119 (2006) 1.
[284] N. Schwentner, E.E. Koch, J. Jortner, Electronic Excitations in Condensed Rare-Gases, Springer Tracts in Modern Physics, Vol. 107, 1985.
[285] V.A. Apkarian, N. Schwentner, Chem. Rev., 99 (1999) 1481.
[286] T. Möller, A.R.B. DeCastro, K. von Haeften, A. Kolmakov, T. Laarmann, O. Löfken, C. Nowak, F. Picucci, M. Riedler, C. Rienecker, A. Wark, M. Wolff, J. Electron Spectrosc. Relat. Phenom., 103 (1999) 185.
[287] J. Hormes, G. Happel, J. Chem. Phys., 78 (1983) 1758.
[288] J. Hormes, R. Grinter, B. Breithaupt, D.M. Kolb, J. Chem. Phys., 78 (1983) 158.
[289] H.D. Lagier, K.H. Godderz, J. Hormes, A. Klein, J. Mol. Struct., 222 (1990) 253.
[290] P. Gurtler, J. Lecalve, D. Raasch, Chem. Phys. Lett., 177 (1991) 585.
[291] M. Chergui, C. Crépin, T. Hebert, A. Tramer, Chem. Phys. Lett., 197 (1992) 467.
[292] B. Healy, J.G. McCaffrey, J. Chem. Phys., 110 (1999) 3903.

[293] B. Healy, P. Kerins, J.G. McCaffrey, Low Temp. Phys., 38 (2012) 679.
[294] P. Kerins, B. Healy, J.G. McCaffrey, Low Temp. Phys., 26 (2000) 756.
[295] T. Hebert, U. Schriever, D.M. Kolb, Chem. Phys. Lett., 200 (1992) 258.
[296] S. Moeller, P. Gurtler, J. Lumin., 72-4 (1997) 881.
[297] S. Moeller, P. Gurtler, J. Chem. Phys., 106 (1997) 3920.
[298] A. Schrimpf, C. Boekstiegel, H.J. Stockmann, T. Bornemann, K. Ibbeken, J. Kraft, B. Herkert, J. Phys. Conds. Mat., 8 (1996) 3677.
[299] R. Schriever, M. Chergui, N. Schwentner, J. Phys. Chem., 95 (1991) 6124.
[300] J.G. McCaffrey, H. Kunz, N. Schwentner, J. Chem. Phys., 96 (1992) 2825.
[301] J.G. McCaffrey, H. Kunz, N. Schwentner, J. Chem. Phys., 96 (1992) 155.
[302] F. Salama, J. Fournier, Chem. Phys. Lett., 120 (1985) 35.
[303] V.A. Bracken, P. Gurtler, J.G. McCaffrey, J. Phys. Chem. A, 101 (1997) 9854.
[304] J. Eberlein, M. Creuzburg, Mol. Phys., 96 (1999) 451.
[305] B.M. Cheng, C.P. Liu, W.J. Lo, Y.P. Lee, Nucl. Inst. Meth. A, 467 (2001) 1461.
[306] K. Godderz, N. Schwentner, Fiz. Nizk. Temp., 22 (1996) 205.
[307] M. Dickgiesser, N. Schwentner, Nucl. Instrumen. Meth. B, 168 (2000) 252.
[308] V. Berghof, M.S. Gudipati, N. Schwentner, J. Chem. Phys., 120 (2004) 1414.
[309] B.M. Cheng, W.J. Lo, W.C. Hung, Chem. Phys. Lett., 236 (1995) 355.
[310] B.M. Cheng, J. Phys. Chem., 100 (1996) 8200.
[311] M. Gerones, A.J. Downs, M.F. Erben, M. Ge, R.M. Romano, L. Yao, C.O. Della Védova, J. Phys. Chem. A, 112 (2008) 5947.
[312] P. Gurtler, E.E. Koch, J. Mol. Struct., 60 (1980) 287.
[313] M. Chergui, N. Schwentner, A. Tramer, Chem. Phys. Lett., 201 (1993) 187.
[314] M. Kraas, P. Gurtler, Chem. Phys. Lett., 183 (1991) 264.
[315] C. Bressler, W.G. Lawrence, N. Schwentner, J. Chem. Phys., 105 (1996) 10178.
[316] C. Bressler, W.G. Lawrence, N. Schwentner, J. Chem. Phys., 105 (1996) 1318.
[317] J. Lecalve, P. Gurtler, J. Chim. Phys. Phys.-Chim. Biol., 86 (1989) 1847.
[318] V. Saile, D. Reiger, W. Steinmann, T. Wegehaupt, Phys. Lett. A, 79 (1980) 221.
[319] J.J. Jia, W.L. Obrien, T.A. Callcott, Q.Y. Dong, J.E. Rubensson, D.R. Mueller, D.L. Ederer, Phys. Rev. Lett., 67 (1991) 731.
[320] A.N. Ogurtsov, E.V. Savchenko, J. Becker, M. Runne, G. Zimmerer, Low Temp. Phys., 23 (1997) 851.
[321] M. Runne, J. Becker, W. Laasch, D. Varding, G. Zimmerer, M. Liu, R.E. Johnson, Nucl. Instrumen. Meth. B, 82 (1993) 301.
[322] A.N. Ogurtsov, E.V. Savchenko, J. Becker, M. Runne, G. Zimmerer, J. Lumin., 76-7 (1998) 478.
[323] A.N. Ogurtsov, E.V. Savchenko, E. Gminder, S. Vielhauer, G. Zimmerer, Surf. Rev. Lett., 9 (2002) 45.
[324] A.N. Ogurtsov, E.V. Savchenko, E. Sombrowski, S. Vielhauer, G. Zimmerer, Low Temp. Phys., 29 (2003) 858.
[325] M. Schwoererbohning, T. Kloiber, W. Laasch, T. Tochtrop, D. Varding, G. Zimmerer, J. Lumin., 48-9 (1991) 626.
[326] O.N. Grigorashchenko, A.N. Ogurtsov, E.V. Savchenko, J. Becker, M. Runne, G. Zimmerer, Surf. Sci., 390 (1997) 277.
[327] A. Ogurtsov, E. Savchenko, S. Vielhauer, G. Zimmerer, J. Lumin., 112 (2005) 97.
[328] E. Savchenko, A. Ogurtsov, I. Khyzhniy, G. Stryganyuk, G. Zimmerer, Phys. Chem. Chem. Phys., 7 (2005) 785.
[329] E.V. Savchenko, A.N. Ogurtsov, G. Zimmerer, Low Temp. Phys., 29 (2003) 270.
[330] A.N. Ogurtsov, E.V. Savchenko, J. Becker, M. Runne, G. Zimmerer, Chem. Phys. Lett., 281 (1997) 281.

[331] J. Becker, O.N. Grigorashchenko, A.N. Ogurtsov, M. Runne, E.V. Savchenko, G. Zimmerer, J. Phys. D Appl. Phys., 31 (1998) 749.
[332] H.C. Lu, H.K. Chen, B.M. Cheng, Y.P. Kuo, J.F. Ogilvie, J. Phys. B At. Mol. Opt. Phys., 38 (2005) 3693.
[333] Y.P. Kuo, H.C. Lu, Y.J. Wu, B.M. Cheng, J.F. Ogilvie, Chem. Phys. Lett., 447 (2007) 168.
[334] H.C. Lu, H.K. Chen, B.M. Cheng, J.F. Ogilvie, Spectrochim. Acta A, 71 (2008) 1485.
[335] M.E. Boyle, B.E. Williamson, P.N. Schatz, J.P. Marks, P.A. Snyder, Chem. Phys. Lett., 130 (1986) 33.
[336] B.E. Williamson, M.E. Boyle, P.N. Schatz, J.P. Marks, P.A. Snyder, Chem. Phys. Lett., 140 (1987) 483.
[337] T.C. Vancott, J.L. Rose, G.C. Misener, B.E. Williamson, A.E. Schrimpf, M.E. Boyle, P.N. Schatz, J. Phys. Chem., 93 (1989) 2999.
[338] B.E. Williamson, T.C. Vancott, J.L. Rose, A. Schrimpf, M. Koralewski, P.N. Schatz, J. Phys. Chem., 95 (1991) 6835.
[339] T.C. Vancott, M. Koralewski, D.H. Metcalf, P.N. Schatz, B.E. Williamson, J. Phys. Chem., 97 (1993) 7417.
[340] M.E. Boyle, B.E. Williamson, P.N. Schatz, J.P. Marks, P.A. Snyder, Chem. Phys. Lett., 125 (1986) 349.
[341] Y.J. Wu, H.F. Chen, C. Camacho, H.A. Witek, S.C. Hsu, M.Y. Lin, S.L. Chou, J.F. Ogilvie, B.M. Cheng, Astrophys. J., 701 (2009) 8.
[342] Y.J. Wu, M.Y. Lin, S.C. Hsu, B.M. Cheng, ChemPhysChem, 10 (2009) 901.
[343] Y.J. Chen, M. Nuevo, J.M. Hsieh, T.S. Yih, W.H. Sun, W.H. Ip, H.S. Fung, S.Y. Chiang, Y.Y. Lee, J.M. Chen, C.Y.R. Wu, A&A, 464 (2007) 253.
[344] M. Nuevo, Y.J. Chen, T.S. Yih, W.H. Ip, H.S. Fung, C.Y. Cheng, H.R. Tsai, C.Y.R. Wu, Adv. Space Res., 40 (2007) 1628.
[345] Y.J. Wu, M.Y. Lin, S.L. Chou, H.F. Chen, H.C. Lu, H.K. Chen, B.M. Cheng, Astrophys. J., 721 (2010) 856.
[346] Y.J. Wu, H.F. Chen, S.L. Chou, M.Y. Lin, B.M. Cheng, Chem. Phys. Lett., 497 (2010) 12.
[347] M.S. Gudipati, J. Daverkausen, G. Hohlneicher, Chem. Phys., 173 (1993) 143.
[348] M.S. Gudipati, M. Kalb, Chem. Phys. Lett., 268 (1997) 169.
[349] G. Monninger, M. Förderer, P. Gürtler, S. Kalhofer, S. Petersen, L. Nemes, P.G. Szalay, W. Krätschmer, J. Phys. Chem. A, 106 (2002) 5779.
[350] M.A. Chesters, E.C. Hargreaves, M. Pearson, P. Hollins, D.A. Slater, J.M. Chalmers, B. Ruzicka, M. Surman, M.J. Tobin, Nuovo Cimento Soc. Ital. Fis. D, 20 (1998) 439.
[351] K.R. Thompson, K.D. Carlson, J. Chem. Phys., 49 (1968) 4379.
[352] E. Knözinger, R. Wittenbeck, J. Am. Chem. Soc., 105 (1983) 2154.
[353] E. Knözinger, R. Wittenbeck, Infrared Phys., 24 (1984) 135.
[354] U. Bergmann, P. Glatzel, S.P. Cramer, Microchem. J., 71 (2002) 221.
[355] M. Krisch, F. Sette, Surf. Rev. Lett., 9 (2002) 969.
[356] U. Bergmann, H. Groenzin, O.C. Mullins, P. Glatzel, J. Fetzer, S.P. Cramer, Pet. Sci. Technol., 22 (2004) 863.
[357] D. Sokaras, D. Nordlund, T.C. Weng, R.A. Mori, P. Velikov, D. Wenger, A. Garachtchenko, M. George, V. Borzenets, B. Johnson, Q. Qian, T. Rabedeau, U. Bergmann, Rev. Sci. Instrum., 83 (2012) 043112.
[358] N. Hiraoka, H. Fukui, H. Tanida, H. Toyokawa, Y.Q. Cai, K.D. Tsuei, J. Synchrotron Rad., 20 (2013) 266.
[359] D.T. Bowron, M.H. Krisch, A.C. Barnes, J.L. Finney, A. Kaprolat, M. Lorenzen, Phys. Rev. B, 62 (2000) R9223.

[360] A. Sakko, S. Galambosi, J. Inkinen, T. Pylkkänen, M. Hakala, S. Huotari, K. Hämäläinen, Phys. Chem. Chem. Phys., 13 (2011) 11678.
[361] L.Å. Näslund, J. Lüning, Y. Ufuktepe, H. Ogasawara, P. Wernet, U. Bergmann, L.G.M. Pettersson, A. Nilsson, J. Phys. Chem. B, 109 (2005) 13835.
[362] L.Å. Näslund, D.C. Edwards, P. Wernet, U. Bergmann, H. Ogasawara, L.G.M. Pettersson, S. Myneni, A. Nilsson, J. Phys. Chem. A, 109 (2005) 5995.
[363] U. Bergmann, A. Di Cicco, P. Wernet, E. Principi, P. Glatzel, A. Nilsson, J. Chem. Phys., 127 (2007) 174504.
[364] H. Fukui, S. Huotari, D. Andrault, T. Kawamoto, J. Chem. Phys., 127 (2007) 134502.
[365] U. Bergmann, D. Nordlund, P. Wernet, M. Odelius, L.G.M. Pettersson, A. Nilsson, Phys. Rev. B, 76 (2007) 024202.
[366] A. Nilsson, D. Nordlund, I. Waluyo, N. Huang, H. Ogasawara, S. Kaya, U. Bergmann, L.Å. Näslund, H. Östrom, P. Wernet, K.J. Andersson, T. Schiros, L.G.M. Pettersson, J. Electron Spectrosc. Relat. Phenom., 177 (2010) 99.
[367] U. Bergmann, P. Wernet, P. Glatzel, M. Cavalleri, L.G.M. Pettersson, A. Nilsson, S.P. Cramer, Phys. Rev. B, 66 (2002) 092107.
[368] P. Wernet, D. Nordlund, U. Bergmann, M. Cavalleri, M. Odelius, H. Ogasawara, L.Å. Näslund, T.K. Hirsch, L. Ojamäe, P. Glatzel, L.G.M. Pettersson, A. Nilsson, Science, 304 (2004) 995.
[369] J.S. Tse, D.M. Shaw, D.D. Klug, S. Patchkovskii, G. Vankó, G. Monaco, M. Krisch, Phys. Rev. Lett., 100 (2008) 095502.
[370] C.J. Sahle, C. Sternemann, C. Schmidt, S. Lehtola, S. Jahn, L. Simonelli, S. Huotari, M. Hakala, T. Pylkkanen, A. Nyrow, K. Mende, M. Tolan, K. Hamalainen, M. Wilke, Proc. Natl. Acad. Sci. U. S. A., 110 (2013) 6301.
[371] U. Bergmann, O.C. Mullins, S.P. Cramer, Anal. Chem., 72 (2000) 2609.
[372] U. Bergmann, H. Groenzin, O.C. Mullins, P. Glatzel, J. Fetzer, S.P. Cramer, Chem. Phys. Lett., 369 (2003) 184.
[373] J.P. Rueff, Y. Joly, F. Bartolomé, M. Krisch, J.L. Hodeau, L. Marques, M. Mezouar, A. Kaprolat, M. Lorenzen, F. Sette, J. Phys. Conds. Mat., 14 (2002) 11635.
[374] N. Huang, D. Nordlund, C. Huang, U. Bergmann, T.M. Weiss, L.G.M. Pettersson, A. Nilsson, J. Chem. Phys., 135 (2011) 164509.
[375] F. Hennies, S. Polyutov, I. Minkov, A. Pietzsch, M. Nagasono, H. Ågren, L. Triguero, M.N. Piancastelli, W. Wurth, F. Gel'mukhanov, A. Föhlisch, Phys. Rev. A, 76 (2007) 032505.
[376] A. Mattila, J.A. Soininen, S. Galambosi, S. Huotari, G. Vankó, N.D. Zhigadlo, J. Karpinski, K. Hämäläinen, Phys. Rev. Lett., 94 (2005) 247003.
[377] P.S. Miedema, P. Ngene, A.M.J. van der Eerden, T.C. Weng, D. Nordlund, D. Sokaras, R. Alonso-Mori, A. Juhin, P.E. de Jongh, F.M.F. de Groot, Phys. Chem. Chem. Phys., 14 (2012) 5581.
[378] C. Sternemann, M. Volmer, J.A. Soininen, H. Nagasawa, M. Paulus, H. Enkisch, G. Schmidt, M. Tolan, W. Schülke, Phys. Rev. B, 68 (2003) 035111.
[379] S. Galambosi, M. Knaapila, J.A. Soininen, K. Nygård, S. Huotari, F. Galbrecht, U. Scherf, A.P. Monkman, K. Hämäläinen, Macromolecules, 39 (2006) 9261.
[380] H. Fukui, M. Kanzaki, N. Hiraoka, Y.Q. Cai, Phys. Chem. Min., 36 (2009) 171.
[381] S.K. Lee, P.J. Eng, H.K. Mao, Y. Meng, M. Newville, M.Y. Hu, J.F. Shu, Nat. Mater., 4 (2005) 851.
[382] S.K. Lee, P.J. Eng, H.K. Mao, Y. Meng, J. Shu, Phys. Rev. Lett., 98 (2007) 105502.
[383] C. Sternemann, J.A. Soininen, S. Huotari, G. Vankó, M. Volmer, R.A. Secco, J.S. Tse, M. Tolan, Phys. Rev. B, 72 (2005) 035104.

[384] T.T. Fister, G.T. Seidler, C. Hamner, J.O. Cross, J.A. Soininen, J.J. Rehr, Phys. Rev. B, 74 (2006) 214117.
[385] S. Huotari, T. Pylkkänen, J.A. Soininen, J.J. Kas, K. Hämäläinen, G. Monaco, J. Synchrotron Rad., 19 (2012) 106.
[386] J. Jiménez-Mier, U. Diebold, D.L. Ederer, T.A. Callcott, M. Grush, R.C. Perera, Phys. Rev. B, 65 (2002) 184105.
[387] J. Jiménez-Mier, D.L. Ederer, T. Schuler, Phys. Rev. B, 70 (2004) 035216.
[388] J. Jiménez-Mier, D.L. Ederer, T. Schuler, Phys. Rev. A, 72 (2005) 052502.
[389] J. Jiménez-Mier, D.L. Ederer, T. Schuler, Radiat. Phys. Chem., 75 (2006) 1666.
[390] J. Jiménez-Mier, G.M. Herrera-Perez, P. Olalde-Velasco, E. Chavira, I. Jimenez, D.L. Ederer, T. Schuler, Radiat. Eff. Defects Solids, 162 (2007) 613.
[391] J. Jiménez-Mier, G. Herrera-Perez, P. Olalde-Velasco, E. Chavira, I. Jiménez-DelVal, D.L. Ederer, Revista Mexicana De Fisica, 53 (2007) 38.
[392] J. Jiménez-Mier, G.M. Herrera-Perez, P. Olalde-Velasco, D.L. Ederer, T. Schuler, Revista Mexicana De Fisica, 54 (2008) 30.
[393] K.M. Lancaster, K.D. Finkelstein, S. DeBeer, Inorg. Chem., 50 (2011) 6767.
[394] U. Bergmann, P. Glatzel, J.H. Robblee, J. Messinger, C. Fernandez, R. Cinco, H. Visser, K. McFarlane, E. Bellacchio, S. Pizarro, K. Sauer, V.K. Yachandra, M.P. Klein, B.L. Cox, K.H. Nealson, S.P. Cramer, J. Synchrotron Rad., 8 (2001) 199.
[395] A. Kotani, European Physical Journal B, 47 (2005) 3.
[396] J.J. Rehr, Radiat. Phys. Chem., 75 (2006) 1547.
[397] H. Hayashi, Anal. Sci., 24 (2008) 15.
[398] P. Glatzel, M. Sikora, M. Fernández-García, Eur. Phys. J.-Spec. Top., 169 (2009) 207.
[399] P. Glatzel, M. Sikora, G. Smolentsev, M. Fernández-García, Catal. Today, 145 (2009) 294.
[400] F.J. Himpsel, Phys. Status Solidi B-Basic Solid State Phys., 248 (2011) 292.
[401] J. Nordgren, J.E. Rubensson, J. Electron Spectrosc. Relat. Phenom., 188 (2013) 3.
[402] V. Potapkin, A.I. Chumakov, G.V. Smirnov, J.P. Celse, R. Ruffer, C. McCammon, L. Dubrovinsky, J. Synchrotron Rad., 19 (2012) 559.